

Charles University in Prague
Faculty of Mathematics and Physics

DOCTORAL THESIS



Jan Čechura

Physics of X-ray binaries

Academy of Sciences of the Czech Republic
Astronomical Institute

Supervisor of the doctoral thesis: doc. RNDr. Petr Hadrava, DrSc.

Study programme: Physics

Specialization: Theoretical physics, astronomy
and astrophysics

2014

I declare that I carried out this doctoral thesis independently, and only with the cited sources, literature and other professional sources.

I understand that my work relates to the rights and obligations under the Act No. 121/2000 Coll., the Copyright Act, as amended, in particular the fact that the Charles University in Prague has the right to conclude a license agreement on the the use of this work as a school work pursuant to Section 60 paragraph 1 of the Copyright Act.

In Prague, September 1, 2014

.....

Jan Čechura

Název práce: Fyzika rentgenových dvojhvězd

Autor: Jan Čechura

Pracoviště: Astronomický ústav Akademie věd České republiky

Vedoucí disertační práce: doc. RNDr. Petr Hadrava, DrSc.

Abstrakt: Představujeme novou metodu interpretace pozorování rentgenových hvězd, která je založena na porovnání spektroskopických dat a numerických předpovědí zářivě hydrodynamického modelu hvězdného větru v rentgenových dvojhvězdách. Použitím nepřímé zobrazovací metody – dopplerovské tomografie – počítáme syntetické tomogramy předpovězené emise v rentgenových stavech Low/Hard a High/Soft a porovnááme je s tomogramy pořízenými s použitím fázově rozlišených optických spekter Cygnu X-1, typického představitele rentgenových dvojhvězd. Emise v rentgenových dvojhvězdách je určena lokálními fyzikálními podmínkami v okolohvězdném prostředí – jmenovitě hustotou, teplotou a ionizačním parametrem. Tyto veličiny jsou počítány zářivě hydrodynamickým numerickým modelem a silně závisí na rentgenovém stavu těchto systémů. Zvýšením intezity rentgenové emise, kterou v modelu produkuje kompaktní průvodce, dosahujeme celkové redistribuce okolohvězdné látky v blízkosti modelovaného systému. Tyto změny, jež simulují přechod mezi dvěma hlavními spektrálními stavy Cygnu X-1, jsou patrné i v syntetických tomogramech a odpovídají výsledkům pozorování.

Klíčová slova: rentgenové dvojhvězdy, zářivá hydrodynamika, fokusovaný hvězdný vítr

Title: Physics of X-ray binaries

Author: Jan Čechura

Department: Astronomical Institute of the Academy of Sciences of the Czech Republic

Supervisor: doc. RNDr. Petr Hadrava, DrSc.

Abstract: We present a novel observation interpreting method for the high-mass X-ray binaries (HMXBs) based on a combination of spectroscopic data and numerical results of a radiation hydrodynamic model of stellar wind in HMXBs. By using an indirect imaging method of Doppler tomography, we calculate synthetic tomograms of a predicted emission in Low/Hard and High/Soft X-ray states and compare them with tomograms produced using phase-resolved optical spectra of Cygnus X-1, a prototype of HMXBs. The emissions of HMXBs are determined by the local conditions within the circumstellar medium - namely by local density, temperature, and ionization parameter. These quantities are computed by the radiation hydrodynamic code and strongly depend on the X-ray state of such systems. By increasing intensity of an X-ray emission produced by the compact companion in the HMXB-model, we achieved a complete redistribution of the circumstellar medium in the vicinity of the modelled system. These changes (which simulate the transitions between two major spectral states) are also apparent in the synthetic Doppler tomograms which are in a good agreement with the observational data.

Keywords: X-ray binaries, radiation hydrodynamics, focused stellar wind

Acknowledgements

Herein, I would like to express my deepest gratitude to my family for the support they have given me. Special thanks belong to my parents who raised me and encouraged, and to whom I owe so much.

I would also like to thank my supervisor Petr Hadrava, my advisors Saku Vrtilek and Michael McCollough, and colleagues Richard Wünsch and Jiří Svoboda for their comments, suggestions and collaboration.

I acknowledge the Astronomical Institute of the Academy of Sciences of the Czech Republic for providing me with a stimulating working environment and appropriate computational equipment. Furthermore, I would like to express my gratitude to the Harvard–Smithsonian Center for Astrophysics for the use of their facilities. This work was supported in part by the Czech Science Foundation (GAČR 14-37086G) – Albert Einstein Center for Gravitation and Astrophysics, by grant SVV-260089, and by the Fund of Mobility of the Charles University in Prague.

To my parents and grandparents

Preface

High-Mass X-ray Binary systems (HMXBs) are interacting binaries in which a compact companion, either a neutron star or a black hole, orbits around a massive early-type star, usually an OB supergiant. This type of stars is characterized by an enhanced mass-loss rate of the order of $\sim 10^{-6} M_{\odot} \text{ yr}^{-1}$. The compact companion is immersed in the stellar wind and accretes material from it, giving rise to a strong X-ray flux. The interaction between the companion and the stellar wind was a subject of many numerical studies – cf., e.g. Blondin et al. (1990), Hadrava & Čechura (2012), or Manousakis et al. (2012), revealing that the wind of the massive star is severely disrupted by the gravity and photo-ionization of the companion. In the case of early type stars, the stellar wind is predominantly driven by the line absorption of radiation from the primary by the wind material and this mechanism can impart sufficient momentum to drive the material to velocities of $\sim 2000 \text{ km s}^{-1}$.

In Chapter III, we present an enhanced version of our radiation hydrodynamic code introduced in (Hadrava & Čechura 2012) which was specifically designed to simulate the circumstellar environment of X-ray binaries. In Sec. 3.1, we describe numerical methods employed by the code as well as various numerical settings and boundary conditions. Later in Sec. 3.2, we use test problems to evaluate the code’s performance in order to assess its applicability to astrophysical problems.

In Chapter IV, we use the radiation hydrodynamic code to investigate the properties and dynamics of the stellar wind in Cygnus X-1. First in Sec. 4.1, we give a detailed description of the physical model we use in our simulations and a summary of all physical effects and phenomena involved in the model. Then in Sec. 4.2, we present numerical settings of the simulations including the description of boundary conditions. The revised results of anisotropic stellar wind in HMXBs can be found in Sec. 4.3 all together with the description of the grid of simulations computed for specific values of selected physical parameters. First in two-dimensional simulations, we investigate the role of various physical parameters that influence the interplay between the stellar wind and the compact companion, namely, the mass ratio of the binary components, and parameters of the line-driven wind model. Then, we show the results of three-dimensional simulations, revealing the importance of X-ray photo-ionization. All calculations show the formation of a gaseous tail with complicated dynamics behind the compact companion. This tail is a product of a process which resembles Bondi-Hoyle-Lyttleton accretion (Bondi & Hoyle 1944).

In Chapter V, we combine computational and observational approach to address the topic of distribution of matter in the immediate vicinity of the X-ray binaries and its structure. In Sec. 5.6, we give a detailed description of the obtained optical

spectra used for our analysis. We combine them with simultaneous X-ray data to provide additional information about the X-ray state of the system in order to conduct Doppler analysis of the optical spectra in both major X-ray states of Cygnus X-1 separately. In Sec. 5.7, we calculate synthetic Doppler tomograms of a predicted emission in Low/Hard and High/Soft X-ray states from our radiation hydrodynamic model and compare them with Doppler tomograms produced using optical spectra of Cygnus X-1.

The majority of the results presented in this Thesis were published in two papers in *Astronomy & Astrophysics* journal (Hadrava & Čechura 2012; Čechura & Hadrava 2014), and several proceedings (Čechura 2012; Hadrava & Čechura 2013; Vrtilík et al. 2013).

Contents

Preface	xi
I Introduction	1
1.1 Basic properties of X-ray binaries	2
1.1.1 Low mass X-ray binaries	4
1.1.2 High mass X-ray binaries	4
1.1.3 X-ray spectral states	5
1.2 Cygnus X-1/HDE 226868	6
1.2.1 Discovery and history of observation	6
1.2.2 Orbital parameters	7
1.2.3 Mass loss	8
II Related topics in stellar astrophysics	11
2.1 Restricted three-body problem	11
2.1.1 Roche lobes	14
2.2 Stellar wind	16
2.2.1 Hydrostatic equilibrium	17
2.2.2 Parker's model	18
2.2.3 Line-driven wind model	20
2.3 Accreting compact objects	22
2.3.1 Spherical flow onto a stationary accretor	23
2.3.2 Bondi-Hoyle-Lyttleton accretion	26
III Radiation hydrodynamic model	31
3.1 Numerical hydrodynamics	31
3.1.1 The piecewise parabolic method	32
3.1.2 Riemann solver	35
3.1.3 Boundary conditions	35
3.1.4 Time-stepping	36
3.1.5 Sink particles	36
3.1.6 Accretion onto sink particles	39
3.1.7 Motion of sink particles	39
3.2 Code test problems	40
3.2.1 Mach 3 wind tunnel with a step	41
3.2.2 Double Mach reflection of a strong shock	44

IV Model of HDE 226868/Cygnus X-1	49
4.1 The physical model of the stellar wind	49
4.1.1 The m-CAK model & finite-disk correction factor	49
4.1.2 Photo-ionization	50
4.1.3 Parameterizing the force multiplier	50
4.1.4 Limb-darkening & gravity-darkening	51
4.1.5 Radiative cooling & X-ray heating	52
4.2 Numerical settings	53
4.2.1 Boundary conditions	53
4.3 Results of the stellar wind simulations	54
4.3.1 Dependency on α parameter	56
4.3.2 Effects of the mass of the companion	59
4.3.3 Effects of the X-ray ionization	62
4.3.4 The three-dimensional model	64
4.3.5 3D visualization	69
V Doppler tomography	71
5.1 Introduction	71
5.2 The principles of Doppler tomography	73
5.2.1 Profile formation	74
5.2.2 Filtered back-projection	75
5.2.3 Maximum entropy inversion	76
5.3 Axioms of Doppler tomography	77
5.4 Modulated Doppler tomography	78
5.5 The application of Doppler tomography	79
5.5.1 Interpreting Doppler maps in X-ray binaries	79
5.6 Doppler imaging results for Cygnus X-1	81
5.6.1 Determination of X-ray state of Cygnus X-1	85
5.6.2 The Low/Hard state	89
5.6.3 The High/Soft state	91
5.7 Production of synthetic Doppler tomograms	93
VI Conclusion	97
VII Future perspective	101
Bibliography	103
List of author's publications	111

Chapter I

Introduction

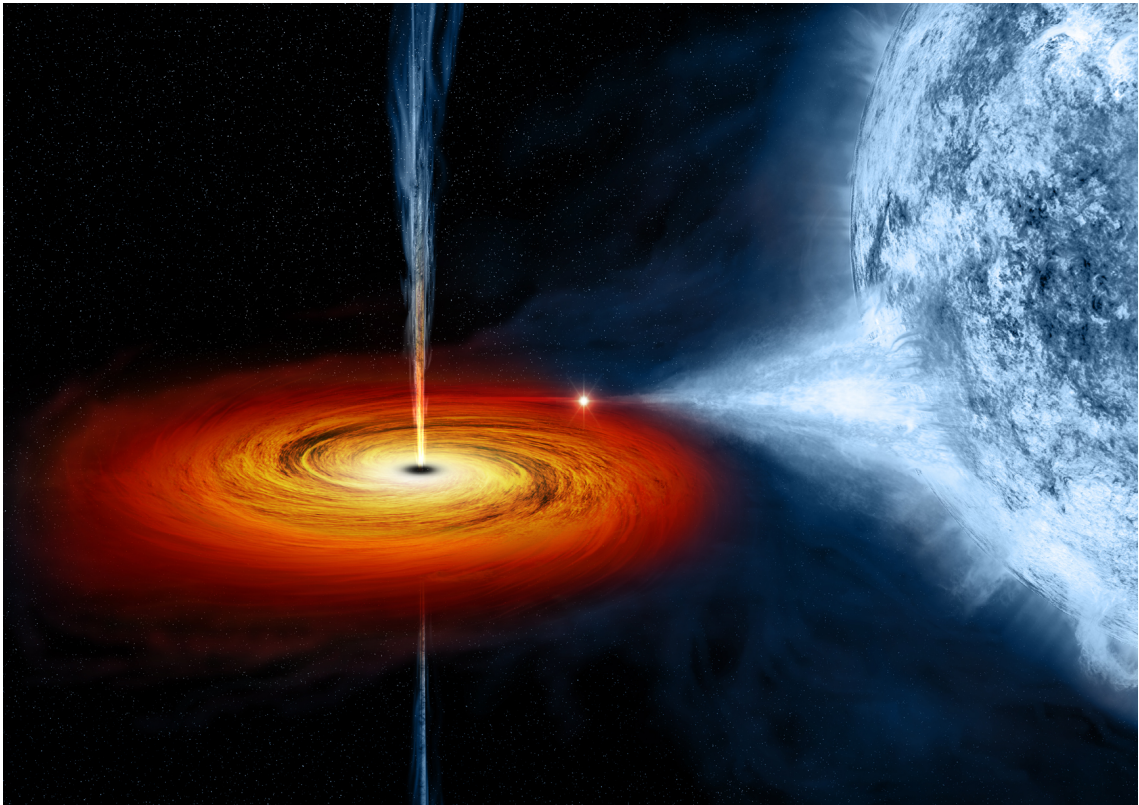


Figure 1.1: Visualisation of a high mass X-ray binary system with a black hole companion like Cygnus X-1: a stellar-mass black hole being fed by a donor star. Credit: M. Weiss (NASA/CXC).

An X-ray binary contains either a neutron star or a black hole accreting material from a companion star. X-ray binaries constitute the brightest class of X-ray sources in the sky, and they were the main focus of the first 15 years of X-ray astronomy, until the advent of X-ray imaging instruments in the late 1970s allowed fainter classes of sources to be studied. The first X-ray point-like source outside the solar system was Scorpius X-1 (Giacconi et al. 1962), subsequently classified as an X-ray binary (Gursky 1966; Sandage et al. 1966; Gottlieb et al. 1975). Since then

approximately 200 X-ray binaries have been identified from various X-ray surveys. Although first detected in X-ray, an identification of optical counterparts to an X-ray binary is crucial to establish the nature of the mass donating companion star, the overall geometry of the accretion flow, and the mass of the X-ray source.

1.1 Basic properties of X-ray binaries

The primary factors that determine the emission properties of an accreting compact object are (i) whether the central object is a black hole or a neutron star, (ii) if it is a neutron star, the strength and geometry of its magnetic field, and (iii) the geometry of the accretion flow from the mass donor (either accretion disk or more spherical accretion of the stellar wind). These determine whether the emission region is the small magnetic polar cap of a neutron star, a hot accretion disk surrounding a black hole, a shock heated region in an approximately isotropic stellar wind, or a boundary layer between an accretion disk and a neutron star. Two more factors are the mass of the central object, and the mass accretion rate; these influence the overall luminosity, spectral shape and time variability of the emission.

A neutron star with a strong magnetic field ($\sim 10^{12}$ G) will disrupt the accretion flow at several hundreds neutron star radii and funnel material onto the magnetic poles (Pringle & Rees 1972; Davidson & Ostriker 1973; Lamb et al. 1973). If the magnetic and rotation axes are misaligned, X-ray pulsation will be observed if the beamed emission from the magnetic poles rotates through the line of sight – cf., e.g., Meszaros et al. (1980); Nagel (1981a,b); Wang & Welter (1981). When the magnetic field of the neutron star is relatively weak ($< 10^{10}$ G), the disk may touch or come close to the neutron star surface. The energy release from the inner accretion disk and the boundary layer between the disk and the neutron star will dominate the emission (Mitsuda et al. 1984). If the central object is a black hole, the X-ray emission comes from the inner disk and are the results of viscous heating (Shakura & Sunyaev 1973).

Instabilities in the emission region, or its influence on the nearby accretion flow, can give rise to rapid fluctuations, or quasi-periodic oscillations (QPOs). The material, as it accumulates on the neutron star, may reach a critical mass and undergo a thermonuclear flash, resulting in an X-ray burst. Instabilities in the accretion flow can also give rise to X-ray bursts, or flashes (Taam & Fryxell 1988).

Many X-ray binaries are transient sources that appear on a time scale of a few days, and then decay over many tens or hundreds of days (White et al. 1984; van Paradijs & Verbunt 1984). These transient sources can, for a few weeks, be amongst the brightest in the sky, before they fade away. They are particularly important in the study of X-ray binaries since they cover an enormous dynamic range in luminosity (typically 10^4 – 10^5). This allows models for the emission region and the accretion process to be tested over a large range of mass accretion rate. The transient episodes may result from an instability in the accretion disk, or a mass ejection episode from the companion. Many transients are seen to recur on a time scale that ranges from days to tens of years. Some transients recur periodically, others do so randomly.

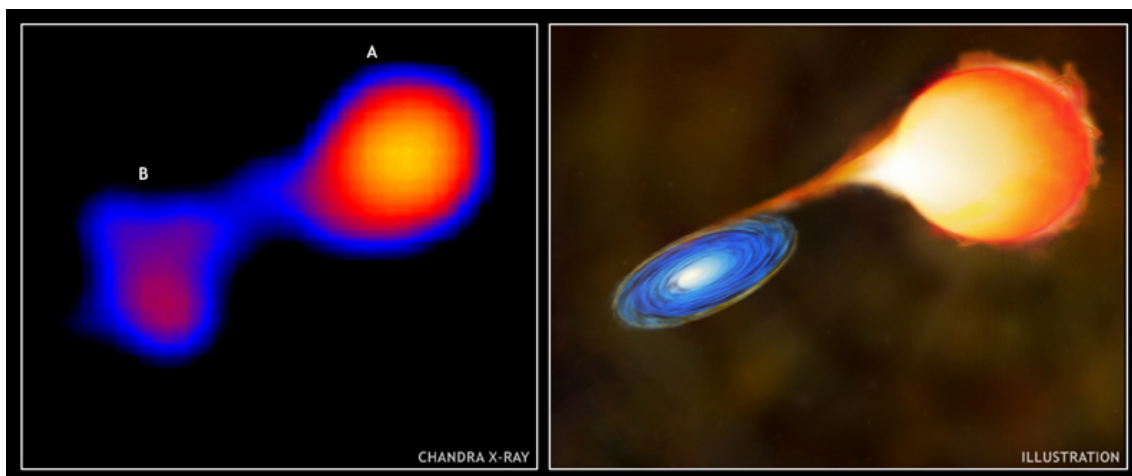


Figure 1.2: Illustration of mass transfer in a binary system. The Chandra image shows α Ceti (Mira A) (right), a highly evolved red giant star, and Mira B (left), a white dwarf. To the right of the image is an artist's conception of the Mira star system. Mira A is losing gas rapidly from its upper atmosphere via an intense stellar wind. Gas from the wind is focused into a narrow matter stream and accumulated in an accretion disk around Mira B. Collisions between rapidly moving particles in the disk produce X-rays. Credit: X-ray: M. Karovska et al. (NASA/CXC/SAO); Illustration: M. Weiss (NASA/CXC).

The flow geometry is determined by the angular momentum per specific mass of the accretion flow. If the donor star fills its critical Roche lobe, then a stream of material will be driven through the inner Lagrangian point. This stream will orbit the compact companion at a radius determined by its specific angular momentum (Lubow & Shu 1975). Viscous interactions and angular momentum conservation cause the ring to expand into a disk. The disk's outer radius is limited by tidal forces, which will transfer angular momentum back to the binary orbit.

The specific angular momentum captured from a stellar wind is determined by gradient and asymmetries in the wind across the accretion cylinder (Shapiro et al. 1976). The magnitude of the captured specific angular momentum of the stellar wind is, in comparison to the Roche lobe overflow, much smaller (Davies & Pringle 1980), and any resulting accretion disk may, depending on the circumstances, be very tenuous.

The emission from the vicinity of the compact object propagates to the observer through the surrounding environment, which modifies the spectrum by absorption and scattering. Important environmental zones are the magnetosphere of the neutron star, the accretion disk, the disk's corona/wind, the wind and/or atmosphere of the donor star and last, but not least, the interstellar medium. The prime result of this is that the X-ray spectrum undergoes substantial absorption at low energies, caused by the increasing absorption cross-section of the medium-Z elements such as iron, oxygen and carbon (Lightman & Shapiro 1976). This results in K and L absorption edges in the spectra, and emission lines from fluorescence and recombination. The relative edge to the line strength can be used to constrain the ionization state of the material, which in turn provides insight into its density and

location. Lastly, the intervening stellar medium causes low energy absorption and dust scattering halos.

1.1.1 Low mass X-ray binaries

The spectral type of the donor star determines the mode of mass transfer to the compact companion and the overall environment in the vicinity of the binary. In the low mass X-ray binaries, the donor star is typically a main sequence star with mass $M \sim M_{\odot}$ later than type A, and can, in some very evolved systems, even be a white dwarf. A late type or degenerate star does not have a natural wind strong enough to power the observed X-ray sources. Significant mass transfer will occur only if the companion fills its critical gravitational potential lobe, the Roche lobe (see in Subsection 2.1.1). X-ray heating of the accretion and the mass donor star dominates in optical, and LMXBs appear as faint blue stars – cf., e.g., Bradt & McClintock (1983) and references therein.

Members of this class are often referred to as Galactic bulge sources because they lie in the general direction of the Galactic Centre. A number of them have been identified with binary systems in globular clusters which are members of the bulge population with a distribution similar to that of the Galactic bulge stars and amongst the oldest systems in our Galaxy. All the stars with mass greater than about $1 M_{\odot}$ in these clusters have completed their evolution on the main sequence and the giant branch. Unlike the case of the cataclysmic variables (CVs), it proved much more difficult to obtain definitive evidence for the binary nature of the LMXBs. This is now understood to be a selection effect in the sense that what is observed at X-ray wavelengths is strongly dependent upon the angle of inclination i of the orbital plane of the binary to the direction of observer. The brightest and most luminous sources are those in which the inclination is small so that the orbital plane is viewed face-on. The compact X-ray source is then observed unobscured by the disc nor the binary companion but this geometry also means that it is difficult to measure radial velocities of either component and thus to determine the properties of the binary orbit. Lower luminosity X-ray sources display evidence of eclipses and 'dips' in their X-ray light curves. It is noteworthy that the ratio of X-ray to optical luminosities of such systems is much smaller than for those systems inferred to be observed at small orbital inclinations. This suggests that the X-ray emission is strongly attenuated when observed at large angles of inclination.

1.1.2 High mass X-ray binaries

In high mass X-ray binaries (HMXBs), the companion is an O or B star whose optical/UV luminosity may be comparable, or even greater than, that of the X-ray source (Conti 1978; Petterson 1978). X-ray heating is minimal, with the optical properties dominated by the donor star (sometimes called primary because of this reason and/or the mass ratio). The OB stars have a substantial stellar wind, losing 10^{-6} to $10^{-10} M_{\odot} \text{ yr}^{-1}$ with terminal velocities up to 2000 km s^{-1} . A neutron star or a black hole in a relatively close orbit will capture a significant fraction of the wind,

sufficient to power the X-ray source. The X-ray must propagate through the wind to the observer, which causes absorption in the X-ray spectrum. Roche lobe overflow can also be a supplement to the mass transfer via the stellar wind in HMXBs. However, if the mass ratio of the compact component to its donor star is greater than unity, then mass transfer via Roche lobe will become unstable $\sim 10^{-5}$ yr after it starts (cf. Savonije (1983) and references therein). Quasi-Roche lobe overflow may occur as the supergiant approaches its Roche lobe, where the reduced gravity can cause a focusing of the stellar wind towards the compact companion (Friend & Castor 1982; Hadrava 1987).

Of the 100 brightest Galactic X-ray sources, about one-quarter of them are high mass X-ray binaries (HMXBs) in the sense that the primary stars are O or B giants or supergiants. Of 26 known X-ray pulsars, 23 are associated with these classes of high mass star. Three of the HMXBs are strong candidates for containing stellar mass black holes. The O and B supergiants have large mass loss rate, and accretion takes place through the capture of a certain fraction of the outflowing material from the donor star by the compact companion.

1.1.3 X-ray spectral states

In the following Section, we will restrict ourselves to a brief description of emission states of black hole HMXBs. The emission in X-ray binaries can (and often does) vary with time. This time dependence is mostly erratic but often exhibits common characteristics. Based on the emission properties, we classify the emission into X-ray spectral states. The concept of X-ray states was introduced when Tananbaum et al. (1972) observed a global spectral change in Cygnus X-1 in which the soft X-ray flux (2-6 keV) decreased by a factor of 4, the hard flux (10-20 keV) increased by a factor of 2, and the radio counterpart turned on. Thereafter, a similar X-ray transition was observed in many other sources as well. The soft state, which was commonly described as ~ 1 keV thermal emission, was usually observed when the source was bright, thereby prompting the name High/Soft state. The hard state, with a typical photon index $\Gamma \sim 1.7$, was generally seen when the source was faint, hence the name Low/Hard state. In this state, the disk was either not observed above 2 keV, or it appeared much cooler and withdrawn from the black hole. There is also an Intermediate state between Low/Hard and High/Soft state. Usually when a source tries to undergo a transition from the Low/Hard state and the High/Soft state and fails, it enters a period of rather erratic behaviour which is classified as Intermediate state. An additional X-ray state of black hole HMXBs was identified in *Ginga*¹ observations (Miyamoto & Kitamoto 1991; Miyamoto et al. 1993). It was characterized by the appearance of several-Hz X-ray QPOs, a relatively high luminosity (e.g., $> 0.1 L_{\text{Edd}}$), and a spectrum comprised of both a thermal component and a powerlaw component that was steeper ($\Gamma \sim 2.5$) than the hard power-law. This state was named the Very High state.

Rapid observational developments challenged the prevailing views of X-ray states in black hole HMXBs. First, it was shown that the High/Soft state of Cygnus X-

¹also known as ASTRO-C was a Japanese X-ray satellite launched on February 5, 1987.

1 is not consistent with a thermal interpretation (Zhang et al. 1997); instead, the spectrum is dominated by a steep power-law component ($\Gamma \sim 2.5$). Thus, Cygnus X-1 is not a useful prototype for the High/Soft state that it helped to define. Secondly, the spectra of black hole transients near maximum luminosity were often found to exhibit a steep power-law spectrum, rather than a thermal spectrum (McClintock & Remillard 2006). Thirdly, a number of different QPO types were commonly observed over a wide range of luminosities (e.g., Morgan et al. (1997); Sobczak et al. (2000); Homan et al. (2001)). These findings attracted great interest in the nature of the Very High state.

The energy spectra of outbursting black holes often exhibit composite spectra consisting of two broadband components. There is a multi-temperature accretion disk with a characteristic temperature near 1 keV, and a power-law component with a photon index Γ . The High/Soft state (also known as "thermal state") corresponds to those times when the radiation is dominated by the heat from the inner region of the accretion disk. The High/Soft state is defined by the following conditions: (i) the disk contributes more than 75% of the total unabsorbed flux at 2–20 keV, (ii) there are no QPOs present with integrated amplitude above 0.5% of the mean count rate, and (iii) the integrated power continuum is low. In the soft state the accretion disk reaches closer to the black hole and its thermal emission is strongly increased, leading to Compton cooling of the corona. For that reason the spectrum is softer.

The Low/Hard state has been clearly associated with the presence of a steady type of radio jet. Considering the Low/Hard states for several black hole binaries allows a definition that is again based on three conditions: (i) the power-law component contributes at least 80% of the unabsorbed 2–20 keV flux, (ii) $1.5 < \Gamma < 2.1$, and (iii) the power density spectrum yields integrated rms power $r > 0.1$. In the Low/Hard X-ray state, the accretion disk component is either absent or it is modified in the sense of appearing comparatively cool and large. A possible physical explanation of the Low/Hard state is that the accretion disk is only weakly extended with a large inner radius. The emitted photons are reprocessed in a hot corona and reach high energies due to inverse Compton scattering. Thus the resulting spectrum is hard.

The particular state definition as described above is far too simplistic, as the states do not only have different spectral shapes but they differ in other characteristics as well. For our purposes, this definition is sufficient. For more detailed summary of the concept of the X-ray spectral state see e.g., Remillard (2005b); Remillard & McClintock (2006).

1.2 Cygnus X-1/HDE 226868

1.2.1 Discovery and history of observation

Cygnus X-1 is one of the brightest X-ray sources in the sky, and it is located in the constellation Cygnus. Already indicated by the first extrasolar X-ray observations (Giacconi et al. 1962; Gould & Burbidge 1963), Cygnus X-1 was discovered during a rocket flight experiment on June 16, 1964 carrying Geiger counters with

a collimator-limited field of view of 8.4° and an effective area of 906 cm^2 in the 1–15 Å range (Bowyer et al. 1965). This X-ray source was also detected with other experiments. Its nature and exact location, however, was not clear at first. Byram et al. (1966) noted a decrease of the 1–10 keV flux by a factor 4 between June 1964 and April 1965, and Overbeck & Tananbaum (1968) found an increase of the 20–50 keV flux by a factor ≤ 2 between September 1966 (Overbeck et al. 1967) and May 1967. The position of Cygnus X-1 was successively refined to a precision of 1.5° by Fisher et al. (1966), to 10 arcminutes by Giacconi et al. (1967), by Tananbaum et al. (1971) using the first X-ray satellite Uhuru, and to 30 arcseconds by Rappaport et al. (1971). Nevertheless, only the appearance of a radio source (Braes & Miley 1971; Hjellming & Wade 1971), which could be identified with the X-ray source due to its simultaneous state transition (Tananbaum et al. 1972), reduced the uncertainty of the position of Cygnus X-1 to 0.5 arcsecond and suggested the 9 mag. star HDE 226868² (V1357 Cyg) to be the optical counterpart of Cygnus X-1 (Braes & Miley 1971; Murdin & Webster 1971). Further refinements of the radio location allowed to exclude another potential counterpart (Wade & Hjellming 1972). HDE 226868 was subsequently discovered to be a spectroscopic binary with a period of 5.6 d (Webster & Murdin 1972; Bolton 1972b,a), which also shows orbital photometric variations due to tidal deformation (Walker 1972; Lyutyi et al. 1973). The orbital elements implied immediately that the dynamically constrained mass of the unseen secondary exceeds the maximal mass of neutron stars, and that the compact object in this high mass X-ray binary system must therefore be a black hole – unless Cygnus X-1 is a triple system with, e.g., a neutron star and a main sequence star orbiting around HDE 226868 (Fabian et al. 1974; Bahcall et al. 1974). The latter model, as well as other alternatives involving a subluminous stellar secondary (e.g., Bahcall et al. (1973); Avni & Bahcall (1975)), are ruled out by the non-detection of a companion with $\leq 2\%$ of HDE 226868’s luminosity (Shafter et al. 1980). Further evidences (e.g., reviewed by Oda (1977); Cowley (1992)) lead to a growing acceptance that Cygnus X-1 contains a black hole.

1.2.2 Orbital parameters

After the discovery of the radial velocity variability of HDE 226868 (Webster & Murdin 1972; Bolton 1972b,a), spectroscopic and photometric follow-up observations allowed to improve the accuracy of the orbital period (e.g., Bolton (1975); Guinan et al. (1979); Gies & Bolton (1982); Sowers et al. (1998)). The claim of a period change by Ninkov et al. (1987) could not be confirmed. LaSala et al. (1998) suggested that the supposed much larger value of 5.60172(3) days is just a typographical error and should actually read 5.6002 days. The measurement

$$P_{\text{orb}} = 5.599829(16) \text{ days} \quad (1.1)$$

of Brocksopp et al. (1999) is also used for the most recent ephemerides, which define an epoch of orbital phase $\Phi = 0$, i.e., superior conjunction of the black hole, at

²The Henry Draper Extension (HDE, published between 1925–1936, see Cannon (1936)) is an expansion of the Henry Draper Catalogue (HD, 1918–1924). There are more than 350 000 stars classified in the Henry Draper Extension Charts (HDEC, 1937–1949).

heliocentric dates of

$$T_0 = \text{MJD } 51729.949(8) \equiv 2000-07-04, 22:58 \pm 11 \text{ min (Gies et al. 2003) }, (1.2)$$

$$T_0 = \text{MJD } 52872.288(9) \equiv 2003-08-21, 06:54 \pm 13 \text{ min (Gies et al. 2008) }. (1.3)$$

An eccentric orbit, with an eccentricity up to $e = 0.09 \pm 0.02$ (Bolton 1972a), was suggested from the first observations (also by Bolton (1975); Hutchings (1978), though with lower e values), but could not be confirmed by later studies finding circular orbits. Gies & Bolton (1982) admitted that their "*earlier result was an artefact of poor phase distribution of the data and inadequate analysis*".

The inclination i of the system, however, is not accurately determined. Davis & Hartmann (1983) find $i = 36^\circ\text{--}67^\circ$ from the change of the C IV UV line between the conjunction phases. Gies & Bolton (1986a) inferred $i = 28^\circ\text{--}38^\circ$ from the photometric modulation and the rotational broadening of photospheric absorption lines. Dolan & Tapia (1989) obtained $i = 62^\circ$ (with a 90% confidence interval of $i = 25^\circ\text{--}67^\circ$) from the polarization of the R, G, B fluxes (see also Dolan (1992)). Wen et al. (1999) concluded $i = 10^\circ\text{--}40^\circ$ from the orbital modulation of the X-ray flux. Gies et al. (2003) get $i = 30^\circ \pm 7^\circ$ from the velocity components of H α P-Cygni line profile. Abubekurov et al. (2004) derive $i = 31^\circ\text{--}44^\circ$ from the radial velocity curve of a Roche model. Given all of these estimates, the following often adopted value

$$i = 35^\circ \tag{1.4}$$

seems to be well-justified.

1.2.3 Mass loss

Walborn (1973) classified HDE 226868 as O9.7 Iab star, as it shows a peculiar and variable emission line at $\lambda = 4686 \text{ \AA}$ (Brucato & Kristian 1972; Bolton 1972a). This line corresponds to the Paschen α transition between the $n = 4$ and $n = 3$ states of singly ionized helium. As its radial velocity curve lags the motion of the primary, the He II $\lambda = 4686 \text{ \AA}$ emission has been identified with an enhanced flow of matter from the supergiant to the black hole (Hutchings et al. 1973; Bisiacchi et al. 1974; Bolton 1975; Aab 1983; Gies & Bolton 1986a,b; Ninkov et al. 1987; Karitskaya et al. 2005). Such a focused wind is expected for a star in a binary system that almost fills its critical Roche lobe. Friend & Castor (1982) estimated the total mass loss rate of Cygnus X-1 to be $2 \times 10^{-6} M_\odot \text{ yr}^{-1}$. This value is supported by the results of Canalizo et al. (1995), who assumed that the relationship between the radial velocity curve of several lines and their excitation potentials measures the mass loss.

The H α line (at $\lambda = 6563 \text{ \AA}$) shows a much more complex variability than He II $\lambda = 4686 \text{ \AA}$. Its profile consists of a P-Cygni component from the supergiant, and an emission component from the focused wind (Brucato & Zappala 1974; Hutchings et al. 1974; Sowers et al. 1998; Hadrava 2007). As these components follow different radial velocity curves, their superposed profile varies with orbital phase. Furthermore, these components vary in strength. Apart from the orbital variability (due to photo-ionization – cf., e.g., Tarasov et al. (2003)) and short-term variability

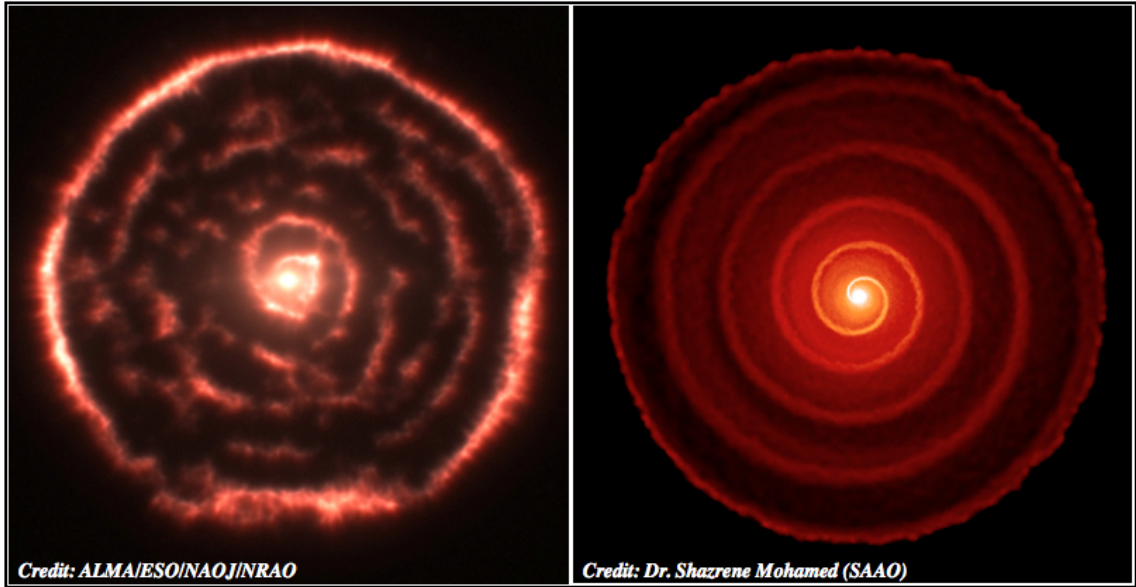


Figure 1.3: Illustration of mass loss in a binary system. On the left is the ALMA observation of circumstellar environment of R Sculptoris and on the right is a cross-section through the three-dimensional hydrodynamic simulation of the interacting binary star system.

(e.g., because of wind clumping), the strength of the $H\alpha$ emission is anti-correlated with the soft X-ray flux of Cygnus X-1 (Voloshina et al. 1997; Tarasov et al. 2003; Gies et al. 2003, 2008; Yan et al. 2008). That is, the $H\alpha$ emission is strongest in the Low/Hard state and, vice versa, flares or High/Soft state only occur when the $H\alpha$ emission is weak. Yan et al. (2008) disentangle the $H\alpha$ complex into a P-Cygni profile and an emission component, and find that the variation in strength between the High/Soft state in 2004 and the hard state in 2006 is largely due to the focused wind's emission component. Gies et al. (2003), on the other hand, find the strength of the emission to be correlated with that of the P-Cygni component. Vrtilik et al. (2008) pointed out, however, that the Low/Hard and High/Soft states do not necessarily differ strongly in mass accretion rate, as the bolometric X-ray luminosity remains roughly constant.

The photo-ionization and velocity of the wind can be probed with UV observations of line profiles, which usually show wide P-Cygni profiles because of the wind acceleration. In the presence of the X-ray source, these lines are strongly suppressed at $\Phi = 0.5$ when the line of sight to the supergiant passes through the photo-ionized region (Hatchett & McCray 1977). The ions that would give rise to a large opacity in the UV band are completely ionized, and the wind cannot reach a high velocity. So far, the only measurements in the hard state are from the International Ultraviolet Explorer (IUE, 1978-1996). These are mostly low-dispersion spectra (Treves et al. 1980), as HDE 226868 was not bright enough to produce a good signal to noise ratio in high-resolution spectra (Davis & Hartmann 1983). High-dispersion UV spectra during the High/Soft state were obtained with HST STIS (Vrtilik et al. 2008; Gies et al. 2008; Caballero-Nieves et al. 2009). Whereas Davis & Hartmann

(1983) derived a terminal velocity of 2300 km s^{-1} on the shadowed side and only $\sim 1500 \text{ km s}^{-1}$ on the hemisphere facing the X-ray source from the Low/Hard state IUE data, Gies et al. (2008) are able to model their High/Soft state HST spectra assuming that the wind of HDE 226868 is fully restricted to the shadow wind from the shielded side of the stellar surface (Blondin 1994). Based on a comparison with low-dispersion IUE spectra, Gies et al. (2008) suggested that the orbital variation of the line strength is the same across the states, and therefore concluded that the radiatively driven wind is "probably always weak or absent" on the side directed toward the black hole. Nevertheless, the claim that there is no spherical wind at all seems not justified in the Low/Hard state, where we observe the orbital modulation of the soft X-ray flux due to absorption in the stellar wind, probably not related to the focused wind. The detailed dynamics of the stellar wind and its interaction with the X-ray source are thus still far from being resolved and understood in a self-consistent picture. The Low/Hard state is lacking UV spectra comparable to the HST STIS data from the High/Soft state, which could firmly constrain the wind structure. Given all the results reviewed above, the stellar wind distribution, its properties and dynamics are clearly sensitive to the X-ray state, if not even the physical cause of the Low/Hard and High/Soft states in the HMXBs.

Chapter II

Related topics in stellar astrophysics

Before we start to investigate properties of the X-ray binary environment, we will mention some general facts from stellar astrophysics which will become relevant in the further course of this thesis. Sec. 2.1 briefly outlines the theory of the Roche potential which determines the shape of close binaries. An overview on stellar wind theory, and line-driven wind from early-type stars in particular, is given in Sec. 2.2. Finally, Sec. 2.3 presents a brief overview of accretion phenomena with a special emphasis put on the accretion of axially symmetric stationary flow onto a compact object.

2.1 Restricted three-body problem

The shape of a star in a binary system whose rotation is synchronized with its circular orbit, is determined by the effective potential in the co-rotating reference frame – the so-called Roche potential (named after the French astronomer Édouard Albert Roche, 1820–1883). It consists not only of gravity of the two bodies with masses M_1 and M_2 (at positions of \mathbf{r}_1 and \mathbf{r}_2 , respectively), but also takes into account the centrifugal potential due to the orbital motion with the Keplerian angular velocity

$$n = \sqrt{\left(\frac{G(M_1 + M_2)}{a^3}\right)}, \quad (2.1)$$

around the barycentre of the system. Here, a represents the orbital separation of components of the binary. Hereafter, we will assume $M_1 \geq M_2$, without loss of generality, and we will probe the effective potential with a test particle with a mass $m_3 \ll M_2$. The well-know system of differential equations governing the so-called restricted three-body problem in the Cartesian coordinates rotating in the xy -plane

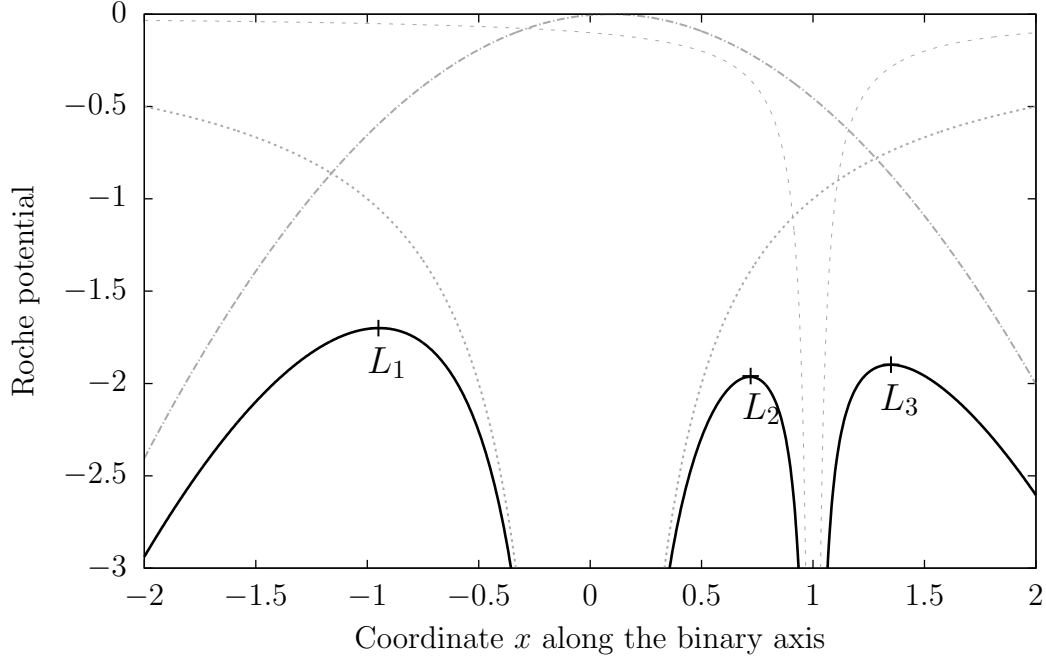


Figure 2.1: Scaled Roche potential of Eq. (2.5) (solid black line) for $q = 0.1$ along the axis connecting the two components of the binary, together with its components (grey lines). The gravitational potential of M_1 (dotted line), the gravitational potential of M_2 (dashed line), and centrifugal potential (dashed–dotted line). Black crosses mark the positions of the Lagrangian point L_1 , L_2 , and L_3 .

is given by

$$\begin{aligned} \ddot{x} - 2n\dot{y} &= \frac{\partial\Omega}{\partial x}, \\ \ddot{y} + 2n\dot{x} &= \frac{\partial\Omega}{\partial y}, \\ \ddot{z} &= \frac{\partial\Omega}{\partial z}, \end{aligned} \quad (2.2)$$

where Ω represents the potential function

$$\Omega(x, y, z) = \frac{GM_1}{r_1} + \frac{GM_2}{r_2} + \frac{1}{2}n^2(x^2 + y^2), \quad (2.3)$$

and $r_{1,2}$ given by

$$\begin{aligned} r_1^2 &= \left(x + \frac{M_2 a}{M_1 + M_2}\right)^2 + y^2 + z^2, \\ r_2^2 &= \left(x - \frac{M_1 a}{M_1 + M_2}\right)^2 + y^2 + z^2, \end{aligned} \quad (2.4)$$

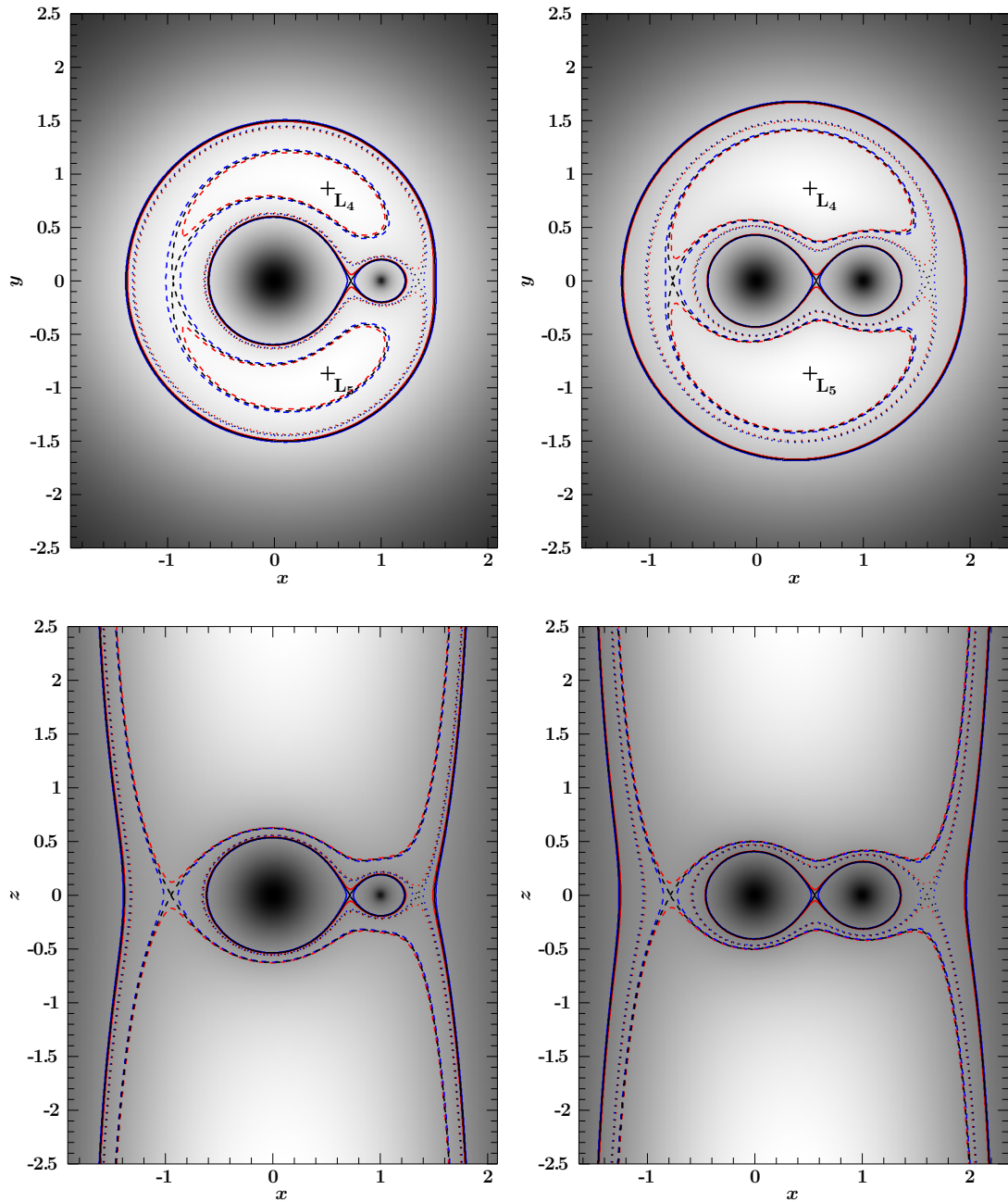


Figure 2.2: Roche potential in the xy -plane at $z = 0$ (top panels) and in the xz -plane at $y = 0$ (bottom panels) for $q = 0.1$ (left panels) and $q = 0.67$ (right panels), respectively. Brighter colors mean higher values of the Roche potential. The black solid line shows the Roche lobes - the equipotential surface passing through the L_1 point. The black dotted and dashed lines show the equipotential surfaces passing through the L_2 and L_3 points, respectively. The blue (red) lines show the corresponding equipotential surfaces at 0.5% lower (higher) potential. The triangular Lagrange points L_4 and L_5 , which are the global maxima of the Roche potential in the orbital plane, are indicated by labelled crosses. Credit to M. Hanke.

are the distances of any arbitrary point from the two centres of masses M_1 and M_2 . Hereafter, we assume a circular orbit, therefore, a remains constant. The three terms constituting the right-hand side of Eq. (2.3) represent the contributions of the attraction of the masses M_1 and M_2 , and of the centrifugal force. If we use dimensionless coordinates and transpose the origin from the centre of the system to the centre of mass M_1 , therefore $(\xi, \eta, \zeta) = \frac{1}{a}(x - M_2 a / (M_1 + M_2), y, z)$, the total potential of forces acting on any arbitrary point can be rewritten as

$$\frac{a}{GM_1} \Psi_{\text{eff}}(\xi, \eta, \zeta) = -\frac{1}{\rho_1} - \frac{q}{\rho_2} - \frac{1+q}{2} \left\{ \left(\xi - \frac{M_2}{M_1 + M_2} \right)^2 + \eta^2 \right\}, \quad (2.5)$$

where now

$$\begin{aligned} \rho_1^2 &= \xi^2 + \eta^2 + \zeta^2, \\ \rho_2^2 &= (\xi - 1)^2 + \eta^2 + \zeta^2, \end{aligned} \quad (2.6)$$

represent distances from the mass centres M_1 and M_2 , respectively, in units of a . Moreover, we can express Ψ_{eff} in spherical coordinates centred at M_1 as

$$\Psi_{\text{eff}}(r, \theta, \phi) = -\frac{GM_1}{a} \left\{ \frac{1}{r} + \frac{q}{\sqrt{1 - 2\lambda r + r^2}} - qr\lambda + \frac{1}{2}(1+q)r^2(1 - \nu^2) \right\}, \quad (2.7)$$

where

$$\begin{aligned} \xi &= r \cos \phi \sin \theta = r\lambda, \\ \eta &= r \sin \phi \sin \theta = r\mu, \\ \zeta &= r \cos \theta = r\nu; \end{aligned} \quad (2.8)$$

and where we have substituted for

$$q = \frac{M_2}{M_1} \leq 1. \quad (2.9)$$

The potential in Eq. (2.5) has five critical points where $\nabla \Psi_{\text{eff}} = 0$, which are called Lagrangian points L_1 – L_5 (after Italian mathematician and astronomer Joseph-Louis Lagrange, 1736–1813). As $\partial \Psi_{\text{eff}} / \partial z = z \cdot f(x, y, z)$ with $f(x, y, z) \geq 0$, all of them are found in the xy -plane. Fig. 2.1 shows the Roche potential along the binary x -axis, where the three saddle points L_1 , L_2 , and L_3 are located. Fig. 2.2 visualizes $\Psi_{\text{eff}}(\mathbf{r})$ in the xy - and xz -planes for different mass-ratios $q = 0.1$ and 0.67 , the latter corresponding to the HDE 226868/Cygnus X-1 system. The upper plots show the triangular Lagrange points L_4 and L_5 at $(x, y) = (1, \pm\sqrt{3})/2$ to be the global maxima of the potential.

2.1.1 Roche lobes

The critical Roche lobes are those equipotential surfaces around M_1 and M_2 that connect at L_1 . Matter inside each Roche lobe, that is co-rotating with the binary, is

Table 2.1: Characteristics of Roche lobes

q	V_{rel}	V	r_{eff}	r_{max}	r_{min}	r_x^+	r_x^-	r_y	r_z
0.1	1.00	0.81458	0.57936	0.71355	0.53366	0.71355	0.61341	0.59516	0.53376
	0.95	0.77389	0.56955	0.65863	0.52693	0.65863	0.60118	0.58447	0.52703
	0.90	0.73327	0.55940	0.63189	0.51977	0.63188	0.58863	0.57337	0.51986
	0.80	0.65182	0.53787	0.58971	0.50399	0.58971	0.56245	0.54987	0.50407
	0.70	0.57037	0.51446	0.55261	0.48608	0.55261	0.53469	0.52451	0.48615
	0.60	0.48892	0.48871	0.51668	0.46555	0.51668	0.50492	0.49687	0.46561
	0.50	0.40748	0.45991	0.47996	0.44171	0.47996	0.47243	0.46628	0.44175
	0.25	0.20379	0.36506	0.37163	0.35778	0.37163	0.36988	0.36754	0.35779
	0.10	0.08154	0.26900	0.27073	0.26684	0.27073	0.27041	0.26972	0.26684
0.667	1.00	0.30026	0.41540	0.53863	0.38930	0.53863	0.44102	0.41157	0.38967
	0.95	0.28528	0.40837	0.49047	0.38413	0.49047	0.43244	0.40511	0.38448
	0.90	0.27024	0.40107	0.46798	0.37859	0.46797	0.42349	0.39825	0.37891
	0.80	0.24029	0.38567	0.43368	0.36651	0.43368	0.40480	0.38355	0.36678
	0.70	0.21027	0.36889	0.40425	0.35287	0.40425	0.38483	0.36730	0.35309
	0.60	0.18021	0.35040	0.37632	0.33735	0.37632	0.36330	0.34923	0.33752
	0.50	0.15016	0.32973	0.34829	0.31948	0.34829	0.33979	0.32890	0.31960
	0.25	0.07508	0.26171	0.26775	0.25760	0.26774	0.26567	0.26144	0.25764
	0.10	0.03005	0.19286	0.19444	0.19164	0.19443	0.19404	0.19278	0.19165

Notes: Parameters of the Roche equipotential surfaces for different values of q around mass centre M_1 . All distances are in units of the orbital separation a . The filling factor V_{eff} is a ratio of the particular volume of star to the volume of its critical Roche lobe. V is the actual volume of a given equipotential in units of a^3 . r_{eff} is the effective radius of a sphere with the same volume. r_{min} and r_{max} represent minimum and maximum distances of the equipotential from the centre of mass. r_x^+ , r_x^- , r_y , and r_z correspond to distances between the centre of star and the intersection of the equipotential surface with the x -axis (in the (+) and (-) directions), y -axis, and z -axis, respectively.

bound to the corresponding mass. Moreover, the fact that the equipotential surfaces are also the zero-velocity surfaces will render them to represent free surfaces in the case when the volume enclosed by such surface is filled with tenuous gas of mass small enough not to contribute to the gravitational potential. If such configurations are to be in hydrostatic equilibrium, the surfaces of constant pressure P and density ρ must be equipotentials. The same must be true for the external surface of a star, at which P and ρ must vanish at the same time; therefore, the surface of the components in the close binary that are in hydrostatic equilibrium are given by an equation of the form of Eq. (2.3) or Eq. (2.7). The shape of a star will, then, notably deviate from a sphere if the star fills a significant fraction of the Roche lobe volume. Table 1.1 lists geometrical parameters of a selection of such equipotential surfaces and Fig. 1.3 shows projections of a 3-dimensional Roche lobe and an equipotential surface that encloses 90% of the Roche lobe volume, which is the estimated filling factor for HDE 226868.

The size of the Roche lobe around M_1 is often parametrized in units of the effective radius r_{eff} of a sphere with the corresponding volume. A general approximation, accurate to $< 1\%$, was found by Eggleton (1983).

$$r_{\text{eff}}(q) \approx \frac{0.49}{0.6 + q^{\pm 2/3} \log(1 + q^{\mp 1/3})}. \quad (2.10)$$

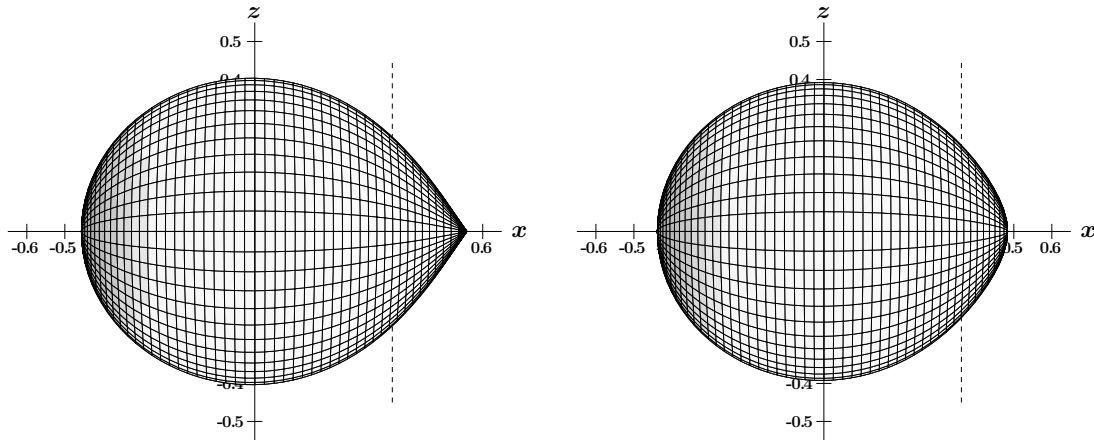


Figure 2.3: Roche equipotential surfaces for $q = 0.667$ with 100% (left) and 90% (right) Roche lobe volume filling factors. The objects are seen in a parallel projection along the y -direction. The dashed line is the binary system's rotation axis.

2.2 Stellar wind

This Section presents a brief overview of some basic contemporary concepts of the stellar wind. An early review is given by (Cassinelli 1979), and more recent details can be found in the textbook by Lamers & Cassinelli (1999).

Stellar winds are the continuous outflow of material from stars. During most of their existence, stars are basically in hydrostatic equilibrium, where the pressure gradient enhanced by the energy release in the core balances the gravitational contraction. But even during the steady phases of their evolution, most stars lose constantly mass from their outer atmosphere through stellar winds. The ejection of material plays a major role in the life cycle of stars. When a central fusion process is exhausted, the star may undergo a vast restructuring, sometimes involving an ejection of its outer layers (e.g., red giants, planetary nebula) or even its total disruption in a cataclysmic supernova explosion. In the case of massive stars, the winds can remove more than half of the star's original mass before the star explodes as supernova.

There are many mechanisms that can lead a star to eject matter in the form of a steady stellar wind. Due to its hydrodynamic nature, its connection to the problem of radiative transport, and sometimes even magnetic field, stellar wind is a highly complex phenomenon. Distinct theories have been presented to explain the mass-loss for various stars. Different spectral types of stars are dominated by different physical processes where we may apply appropriate approximations.

- *Winds from main sequence stars.* Stars similar to the sun have a low rate of mass loss: $\dot{M} \sim 10^{-14} M_{\odot} \text{ yr}^{-1}$. The asymptotic velocity v_{∞} of the wind is

comparable to the escape velocity v_{esc} . The prototypical star in this category is the Sun. Thermal winds are driven by the gradient of the gas pressure. This requires a high pressure in the wind formation zone which may be created, e.g., by dissipation of sound waves or by radiative heating of the gas. Models of pressure-driven winds were developed in an early attempt to understand the newly-discovered solar wind.

- *Winds from hot, luminous stars.* Stars with temperature of photosphere $T_{\text{eff}} \geq 15,000$ K, and luminosity $L \geq 3000 L_{\odot}$ have a high rate of mass loss: $\dot{M} \sim 10^{-7} - 10^{-5} M_{\odot} \text{ yr}^{-1}$. Their winds are very fast, with $v_{\infty} > v_{\text{esc}}$. Wolf-Rayet (WR) stars or very young and luminous O and B supergiants fall into this category. WR stars are hot, luminous stars with extended envelopes; their mass loss rates $\dot{M} \sim 10^{-5} M_{\odot} \text{ yr}^{-1}$ and wind terminal velocities $v_{\infty} \sim 2500 \text{ km s}^{-1}$ are among the largest observed for any type of star. Winds from hot stars are thought to be driven by radiation pressure. Radiation driven winds receive their momentum directly from the radiation field of the star by absorbing the outwards-directed stellar radiation and re-emitting photons into all directions. This creates a net force (radiation pressure) directed away from the star. This is probably the most efficient mass-loss mechanism for luminous stars.
- *Winds from cool, luminous stars.* Stars with $T_{\text{eff}} \leq 6000$ K and $L \geq 100 L_{\odot}$ have a high rate of mass loss: $\dot{M} \sim 10^{-8} - 10^{-5} M_{\odot} \text{ yr}^{-1}$. The wind velocity, however, is very low, typically on the order of $v_{\infty} \sim 10 - 30 \text{ km s}^{-1}$ corresponding to the low surface gravity of these extended objects. The mechanism that drives the wind from cool stars is uncertain; possible sources of opacity in winds of evolved cool stars (typically K and M giants and supergiants) are molecules and dust grains which form in the upper layers of the atmospheres. If dust grains provide the main source of opacity the outflow is called a dust-driven wind. For stars on the asymptotic giant branch (AGB) observations suggest a correlation of pulsation and mass-loss. Most of the stars are known to be large-amplitude pulsators (long-period variables, Mira-type stars). The stellar pulsation creates shock waves in the atmosphere which lead to a levitation of the outer atmospheric layers, i.e. relatively high densities at low temperatures. In this environment molecules and dust grains can form efficiently and provide the necessary opacity to drive a massive slow wind.
- *Winds from extremely young stars.* T Tauri stars have mass loss rates of $\dot{M} \sim 10^{-9} - 10^{-7} M_{\odot} \text{ yr}^{-1}$. The wind velocity is $v_{\infty} \sim 200 \text{ km s}^{-1}$. T Tauri stars have circumstellar disks that might be accretion disks. The strength of the wind is correlated with the luminosity of the disk; this suggests that the outgoing wind might be powered by the accretion disk.

2.2.1 Hydrostatic equilibrium

First, let us find the conditions when a star's atmosphere is in the hydrostatic equilibrium with its surroundings. The problem is hydrodynamic in its nature,

therefore we will utilize the Navier-Stokes equation (named after the French engineer and physicist Claude-Louis Navier, 1785-1836, and the Irish mathematician and physicist Sir George Gabriel Stokes, 1819-1903), which describes the conservation of momentum for an incompressible flow:

$$\rho \frac{d\mathbf{v}}{dt} \equiv \rho \left(\frac{\partial \mathbf{v}}{\partial t} + (\mathbf{v} \cdot \nabla) \mathbf{v} \right) = -\nabla P + \mu \nabla^2 \mathbf{v} + \mathbf{f} , \quad (2.11)$$

where ρ represents density, \mathbf{v} is the velocity field, P is pressure, μ is dynamic viscosity, and \mathbf{f} is the external force density. In our simplified case of hydrostatic equilibrium, we may consider the material within the star's atmosphere to be steady ($\partial \mathbf{v} / \partial t = 0$), spherically symmetric ($\partial / \partial \vartheta = \partial / \partial \varphi = 0$, therefore, $\nabla \rightarrow \hat{e}_r d/dr$), inviscid ($\mu = 0$), and static ($\mathbf{v} = 0$). Assuming an isolated spherically symmetric star, its gravity is given by the gravitational potential $\Phi(r) = -GM/r$, the force acting on an element of matter is equal to $f = -\rho \nabla \Phi$. In this case, the Eq. (2.11) reads

$$\frac{dP}{dr} = -\rho \frac{GM}{r^2} , \quad (2.12)$$

which represents the hydrostatic equilibrium equation. Moreover, if we assume an ideal gas with the equation of state given by $P = a^2 \rho$, where a is constant in the case of the isothermal atmosphere, we arrive to the simple differential equation

$$a^2 \frac{d\rho}{dr} = -\rho \frac{GM}{r^2} , \quad (2.13)$$

which represents the equation of hydrostatic equilibrium. The solution of this equation reads

$$\rho = \rho_0 \exp \left(\frac{GM}{ra^2} \right) . \quad (2.14)$$

Thus, we can conclude that if we disregard physically uninteresting case of $\rho_0 = 0$ and, by extension, $\rho = 0$ for every r , for $r \rightarrow \infty$, ρ goes to a non-zero positive value ρ_0 . Therefore, the necessary condition for hydrostatic equilibrium within the star's atmosphere is non-zero density far away from the star. It is clear then, that at certain distance from the star, the thermal motion of particles of the gas will exceed the escape velocity. The gas will not be gravitationally bounded any more and will escape the star's gravitational field. This continual expansion is called the stellar wind.

2.2.2 Parker's model

We will consider a simple model for an expanding stellar wind which can be treated analytically. The pressure gradient dp/dr drives the hydrodynamic expansion of the outer atmosphere of stars with strong coronal heating like the Sun (as originally proposed by Parker (1958, 1960)). The model is based on the following assumptions: the outflow is stationary and spherically symmetric. We also assume the stellar atmosphere to be isothermal. The general form of the mass continuity equation reads

$$\frac{\partial \rho}{\partial t} + \nabla \cdot (\rho \mathbf{v}) = 0 . \quad (2.15)$$

In our case, we assume the velocity field in the form of $\mathbf{v} = v(r)\mathbf{r}/r$, with the only non-zero component in the r -direction. The previous equation, thus, can be transformed into

$$\nabla^i \left(\frac{\rho(r)v(r)}{r} r^i \right) = \frac{1}{r^2} \frac{d}{dr} (\rho(r)v(r)r^2) = 0 . \quad (2.16)$$

From Eq. (2.16) we conclude

$$\rho(r)v(r)r^2 = -\frac{\dot{M}}{4\pi} = \text{const.}, \quad (2.17)$$

where the constant on the right-hand side of the equation represents the amount of matter flowing in or out a unit solid angle per unit time. The constant is positive for the stellar wind, and negative in the case of spherically symmetric accretion.

From Eq. (2.11), we obtain the radial form of the equation of conservation of momentum for $v = v(r)$

$$\rho v \frac{dv}{dr} = -\frac{dP}{dr} - \rho \frac{d\Phi}{dr} , \quad (2.18)$$

where P denotes the total pressure – gas pressure as well as radiation pressure due to the Thomson scattering of the star's radiation field on free electrons. The total pressure, thus, reads $P = P_g + P_r$. From the theory of the radiative transport, we get expression for the radiation pressure gradient

$$\frac{dP_r}{dr} = -\frac{\rho\kappa L}{4\pi r^2 c} , \quad (2.19)$$

where κ is the continuum opacity, L is the luminosity of the star, and c denotes the speed of light. In order to find the gas pressure gradient, we will assume (similarly to the previous Section) the material of the wind to be governed by the equation of state of the ideal gas which generally reads

$$P_g(\rho, T) = a^2(T) \rho , \quad (2.20)$$

where again if we assume the isothermal case, a becomes a constant independent on T and r . By derivation of the previous equation, we arrive to an simple expression for the gas pressure gradient

$$\frac{dP_g}{dr} = a^2 \frac{d\rho}{dr} . \quad (2.21)$$

To specify the density gradient $d\rho/dr$, we will make use of Eq. (2.16), from which we can obtain

$$\frac{dP_g}{dr} = a^2 \left(-\frac{\rho}{v} \frac{dv}{dr} - \rho \frac{2}{r} \right) . \quad (2.22)$$

By using Eq. (2.19), and Eq. (2.22), we can express Eq. (2.18) in form of

$$\left(v - \frac{a^2}{v} \right) \frac{dv}{dr} = -\frac{GM}{r^2} + \frac{2a^2}{r} + \frac{\kappa L}{4\pi r^2 c} . \quad (2.23)$$

The first and third terms in the right-hand side of the equation show the same functional dependency on r . We can, thus, join both terms together by introducing parameter Γ

$$\Gamma = \frac{\kappa L}{4\pi GMc} , \quad (2.24)$$

which represents the ratio of the luminosity of the star to its Eddington luminosity, and create a kind of effective gravitational force which is weakened by the pressure gradient of the star's continuum radiation field.

$$\left(v - \frac{a^2}{v} \right) \frac{dv}{dr} = -\frac{GM(1-\Gamma)}{r^2} + \frac{2a^2}{r} . \quad (2.25)$$

By integrating the equation we obtain

$$F(v) = \Phi_k - \Phi_m(r) , \quad (2.26)$$

where the function $F(v)$ in the left-hand side of the equation, in the case of isothermal atmosphere and $a = kT/m$, reads

$$F(v) = \frac{1}{2} (v^2 - v_k^2) - \frac{k_B T}{m} \ln \left| \frac{v}{v_k} \right| . \quad (2.27)$$

where k_B is the Boltzmann constant, and m is the mass of the particle of the gas. The right-hand side of Eq. (2.26) represents a modified potential, which for constant opacity κ reads

$$\Phi_m(r) = -\frac{GM(1-\Gamma)}{r} - 2\frac{kT}{m} \ln r . \quad (2.28)$$

The both sides of Eq. (2.26) reach their minimum values in the critical point

$$r_c = \frac{GM(1-\Gamma)}{2a^2} , \quad (2.29)$$

where the condition $v = a$ or $dv/dr = 0$ must be satisfied. Similarly in the sonic point where $v = a$, r either equals to r_c or $dv/dr \rightarrow \infty$.

2.2.3 Line-driven wind model

In order to drive a substantial stellar wind by radiation pressure gradient usually two requirements have to be fulfilled: a high stellar luminosity and the presence of efficient absorbers (high opacity). Compared to the Parker's model of the stellar wind as discussed in the previous Section, the equation of motion for a line-driven wind contains an additional term accounting for the line absorption and scattering of the star's radiation field. To calculate the radiation pressure of lines we must know the frequency-dependent radiative flux at every point in the wind. The computation of the flux, however, can only be performed for a known spatial structure of density, temperature and velocity fields (Doppler shifts). Therefore, the modelling of line-driven winds in general requires a simultaneous (or iterative) solution of both, the equations of hydrodynamics and the equations of radiative transfer. In certain

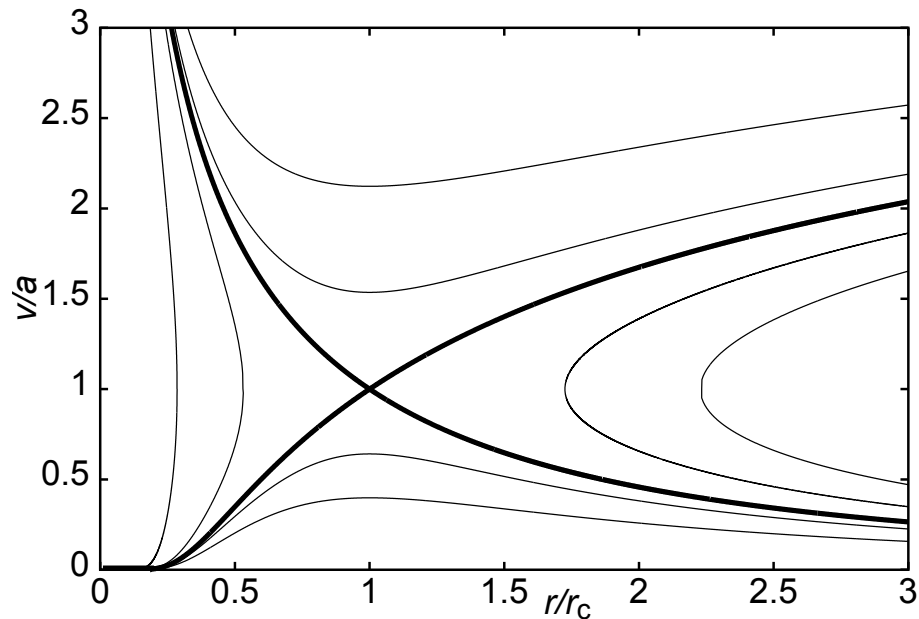


Figure 2.4: Graphical interpretation of Eq. (2.25) of the Parker's model of the stellar wind. Velocity is expressed in the units of isothermal sound speed a , and the distance from the star in units of the critical point r_c .

cases, i.e. if molecules or dust grains are important sources of opacity, it may even be necessary to include a (non-equilibrium) description of chemistry or a (time-dependent) treatment of dust formation. In contrast to the simple Parker's model of the stellar wind which we studied in the preceding Section, a general analytical solution of the problem of line-driven wind is not possible, and one has to resort to numerical simulations.

The most commonly used model of stellar winds from massive early-type stars has been introduced by Castor, Abbott and Klein (Castor et al. 1975, hereafter CAK). This model describes the mass-loss driven by line absorption and scattering of star's radiation field. It is based on a simple parametrization of the line force (by parameters α and k) which represents the contribution of spectral lines to the radiative acceleration by a power law distribution function.

In a rapidly expanding stellar wind, where the radial velocity gradient is assumed to be large, the line optical depth τ_L in the radial direction can be reduced to a purely local quantity (Castor 1974)

$$\tau_L = \rho v_{\text{th}} \kappa_L \left(\frac{dv}{dr} \right)^{-1}. \quad (2.30)$$

κ_L is the monochromatic line opacity per unit mass, v_{th} is the thermal velocity of the ions in the wind, ρ and v are the density and the velocity of the wind material. We can introduce two new variable. The local optical depth parameter t which is independent of the line strength, and, in the case of expanding atmosphere, is given by

$$t = \sigma_e \rho v_{\text{th}} \left(\frac{dv}{dr} \right)^{-1}, \quad (2.31)$$

where the quantity σ_e is the electron scattering coefficient. The second variable is the ratio of the line opacity coefficient κ_L to the electron scattering coefficient σ_e

$$\eta = \frac{\kappa_L}{\sigma_e} . \quad (2.32)$$

Then, as a consequence,

$$\tau_L = \eta t . \quad (2.33)$$

Following Castor (1974), under the assumption of the Sobolev approximation, the total force due to lines can be approximated as

$$f_{\text{rad}} = \frac{\sigma_e L_*}{4\pi cr^2} M(t) , \quad (2.34)$$

where L_* is the luminosity of the primary star, and

$$M(t) = kt^{-\alpha} \quad (2.35)$$

is the force multiplier function of the local optical depth parameter t which is a convenient means of parametrizing the line force, often used in wind calculations. α represents the slope and k the amplitude of $M(t)$, at $t = 1$ (i.e., $k = M(1)$).

Abbott (1982) improved this theory calculating the line force considering the contribution of the strengths of the hundreds of thousands of lines. He also included a third parameter (δ) that takes into account the changes in ionization throughout the wind. Despite this immense effort to give a more realistic representation of the line force, evident discrepancies with observational data still remained.

2.3 Accreting compact objects

Accretion process onto a compact companion – a black hole or a neutron star – is one of the most important concepts for understanding a variety of phenomena in the universe. The importance of accretion as a power source can be easily recognized in the study of binary systems, especially X-ray binaries. A lot of progress has been made in the understanding of accretion has been made since 1960's when the theoretical studies on black hole accretion flows were initiated. The classical picture of accretion disks was established in 1970's. The X-ray binaries were always used as a laboratory - a sort of a controlled environment in which the accretion process could be studied in detail. The reason for this is simply that, by their very nature, X-ray binaries reveal more about themselves, notably their masses and dimensions, than other astronomical objects do. This is particularly true in the case of eclipsing binaries, where we get direct observation about spatial relations within the source. The importance of accretion is further manifested by the realization that probably a majority of all stars are members of binary systems which, at certain stage of their evolution, undergo mass transfer.

The detailed studies of interacting binaries have revealed the importance of angular momentum in accretion. In many cases, the transferred material cannot land on the accreting star until it has rid itself of most of its angular momentum. This

leads to the formation of accretion disks, which turn out to be efficient machines for extracting gravitational potential energy and converting it into radiation. This property has made accretion disks attractive candidates for the role of the central engine in quasars and active galactic nuclei. The existence as well as the importance of the accretion process in the X-ray binaries is well attested through observation. A relativistic accretion disk is a concept well established within the standard picture of X-ray binaries but. In the context of this study, however, it is not the most relevant one. We do not aspire to an ambition to create an all-encompassing realistic simulation of the accretion disk around a compact companion. The computational limitations prevent us from adopting finer grid which would allow us to resolve the accretion process in more detail. We will rather concentrate on a non-spherical accretion onto a moving black hole – a process which we apply directly to our simulations later. We will briefly introduced a concept of spherical flow onto a stationary accretor, followed by a discussion of the non-spherical accretion onto moving accretor. For the complexity of the topic which is clearly beyond the scope of this study, we will not attempt to provide a reader with an introduction to accretion disks. For excellent overview of the physics of the accretion disks see e.g., Kato et al. (1998). A general overview of the accretion process can be also found in e.g., Frank et al. (2002).

2.3.1 Spherical flow onto a stationary accretor

We will begin with a review of the classical derivation of the mass accretion rate for the hydrodynamic spherical flow onto a stationary accretor. Since this derivation can be found in several other publications (the original paper by Bondi (1952); or in textbooks, e.g., Shapiro & Teukolsky (1983, pp. 412–422)), we will only highlight the aspects most relevant to the numerical simulations presented here.

In the case of the steady-state, spherical flow, the system is completely governed by the continuity equation,

$$\nabla \cdot \rho u = \frac{1}{r^2} \frac{d}{dr} (r^2 \rho u) = 0 , \quad (2.36)$$

and the Euler equation,

$$u \frac{du}{dr} = -\frac{1}{\rho} \frac{dP}{dr} - \frac{GM}{r^2} . \quad (2.37)$$

Assuming the medium to be a polytropic gas, i.e., $p/p_\infty = (\rho/\rho_\infty)^\gamma$, with p_∞ and ρ_∞ , respectively, the pressure and density far away from the accretor and γ the adiabatic index, one can integrate Eq. (2.36) and Eq. (2.37) to obtain a mass accretion rate of

$$\dot{M}_B = 4\pi R_B^2 \rho_\infty c_\infty \lambda . \quad (2.38)$$

In this equation, c denotes the sound speed given by $c^2 \equiv dp/d\rho = \gamma p/\rho$ and the radius of the effective cross-section is the Bondi radius

$$R_B = \frac{GM}{c_\infty^2} , \quad (2.39)$$

where G is the gravitational constant and M the mass of the accretor. The dimensionless parameter λ satisfies the equation

$$f(u) = \lambda^{-2(\gamma-1)/(\gamma+1)} g(x) , \quad (2.40)$$

in which f and g are functions of the dimensionless velocity $u \equiv v/c$ and distance $x \equiv r/R_B$ which have been separated to the left and right of the equals sign,

$$f(u) \equiv u^{-2(\gamma-1)/(\gamma+1)} \left(\frac{u^2}{2} + \frac{1}{\gamma-1} \right) , \quad (2.41)$$

$$g(x) \equiv x^{4(\gamma-1)/(\gamma+1)} \left(\frac{1}{x} + \frac{1}{\gamma-1} \right) . \quad (2.42)$$

The classical derivation now finds the maximum rate of steady state accretion by solving equation ($f(u)=\lambda g(x)$) for λ and using the minimum values for f and g . These minimum values occur at the sonic point ($u_s = 1$) which is at

$$x_s = \frac{5 - 3\gamma}{4} . \quad (2.43)$$

This, however, assumes that the accretor is always smaller than the distance to the sonic point x_s , since the matter passing through this point limits the accretion rate. If this "funnel" lies within the accretor, this limiting factor is shifted further out. Note that the sonic distance x_s decreases linearly from $x_s(\gamma = 1) = 0.5$ down to zero for $\gamma = 5/3$. So, although for most values of γ the sonic point lies outside the usually very small accretor, this is never the case for $\gamma = 5/3$: whatever the small but finite radius of the accretor, it is always larger than $x_s(\gamma = 5/3) = 0$. Our accretor is modelled by a vacuum sphere, so we will assume that the gas expands with sound of speed across the accretor boundary (at distance R). With this assumption we return to equation ($f(u)=\lambda g(x)$) and obtain

$$\begin{aligned} \lambda(R) &= \left[\frac{g(x = R_*)}{f(u = 1)} \right]^{(\gamma+1)/[2(\gamma-1)]} \\ &= \left[\frac{2}{\gamma+1} R_*^{4(\gamma-1)/(\gamma+1)} + \frac{2(\gamma-1)}{\gamma+1} R_*^{(3\gamma-5)/(\gamma+1)} \right]^{(\gamma+1)/[2(\gamma-1)]} , \end{aligned} \quad (2.44)$$

with the limits

$$\lim_{\gamma \rightarrow 5/3} \lambda = \left(\frac{3}{4} R_* + \frac{1}{2} \right)^2 , \quad (2.45)$$

$$\lim_{R \rightarrow \infty} \lambda = \left(\frac{2}{\gamma+1} \right)^{(\gamma+1)/[2(\gamma-1)]} R_*^2 \xrightarrow{\gamma \rightarrow 5/3} \frac{9}{16} R_*^2 , \quad (2.46)$$

$$\lim_{\gamma \rightarrow 1} \lambda = R_*^2 \exp \left(\frac{1}{R_*} - \frac{1}{2} \right) \xrightarrow{R_* \rightarrow \infty} \frac{1}{\sqrt{e}} R_*^2 \exp . \quad (2.47)$$

The limit $\lambda(R_* \rightarrow (5 - 3\gamma)/4)$ gives the classical value, which can be found in Bondi (1952) and in textbooks for λ .

The curves in Fig. 2.5 show the run of the mass accretion rate \dot{M}_B from Eq. (2.38), with the values of λ taken from Eq. (2.44). The straight lines joining the minima of the curves to the y -axis are the connection to the classical Bondi derivation: when the radius R_* of the accretor is smaller than the sonic point distance x_s , one must take this minimum value for λ . Hence the accretion rate stays at the minimum value for R_* smaller than x_s , producing a straight line to the left of the minimum. When R_* is larger than x_s , one should take the increased mass accretion rate as given by Eq. (2.38) and Eq. (2.44).

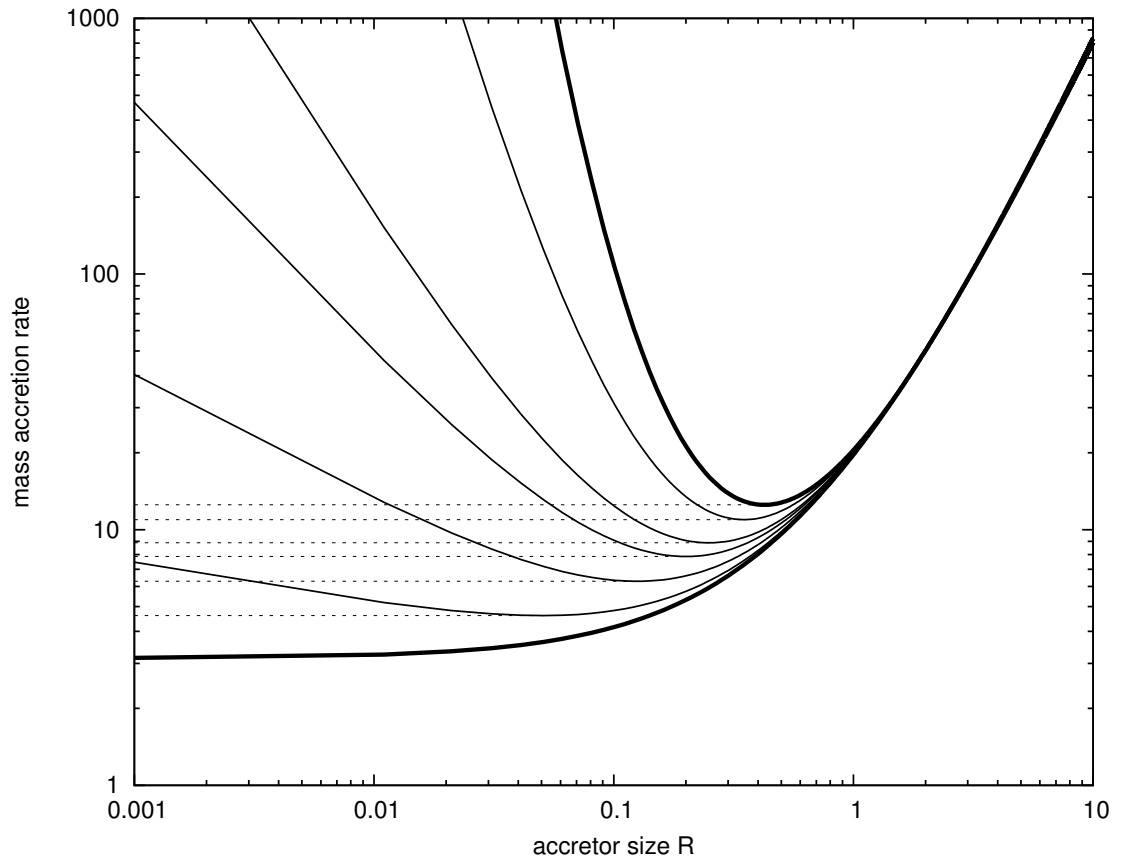


Figure 2.5: Mass accretion rate for a stationary accretor as given by Eq. (2.38) and Eq. (2.44) as a function of accretor size R_* and specific heat ratio $\gamma = 5/3, 1.6, 1.5, 1.4, 4/3, 1.2$ and 1.1 . The two limiting cases for γ ($\gamma = 5/3$ and $\gamma = 1.1$) are shown in bold solid lines.

Ruffert (1994) suggested an interpolation formula that approximates the run and dependencies of the numerically obtained accretion rates by modifying the equations known and applicable to limiting cases (e.g. stationary accretor, large Mach number, etc.). He introduced the following formulae to fit the mass accretion rates over many orders of magnitude:

$$\dot{M} = \sqrt{\dot{M}_C \left(\dot{M}_C + \frac{u_\infty}{\alpha c_\infty} \dot{M}_V \right)} \quad (2.48)$$

where

$$\alpha = 4 \left(\frac{2}{\gamma + 1} \right)^{(\gamma+1)/(2(\gamma-1))}, \quad (2.49)$$

$$u_\infty = \sqrt{\max(v_\infty^2 - c_\infty^2, 0)} \quad (2.50)$$

and accretion rates \dot{M}_C and \dot{M}_V

$$\dot{M}_C = \lambda 4\pi \bar{R}_B^2 c_\infty \rho_\infty \max\left(\frac{R_*}{\bar{R}_B}, \frac{5-3\gamma}{4}\right), \quad \text{for } v_\infty \ll c_\infty, \quad (2.51)$$

$$\dot{M}_V = \pi \bar{R}_A^2 v_\infty \rho_\infty \max\left(\frac{R_*}{\bar{R}_A} \left(\frac{R_*}{\bar{R}_A} + 1\right), 1\right), \quad \text{for } v_\infty \gg c_\infty; \quad (2.52)$$

where

$$\bar{R}_B = \frac{GM}{\max(v_\infty^2, c_\infty^2)} \quad \text{and} \quad \bar{R}_A = 2\gamma \bar{R}_B; \quad (2.53)$$

represent an approximation of both limiting cases: the case in which motion of the accretor v_∞ relative to the medium is slow (compared to the sound speed), and the case in which the accretor move fast through the medium. The latter Eq. (2.52) is the Hoyle-Lyttleton rate (Hoyle & Lyttleton 1940) combined with the rate for simple geometric accretion: one takes whichever is larger.

The run of \dot{M} has been included in Fig. 2.6

2.3.2 Bondi-Hoyle-Lyttleton accretion

This Section contains a brief summary of the work of Bondi, Hoyle and Lyttleton, who first considered accretion by a star moving at a steady speed through an infinite gas cloud. This type of accretion bears their name and we will refer to it as BHL accretion. The classical derivation of the mass accretion rate for a moving accretor can be found in the original work by Bondi & Hoyle (1944) or in one of the more recent reviews – c.f., e.g., Edgar (2004).

We will follow Hoyle & Lyttleton (1939) who considered a point of mass moving supersonically through gas which is free of self-gravity, and is uniform in infinity. The gravity of the star focuses the flow into a dense tail which is then partially accreted. Let us consider a streamline with impact parameter b . If this streamline follows a ballistic trajectory (in the case that pressure effects are negligible), we can apply the conventional orbit theory where the equations of motion in the polar coordinates are given by

$$\ddot{r} - r\dot{\varphi}^2 = -\frac{GM}{r^2}, \quad (2.54)$$

$$r^2\dot{\varphi} = bv_\infty. \quad (2.55)$$

Note that the second equation expresses the conservation of angular momentum where $l = L/m = bv_\infty$ is the specific angular momentum. By substituting $u = r^{-1}$, we may rewrite the first equation as

$$\frac{d^2u}{d\varphi^2} + u = \frac{GM}{l^2}. \quad (2.56)$$

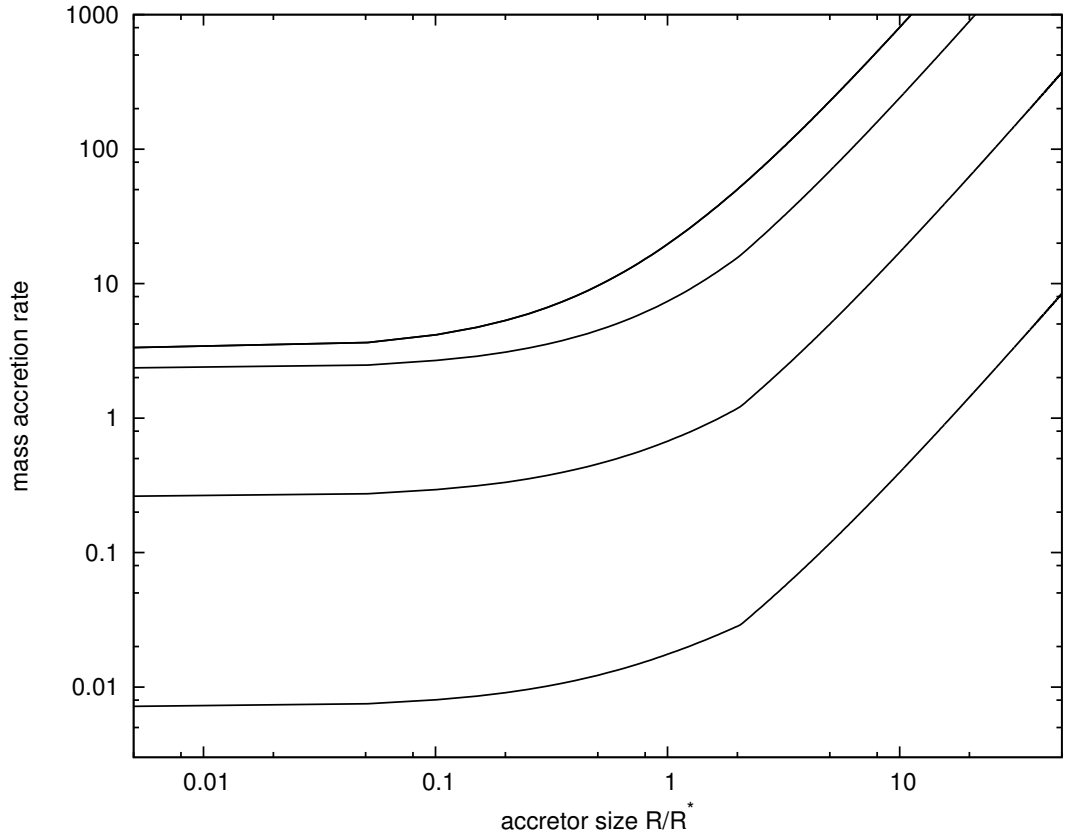


Figure 2.6: Mass accretion rates in units $R_B^2 c_\infty \rho_\infty$ as a function of accretor size. The Mach number is an additional parameter. The top most curve corresponds to Mach number 0.6. The other lines belong to Mach number 1.4, 3.0 and 10.

The general solution of this equation has a form of $u = A \cos \varphi + B \sin \varphi + C$ for three arbitrary constants A , B and C . Substitution of this general solution immediately shows that $C = GM/l^2$. The values of A and B are determined by the boundary conditions

$$u \rightarrow 0 \quad \text{as} \quad \varphi \rightarrow \pi \quad (2.57)$$

$$\dot{r} = -bv_\infty \frac{du}{d\varphi} \rightarrow -v_\infty \quad \text{as} \quad \varphi \rightarrow \pi \quad (2.58)$$

These conditions are satisfied by

$$u = \frac{GM}{b^2 v_\infty^2} (1 + \cos \varphi) - \frac{1}{b} \sin \varphi . \quad (2.59)$$

The passing material, specified by its impact parameter of interval $(b, b + db)$, encounters $\varphi = 0$ axis at

$$r_0 = \frac{b^2 v_\infty^2}{2GM} , \quad (2.60)$$

and loses a part of its kinetic energy. We assume that, as a result of the collision, the tangential φ -component of velocity is equal to 0. The material is, thus, only

allowed to move in the radial direction with velocity $v_r = v_0 \cos \alpha$ where α is the angle between the tangent to the trajectory of the material and $\varphi = 0$ axis. v_0 is the corresponding velocity magnitude of the material just before the collision. In this case, the energy conservation equation reads

$$\frac{1}{2} (\dot{r}^2 + r^2 \dot{\varphi}^2) - \frac{GM}{r} = \frac{E_0}{m} = \text{const.} , \quad (2.61)$$

where $E_0 = \frac{1}{2} m v_\infty^2$ is the kinetic energy of a particle of the material with mass m at infinity. Then, we can express velocity v_0 as

$$v_0 = \sqrt{v_\infty^2 + \frac{2GM}{r_0}} . \quad (2.62)$$

We can determine α from the ratio of differentials at $\varphi = 0$

$$\tan \alpha = -r_0 \left. \frac{d\varphi}{dr} \right|_{\varphi=0} . \quad (2.63)$$

By differentiating Eq. (2.59) and assuming $\varphi = 0$ and $db = 0$, we find the ratio to be

$$\frac{d\varphi}{dr} = \frac{1}{b} \left(\frac{2GM}{bv_\infty} \right)^2 . \quad (2.64)$$

Therefore, we can write

$$\tan \alpha = \frac{b}{r_0}, \quad \text{a} \quad \cos \alpha = \frac{1}{\sqrt{1 + \left(\frac{b}{r_0}\right)^2}} . \quad (2.65)$$

Making use of Eqs. (2.60), (2.62) and (2.65), we can express the radial component of velocity v_r at $\varphi = 0$ as

$$v_r = v_0 \cos \alpha = \sqrt{\frac{v_\infty^2 + \frac{2GM}{r_0}}{1 + \left(\frac{b}{r_0}\right)^2}} = \sqrt{\frac{v_\infty^2 + \frac{2GM}{r_0}}{1 + \frac{2GM}{r_0 v_\infty^2}}} = v_\infty . \quad (2.66)$$

The usual condition for the material to be accreted onto the star is that v_r is smaller than the escape velocity. Therefore, we have to satisfy

$$\frac{1}{2} v_0^2 \cos^2 \alpha - \frac{GM}{r_0} \leq 0 , \quad (2.67)$$

which, taking into account Eq. (2.66), can be rewritten as

$$v_\infty^2 - \frac{2GM}{r_0} \left(\frac{b}{r_0} \right)^2 \leq 0 . \quad (2.68)$$

The previous equation suggests the existence of a critical point r_* which separates the material that is accreted onto the star and the material that escapes to infinity. Such point has to be at distance

$$r_* = \sqrt[3]{\frac{2GMb^2}{v_\infty^2}} = \frac{2GM}{v_\infty^2} . \quad (2.69)$$

The mass flux arriving in the distance r to $r + dr$ per unit of time is given by

$$\frac{d\dot{M}}{dr_0} = 2\pi b \frac{db}{dr_0} \rho_\infty v_\infty . \quad (2.70)$$

By differentiating Eq. (2.60) we find the ratio of differentials db/dr_0 to be

$$\frac{db}{dr_0} = \frac{GM}{bv_\infty^2} , \quad (2.71)$$

which we can substitute in Eq. (2.70) and rewrite it as

$$\frac{d\dot{M}}{dr_0} = 2\pi\rho_\infty \frac{GM}{v_\infty} . \quad (2.72)$$

This is an interesting result because it does not depend on the impact parameter b . The mass flux per unit of time, therefore, has to be constant along the $\varphi = 0$ axis. By integrating the previous equation along the $\varphi = 0$ axis from 0 to r_* , we obtain the overall accretion rate onto the star

$$\dot{M}_{\text{HL}} = 4\pi\rho_\infty \frac{G^2 M^2}{v_\infty^3} , \quad (2.73)$$

which is known as the Hoyle-Lyttleton accretion rate.

Chapter III

Radiation hydrodynamic model

Numerical simulations of astronomical phenomena play a key role, along with analytic approach and observations. Due to the high spatial and temporal dynamical ranges involved, astrophysical phenomena present a taxing challenge for numerical simulators. To tackle such demanding situations, a number of numerical techniques has been developed that can be broadly split into gridless and grid-based method. The most widely used example of the former is Smoothed Particle Hydrodynamics (Lucy 1977; Gingold & Monaghan 1977, SPH). It has achieved much success, particularly in regimes dominated by gravity. However, its development to include an increasing number of sought-after physical processes is still at a relatively early stage when compared with the effort put into the latter type. The grid-based methods solve the hydrodynamics from first principles, for two and three-dimensional problems mostly in the Eulerian formulation – c.f., e.g., Laney (1998); Toro (1997); Colella & Woodward (1984); Bodenheimer et al. (2006).

We have developed and extensively tested a new hydrodynamic code introduced in Hadrava & Čechura (2012) which is based on the Eulerian hydrodynamics. In this Chapter, we present an enhanced version of the code which we will be later used to investigate the properties and dynamics of the stellar wind in Cygnus X-1.

3.1 Numerical hydrodynamics

We begin this Section by first writing down the complete set of physical equations that are solved by the hydrodynamical code, and then briefly describe the numerical algorithms that we use to solve these equations. This Section is intended to be an overview of the code's properties and capabilities: thus, we gather all of the governing equations into a single place and provide a brief introduction to the numerics of the code. The model utilizes the time-dependent equations of Eulerian hydrodynamics. The relevant equations for mass, momentum, and energy conservation are

$$\frac{\partial \rho}{\partial t} + \nabla \cdot \rho \mathbf{v} = 0, \quad (3.1a)$$

$$\frac{\partial \rho \mathbf{v}}{\partial t} + \nabla \cdot \rho \mathbf{v}^2 + \nabla P = \rho \mathbf{f}, \quad (3.1b)$$

$$\frac{\partial \epsilon}{\partial t} + \nabla \cdot [(\epsilon + P)\mathbf{v}] = 0, \quad (3.1c)$$

respectively where

$$\epsilon = \frac{1}{2} \rho v^2 + \rho e \quad (3.2)$$

is the total energy density, and e is the specific internal energy. In these equations, ρ , \mathbf{v} and P are gas density, peculiar velocity, and thermal pressure, respectively. \mathbf{f} represents net force density of the outer forces acting on a unit volume of gas. We adopt the equation of state of the ideal gas which closes the set of equations

$$P = (\gamma - 1)\rho e. \quad (3.3)$$

Here, γ represent a ratio of specific heats. At this stage of the development of the code, we do not involve magnetic field terms and we work in the purely hydrodynamic limit where magnetic field strength $\mathbf{B} = 0$.

3.1.1 The piecewise parabolic method

A central piece of the numerical integration scheme used in our code is based the piecewise parabolic method (PPM), originally suggested by Colella & Woodward (1984) which have been modified for implementation in astrophysics. In this Section, we will provide a short description of the method. PPM is a higher-order-accurate version of Godunov's method for ideal gas dynamics with spatially third-order-accurate piecewise parabolic monotonic interpolation and a non-linear Riemann solver for shock capturing. The method is based on a second-order spatial interpolation of variables inside individual computational cells. It does an excellent job capturing strong shocks across a few cells. The introduction of parabola as the main interpolation function in a computational cell allows for a more accurate representation of smooth spatial gradients, as well as a steeper representation of captured discontinuities. Generally, the scheme is third-order accurate in space and second-order accurate in time. In the case of equally spaced zones its spatial accuracy increases to fourth-order.

This method advances the hydrodynamic equations in the following steps: (i) construct monotonic parabolic interpolation of cell average data, for each fluid quantity; (ii) compute interface states by averaging the parabola over the domain of dependence for each interface; (iii) use interface data to solve the Riemann problem; (iv) difference the interface fluxes to update the cell average quantities.

Multidimensional schemes are built up by directional splitting, and produce a method that is formally second-order-accurate in space and time and explicitly conserves energy, momentum and mass flux. Both the conservation laws and Riemann

solver are modified to include gravity. Because we are interested in phenomena, generally, with no special geometry, we have adopted Cartesian coordinates. We can dimensionally split the equations and rewrite the one-dimensional versions of Eqs. (3.1) without expansion terms in conservative form as

$$\frac{\partial \rho}{\partial t} + \frac{\partial \rho v}{\partial x} = 0, \quad (3.4a)$$

$$\frac{\partial \rho v}{\partial t} + \frac{\partial \rho v^2}{\partial x} + \frac{\partial P}{\partial x} = \rho f, \quad (3.4b)$$

$$\frac{\partial \epsilon}{\partial t} + \frac{\partial \epsilon v}{\partial x} = \rho v f, \quad (3.4c)$$

Here x and v refer to the one-dimensional co-moving position and peculiar velocity, and f is the acceleration at the cell center. These equations are now in a form that can be solved by the split PPM scheme. We now restrict ourselves to the solution of Eqs. (3.4) in one-dimension. In the Eulerian version of PPM, this is accomplished by a three-step process. First, we compute effective left and right states at each grid boundary by constructing a piecewise parabolic description of the original variables (ρ , v and ϵ) and then averaging over the regions corresponding to the distance each characteristic wave can travel (v , $v - c_s$ and $v + c_s$, where c_s is the sound speed). Second, a Riemann problem is solved using these effective left and right states, and finally the fluxes are computed based on the solution to this Riemann problem and the conserved quantities are updated. This is described in detail in (Colella & Woodward 1984), but we will briefly outline the procedure here both for completeness and to highlight the changes we make in context.

The Eulerian difference equations are

$$\begin{aligned} \rho_j^{n+1} &= \rho_j^n \\ &+ \Delta t \left(\frac{\bar{\rho}_{j+1/2} \bar{v}_{j+1/2} - \bar{\rho}_{j-1/2} \bar{v}_{j-1/2}}{\Delta x_j} \right), \end{aligned} \quad (3.5a)$$

$$\begin{aligned} \rho_j^{n+1} v_j^{n+1} &= \rho_j^n v_j^n \\ &+ \Delta t \left(\frac{\bar{\rho}_{j+1/2} \bar{v}_{j+1/2}^2 - \bar{\rho}_{j-1/2} \bar{v}_{j-1/2}^2 + \bar{P}_{j+1/2} - \bar{P}_{j-1/2}}{\Delta x_j} \right) \\ &+ \frac{\Delta t}{2} f_j^{n+1/2} (\rho_j^n + \rho_j^{n+1}), \end{aligned} \quad (3.5b)$$

$$\begin{aligned} \rho_j^{n+1} \epsilon_j^{n+1} &= \rho_j^n \epsilon_j^n \\ &+ \Delta t \left(\frac{\bar{\rho}_{j+1/2} \bar{v}_{j+1/2} \bar{\epsilon}_{j+1/2} - \bar{\rho}_{j-1/2} \bar{v}_{j-1/2} \bar{\epsilon}_{j-1/2} + \bar{v}_{j+1/2} \bar{P}_{j+1/2} - \bar{P}_{j-1/2} \bar{P}_{j-1/2}}{\Delta x_j} \right) \\ &+ \frac{\Delta t}{2} f_j^{n+1/2} (\rho_j^n v_j^n + \rho_j^{n+1} v_j^{n+1}), \end{aligned} \quad (3.5c)$$

We have used subscripts to indicate zone-centred (j) and face-centred ($j + 1/2$) quantities, while superscripts (n) refer to particular time step. The cell width is Δx_j . Although they have been discretized in space, the accuracy of the updates depend on how well we can compute the fluxes in and out of the cell during Δt . This depends on our ability to compute the time-averaged values of P , ρ , and v at

the cell interfaces, denoted here by $\bar{P}_{j\pm 1/2}$, $\bar{\rho}_{j\pm 1/2}$, and $\bar{v}_{j\pm 1/2}$. We now describe the steps required to compute these quantities. We first construct monotonic piecewise parabolic (third-order) interpolations in one dimension for each of P , ρ , and v . The pressure is determined from Eq. (3.3), the equation of state. The interpolation formula for some quantity q is given by

$$q_j(x) = q_{L,j} + \tilde{x} (\Delta q_j + q_{6,j}(1 - \tilde{x})) \quad \text{for} \quad \tilde{x} \equiv \frac{x - x_{j-1/2}}{\Delta x_j}, \quad (3.6)$$

where we assume $x_{j-1/2} \leq x \leq x_{j+1/2}$. This is Eq. (1.4) of (Colella & Woodward 1984) (in the spatial rather than mass coordinate, as is appropriate for the direct Eulerian approach). The quantities $q_{L,j}$, Δq_j , and $q_{6,j}$ can be viewed simply as interpolation constants; however, they also have more intuitive meanings. For example, $q_{L,j}$ is the value of q at the left edge of zone j , while Δq_j and $q_{6,j}$ are analogous to the slope and first-order correction to the slope of q

$$\Delta q_j \equiv q_{R,j} - q_{L,j} \quad \text{and} \quad q_{6,j} \equiv 6 \left[q_j - \frac{1}{2} (q_{L,j} + q_{R,j}) \right]. \quad (3.7)$$

We have reduced the problem to finding $q_{L,j}$ and $q_{R,j}$. While this is simple in principle, it is somewhat complicated by the requirement that these values should be of sufficient accuracy and that the resulting distribution be monotonic. That means, no new maxima or minima are introduced. The resulting formulae are straightforward but complicated and we will only refer to Eqs. (1.7)–(1.10) of (Colella & Woodward 1984) where the detailed derivation can be found. We also allow steepening as described in that reference.

Once we have reconstructed them, the primary quantities P , ρ , v , and ϵ are averaged over the domains corresponding to the three characteristics $v - c_s$, v , and $v + c_s$, (where c_s is the sound speed in a cell). The linearised gas dynamics equations are then used to compute second-order accurate left and right states that take into account the multiple wave families. This process is described in (Colella & Woodward 1984) and we use their Eqs. (3.6) and (3.7).

With these effective states, an approximation to the Riemann problem is found (see below for more detail about the Riemann solver used), producing estimates for $\bar{P}_{j\pm 1/2}$, $\bar{\rho}_{j\pm 1/2}$, and $\bar{v}_{j\pm 1/2}$ that are third-order accurate in space and second-order accurate in time. These values are then used to solve the difference Eqs. (3.5) for ρ^{n+1} , v^{n+1} , and ϵ^{n+1} .

We include an optional diffusive flux (and flattening for the parabolic curves) that can improve the solution in some cases. Our implementation follows that in the appendix of (Colella & Woodward 1984). In addition, as discussed earlier, the three-dimensional scheme is achieved by operator-splitting and repeating the above procedure in the other two orthogonal directions. The transverse velocities and any additional passive quantities are naturally and easily added to this system (see Eq. (3.6) of (Colella & Woodward 1984)).

3.1.2 Riemann solver

In this Section, we describe the methods we adopt to solve the Riemann problem, which is generally required to compute the fluxes in any Godunov-based scheme. The Riemann problem, we are solving, involves two constant states separated by a single discontinuity at $t = 0$. The subsequent evolution has an exact analytic solution. This solution is described in detail in many texts on computational fluid dynamics – e.g., (Toro 1997). In brief, there are three waves that propagate away from the initial discontinuity. The central wave, characterized by a density jump but not a pressure jump, is called the contact discontinuity. The waves travelling to the left and right of the contact discontinuity can be either shocks, if characteristics converge on the wave front, or rarefaction fans if characteristics diverge. While there is an exact solution to this problem, finding it is expensive. There are four possible combination of left- and right-travelling shocks and rarefactions, only one of which is fully consistent with the initial conditions. Once the correct physical state is determined, the pressure in the central region can only be computed by finding the root to an algebraic equation, which is necessarily an iterative process.

The Riemann solver we use is two-shock (Toro 1997) which works well with the PPM method. The only approximation that two-shock makes is that both left- and right-moving waves are shocks. This solution still requires an iterative method for finding the pressure in between the two waves. On rare occasions, high-order solutions can cause negative densities or energies. For that reason our PPM solver employs a Riemann solver correction mechanism (Lemaster & Stone 2009). If a negative density is found at a particular interface, correction is used to compute the fluxes associated with that cell, and the flux update is repeated.

3.1.3 Boundary conditions

In order to solve the hydrodynamic equations in a certain domain, it is necessary to specify the boundary conditions of that domain. There are two cases. The first is that the boundary is external to the computational domain. The second possibility is that the boundary is within the computational domain. In the first case, we allow for four types of boundary conditions (for simplicity, represented here as being at $x = 0$, with positive x interior and negative x exterior to the domain):

We handle the boundary conditions with use of the ghost zones located at the edges of the active grid. In general, boundary conditions can be of two main types. In the *Dirichlet* condition, the value of a function (which could be 0) is prescribed on the boundary. In the *Neumann* condition, the derivative of the function normal to the boundary surface is prescribed. Commonly used combination of these conditions are show on the two-dimensional grid example. :

- *Reflecting boundary condition.* In this case, the boundary behaves like a mirror, with the solution on the boundary reflecting the solution in the computational domain. The cell-centred variable ρ , e in the ghost cells are set to the corresponding value in the last active cell, thus $\rho_{i+1,j} = \rho_{i,j}$ and $\rho_{i+2,j} = \rho_{i-1,j}$ with an analogous treatment at the j -boundary. The same treatment is given

to the parallel component v^{\parallel} of the velocity. The normal component of the velocity $v_{i+1,j}^{\perp}$ is set to zero, and $v_{i,j}^{\perp}$, and similarly, at the j -boundary.

- *Outflow boundary condition.* Here, all of the variables in the ghost cells, ρ , e , v^{\parallel} , and v^{\perp} , are set to corresponding values in the active cells. This is a Neumann boundary condition with derivatives of all variables set to 0 at the boundary of the active zone. Thus, at the outer i -boundary, $\rho_{i+1,j} = \rho_{i,j}$, $e_{i+1,j} = e_{i,j}$, $v_{i+1,j}^{\parallel} = v_{i,j}^{\parallel}$, and $v_{i+1,j}^{\perp} = v_{i,j}^{\perp}$. An analogous treatment holds at the j -boundary. If the outflow is subsonic, then reflected waves can be generated at the boundary causing numerical problems. If the outflow is supersonic, this problem does not arise.
- *Inflow boundary condition.* Here, all of the variables in the ghost cells, ρ , e , v^{\parallel} , and v^{\perp} , are set to prescribed values, which may vary in time. The component of the velocity normal to the boundary condition must be directed towards the interior of the active zone.
- *Periodic boundary condition* The material that flows out of the grid on one side is assumed to re-enter the grid on the opposite side with the same physical characteristics. Thus, $\rho_{-2,j} = \rho_{i-1,j}$, $\rho_{-1,j} = \rho_{i,j}$, $\rho_{i+1,j} = \rho_{0,j}$, and $\rho_{i+2,j} = \rho_{1,j}$. The same treatment applies to the internal energy and the tangential component of the velocity. For the normal component of the velocity, for i -direction, $v_{-1,j}^{\perp} = v_{i-1,j}^{\perp}$ and $v_{i+2,j}^{\perp} = v_{1,j}^{\perp}$. At the boundaries themselves, the value of v^{\perp} is computed from the difference equations.

3.1.4 Time-stepping

In each integration step we compute a time-step Δt which satisfies the Courant-Friedrichs-Lewy condition

$$\Delta t = C_0 \min \left(\frac{1}{a} \min(\Delta x, \Delta y, \Delta z), \frac{\Delta x}{|v_x|}, \frac{\Delta y}{|v_y|}, \frac{\Delta z}{|v_z|} \right), \quad (3.8)$$

where Δx , Δy , and Δz are the distances between the neighbouring grid nodes in the x , y , and z -direction, respectively. In this case, we take the Courant number C_0 equals to 0.5. In each time-step, all physical variables evolve in accordance with the conservation equations. The employed numerical technique is based on an explicit, Eulerian version of the piecewise parabolic method developed by Colella & Woodward (1984).

3.1.5 Sink particles

Simulations of gaseous collapse and accretion are ubiquitous tools in astrophysics, and all of them face a common difficulty: gravitational collapse forms structures very small compared to the initial object. This enormous dynamic range generally makes the full problem computationally infeasible. Dynamic range is expensive because one requires sufficient resolution in both space and time. to resolve the

largest and smallest scales present in the problem. In practice, this limits three-dimensional Eulerian codes with no mesh adaptivity to dynamic ranges in length no greater than $\sim 10^3$. Lagrangian approaches, such as SPH, and adaptive Eulerian approaches, such as AMR, fare significantly better by concentrating resolution in regions of interest and evolving different regions with different time-steps.

Even with adaptive algorithms, however, many interesting problems require more dynamical range than any code can handle. Therefore a new concept of sinks has been introduced. Sinks are regions of a flow that accrete incoming material but that have no internal structure. Sinks provide a way to stop following collapse at a pre-chosen scale without damaging the rest of the calculation.

Krumholz et al. (2004) introduced a technique to embed an accreting Lagrangian sink particle in an Eulerian code. This technique allows to use Eulerian codes for cases where they are preferred, while retaining the flexibility of a moving sink.

Sink particle creation

Many conditions have been introduced in the process of creating new sink particles. Underlying assumption is that we want to introduce a sink particle only when there is good physical reason to believe that continued collapse is likely. These conditions are necessary since we want to prevent creating spurious sink particles in regions that are not undergoing free-fall collapse.

Density threshold

Among these conditions are (1) density threshold, where a new sink particle is introduced following collapse calculation for many dynamical times without compromising the Truelove criterion for the gas density (Truelove et al. 1997) The Truelove criterion states that in order to avoid spurious fragmentation in numerical collapse calculations in grid codes, the Jeans length,

$$\lambda_J = \left(\frac{\pi c_s^2}{G\rho} \right), \quad (3.9)$$

must be resolved with at least four grid cells, hence $\lambda_J/\Delta x \geq 4$. It should be emphasized that this resolution criterion is only meaningful in regions that are undergoing self-gravitational collapse.

Refinement check

The Jeans refinement criterion discussed in the previous Subsection is also used to resolve the Jeans length of the gas up to the highest level of the AMR grid hierarchy. Only when the Jeans refinement reaches the highest level AMR level, sink particles are allowed to form.

Converging flow check

In order to guarantee that the gas supposed to form a sink particle is in free-fall collapse, the flow must converge toward the center of the designated region, $\nabla \cdot$

$v < 0$. Additionally, we implemented this criterion such that not just the total divergence toward the central cell must be negative, but also that the flows along each principal axes must be directed toward the center. The converging flow check alone is insufficient, because $\nabla \cdot v < 0$ can also be fulfilled by a localized collision of multiple shocks that does not necessarily produce a gravitationally bound structure.

Gravitational potential minimum check

A sink particle can only be created if the central cell of the designated accretion region is the minimum of the local gravitational potential ϕ . The central cell $(i, j, k) = (0, 0, 0)$ must fulfil the constrain

$$\phi(0, 0, 0) = \min_{ijk} [\phi(i, j, k)] \quad (3.10)$$

for the sink particle creation.

Jeans instability check

If the converging flow check and potential minimum criterion are fulfilled, the control volume is checked for Jeans-instability. The thermal energy E_{th} and gravitational energy E_{grav} of the gas are calculated as follows:

$$E_{\text{th}} = \frac{1}{2} \sum_{ijk} M(i, j, k) c_s^2(i, j, k) \quad (3.11)$$

$$E_{\text{grav}} = \frac{1}{2} \sum_{ijk} M(i, j, k) \phi(i, j, k) , \quad (3.12)$$

where $c_s(i, j, k)$ is the sound speed and

$$M(i, j, k) = \rho(i, j, k) \Delta V(i, j, k) \quad (3.13)$$

is the mass inside each cell (i, j, k) . The relation

$$|E_{\text{grav}}| > 2E_{\text{th}} \quad (3.14)$$

must hold for sink particle to be created, which means that the gas exceeds the Jeans mass within the designated region.

Check for bound state

For successful sink particle creation, the total gas energy inside the designated region must be negative,

$$E_{\text{grav}} + E_{\text{th}} + E_{\text{kin}} < 0 . \quad (3.15)$$

The gravitational and thermal energy are calculated from Eq. (3.11) and Eq. (3.12). The kinetic energy

$$E_{\text{kin}} = \frac{1}{2} \sum_{ijk} M(i, j, k) |\mathbf{v}(i, j, k) - \mathbf{v}_{\text{cm}}|^2 \quad (3.16)$$

is determined from the velocity dispersion of the gas, where the center of mass motion,

$$\mathbf{v}_{\text{cm}} = \frac{\sum_{ijk} M(i, j, k) \mathbf{v}(i, j, k)}{\sum_{ijk} M(i, j, k)} \quad (3.17)$$

is subtracted.

Proximity check

A new sink particle cannot be created within the accretion radius of an already existing sink particle. Gas that exceeds the density threshold within the accretion radius on an existing particle is accreted by that particle, if the gas passes the accretion checks as stated above.

3.1.6 Accretion onto sink particles

In our testing case of the BHL accretion we did not follow any criteria for creating a sink particle because we introduced one in the initial conditions. As soon as a sink particle is created, it can gain further mass by accreting gas from the surrounding cells. The gas in which the sink particle is embedded continues to evolve according to the Euler equations.

The size of the accretor is a free parameter in the simulations we present here. The quantities in the cells representing the interior of the accretor are summed and then set to zero after each time step. These sums yield the values of the accretion rate, linear momentum, angular momentum, and energy. When density and energy within the accretor are reset effectively to zero (in fact, the values of density and specific energy are set to 10^{-7} of the initial value ρ_∞ and ϵ_∞ for numerical reasons), a vacuum (near-zero pressure) is created and maintained within the accretor. Matter flowing to the vicinity of the surface, therefore, expands freely into the vacuum. This procedure allows accretion to proceed at the maximum rate. Setting velocities inside the accretor also helps increase the time-step.

3.1.7 Motion of sink particles

In each time step we update the position of each sink particle based on its current momentum, and we modify its momentum through accretion and through gravity. First we change the momenta of sink particles due to their gravitational interactions with the gas; we compute the force via a Plummer Law (Aarseth 1963). We set the softening length in the Plummer Law to $2\Delta x$. Since the number of particles is generally small, we compute gas-particle forces via a direct sum. Second, we update the positions and momenta of the particles including the effects of particle-particle interactions using a high-order integrator with adaptive time-step control. During this integration, we consider only particle-particle gravitational interactions, which, as with the particle-gas interactions, we compute via a direct sum.

Softening the gravitational potential

The basic problem in computing the gravitational acceleration is that it can yield extremely large values if the distance between sink particles and cell centres or between adjacent sink particles becomes small. If the distance goes to zero, the acceleration becomes infinite. For numerical reasons, we introduce a smoothing parameter ϵ that softens the potential of the sink particles

$$\Phi_{\text{sink}} = \frac{-GM_{\text{sink}}}{\{r^2 + \epsilon^2 \Delta x^2 \exp(-r^2/(\epsilon \Delta x)^2)\}^{1/2}} \quad (3.18)$$

and effectively removes the singularity from the equation. r is the distance from the sink particle to the given cell, ϵ is the softening parameter, and Δx is the width of one cell. The exponential dependency reduces the influence of the softening outside the distance given by the smoothing parameter ϵ .

3.2 Code test problems

Numerical methods are essential for the study of a very wide range of problems in astrophysical fluid dynamics. It is, however, crucial to test new algorithms and evaluate the results before any astrophysical application is made. Such testing is designed not only to uncover simple bugs in the implementation, but also serves to demonstrate the strengths and limitations of a given method on a wide variety of problems. An integral part of the code development process, therefore, need to be not only finding run-time errors during the realization but also to measure fidelity of the method in comparison to other techniques.

Testing of hydrodynamic codes usually employs one of three techniques: comparison of numerical calculations with the results of laboratory experiments, comparison of numerical results with analytic solutions where they exist, and cross comparison of numerical solutions generated by different algorithms. Collections of test problems which include examples of type have been published for both hydrodynamic (cf., e.g., Sod (1978); Woodward & Colella (1984)), and magnetohydrodynamic (MHD) codes (e.g., Stone et al. (1992); Tóth & Odstrčil (1996)). Radiation hydrodynamic codes are still not as commonly used as hydrodynamic or MHD codes in astrophysics, despite their importance to the study of problems ranging from winds from hot stars, accretion disk around compact objects and active galactic nuclei, and strong shocks. Moreover, finding test problems for such codes is difficult due to the challenge of finding analytic solution to the dynamical equations, and the scarce number of published results from other codes with which to compare. There is an obvious lack of published test problems for radiation hydrodynamic codes, compared to the case of hydrodynamic or MHD codes.

In this Section, we present a selection of tests that we have found useful in the development of our code. The two test problems presented here involve most of the computational difficulties encountered in broader set of commonly used testing suites. In general, we find our results in good agreement (and often nearly identical) with the ones presented by other studies.

3.2.1 Mach 3 wind tunnel with a step

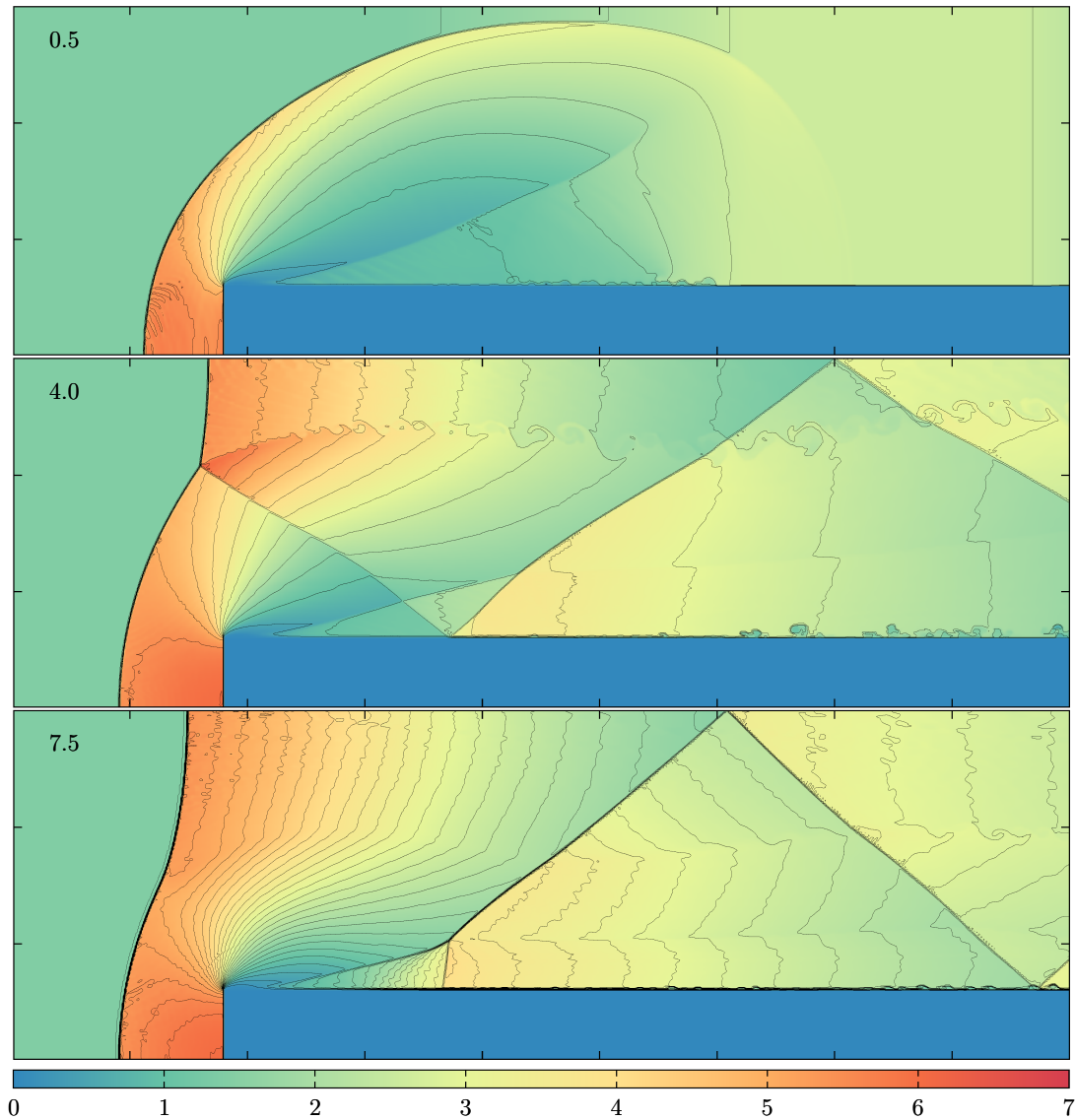


Figure 3.1: The time evolution of the density distribution of the Mach 3 wind tunnel problem. The results were produced with our hydrodynamic code utilizing the PPM scheme. Resolution of this simulation is 900×300 in x and y -direction, respectively. The time index at the top-left corner of each panel shows the progress of the simulation.

This two-dimensional test problem was originally introduced more than fifty years ago by Emery (1968). The problem begins with uniform Mach 3 flow in a wind tunnel containing a step. The wind tunnel is 1 length unit wide and 3 length unit long. The step is 0.2 length unit high and is located 0.6 length unit from the left-hand end of the tunnel. At the left is an inflow boundary condition, and at the right all gradients are assumed to vanish. The exit boundary condition has no effect

on the flow, because the exit velocity is always supersonic. Initially, the wind tunnel is filled with a γ -law gas, with $\gamma = 1.4$ which everywhere has density $\rho = 1.4 \text{ kg m}^{-3}$, pressure $P = 1.0 \text{ Atm}$, and velocity $v = 3 c_s$, where c_s stands for the isothermal sound speed. There are reflecting boundary conditions applied along the walls of the tunnel.

Fig. 3.1 represents a time evolution of the solution produced by our hydrodynamic code. The displayed quantity is the density distribution at 0.5, 4.0 and 7.5 s after the beginning of the simulation. At the topmost panel, we see how the homogeneous inflowing gas, at first, is compressed as it hits the step creating a distinctive shock which spreads towards the upper boundary. 4 seconds after the beginning of the numerical integration (the middle panel), the flow developed a highly complex structure with the shock reflecting from the boundaries and interacting with itself. At this time, the flow is still unstable (a steady solution is reached after approximately 12 seconds) and, therefore, it is suitable for testing the properties of the hydrodynamic code in the presence of shock waves. We notice a development of the Kelvin-Helmholtz instability spreading from the trinity point – intersection of the main strong shock wave and reflected shock which bounced back from the upper boundary. Evolution of such instabilities is amplified by numeric errors generated in the trinity point during the shock waves interaction independently of mesh density. Increasing the dissipation of the numeric scheme near such a shock waves interaction can eliminate this effect. At the bottom-most panel, we show the properties of the flow at 7.5 s after the beginning of the simulation. The rudimentary structure of the flow has been established and, now, we witness slow fading of the reflected shock waves as they propagate towards the right boundary.

In Fig. 3.2 for completeness, we show the remaining quantities of interest as they are calculated 4 s after the beginning of the simulation. The panels in the descending order represent density, velocity magnitude, temperature and pressure of the flow.

The results of this simulation can be directly compared with other broadly used hydrodynamic codes – cf., e.g., Emery (1968); Woodward & Colella (1984). The predictions of our code are generally in good qualitative and quantitative agreement with results obtained with other codes. Fig. 3.3 and 3.4 show an example of the evolution of the same problem calculated by FLASH, a well tested hydrodynamic code often used for astrophysical applications.

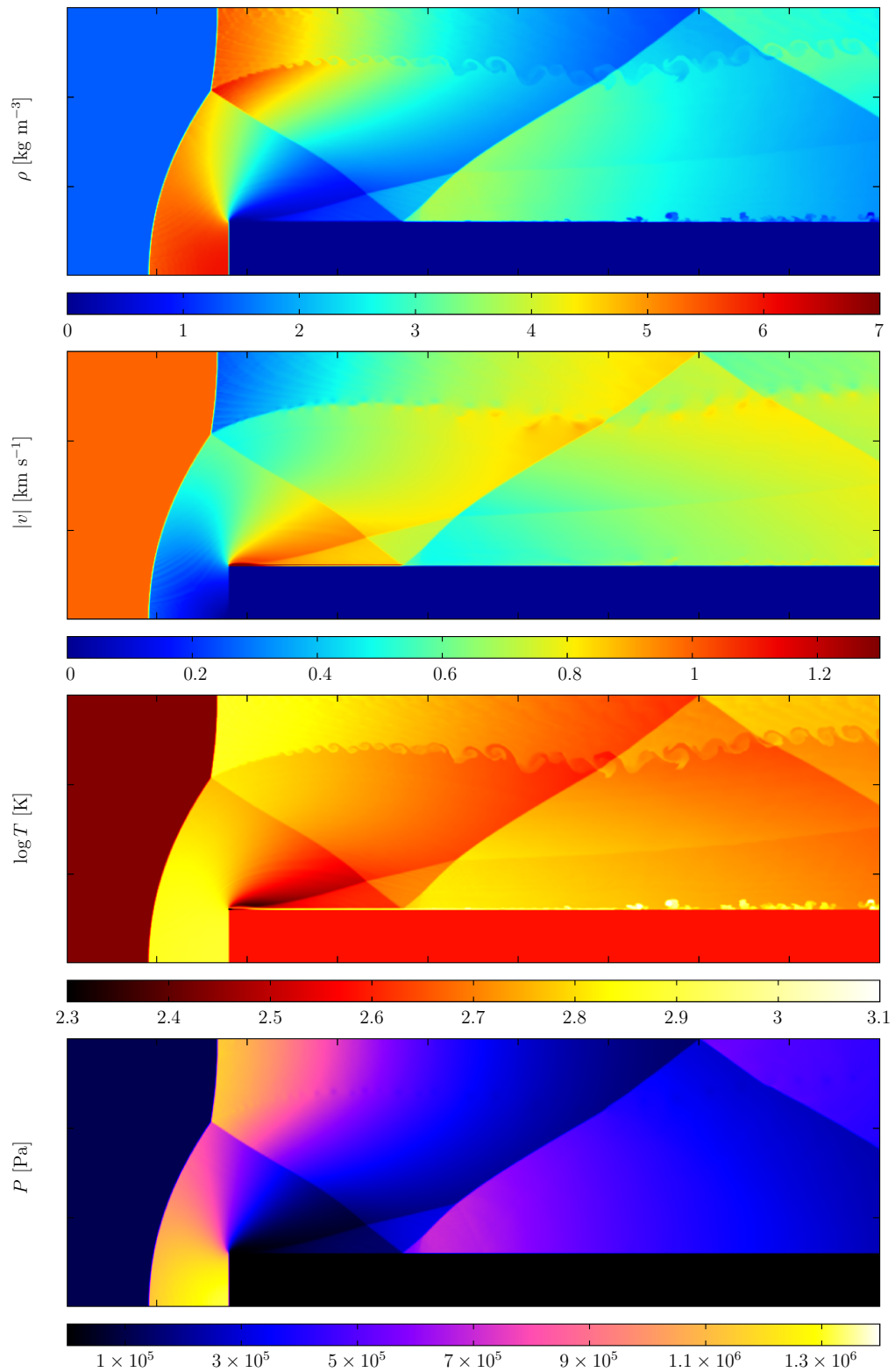


Figure 3.2: The distribution of various quantities for the Mach 3 wind tunnel problem after 4 s since the beginning of the simulation. The displayed quantities in the descending order of panels are density, velocity magnitude, temperature, and pressure.

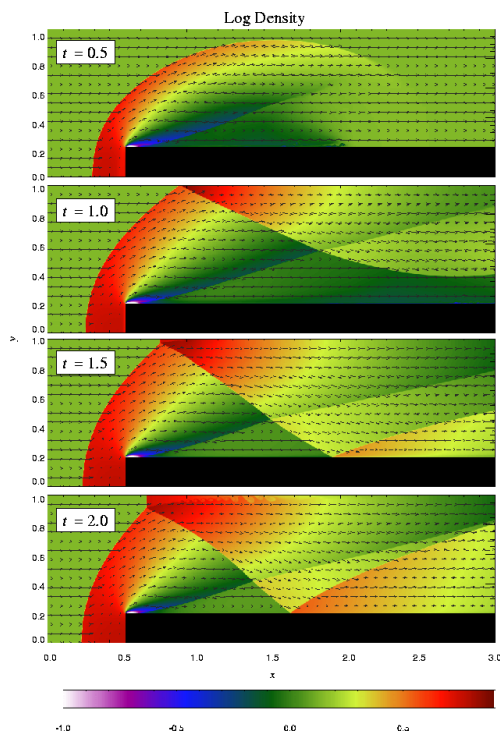


Figure 3.3: The time evolution of the density distribution of the Mach 3 wind tunnel problem as calculated by FLASH code in time interval 0.5–2.0 s from the beginning of the simulations as indicated by the time index at the top-left corner of each panel.

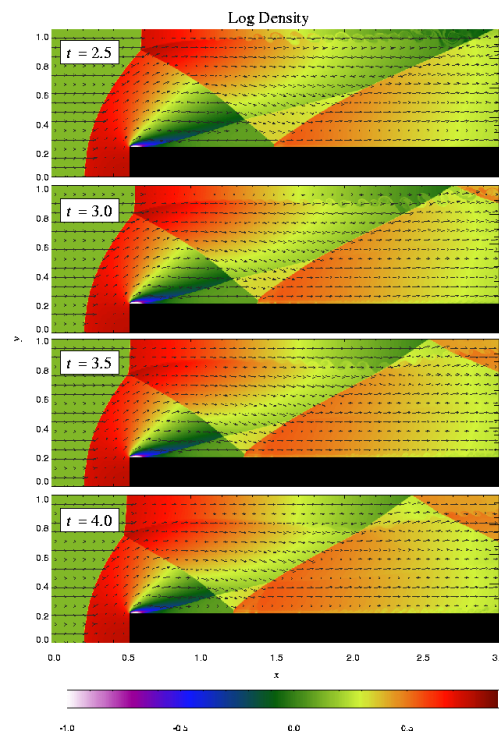


Figure 3.4: The time evolution of the density distribution of the Mach 3 wind tunnel problem as calculated by FLASH code in time interval 2.5–4.0 s from the beginning of the simulations as indicated by the time index at the top-left corner of each panel.

3.2.2 Double Mach reflection of a strong shock

The double Mach reflection test is another classic two-dimensional test of hydrodynamic algorithms originally described by Woodward & Colella (1984) and more recently in Stone et al. (2008). An analytical treatment is found in (Li & Ben-Dor 1995; Ben-Dor 2007) and the references therein. In this problem, a shock is injected at an angle to a reflecting surface (the y^- -boundary). As the shock runs along the reflecting surface, a self-similar shock structure with two triple points evolves. The appearance of this solution is highly sensitive to numerical diffusion. If numerical noise is present, the Kelvin-Helmholtz instability develops and breaks the self-similarity. This problem is design to test the robustness of the numerical algorithms, as well as testing that shocks propagate at the correct speed in all directions (the “carbuncle instability”). The test generates a number of shock waves and discontinuities, some of which should be straight lines, and which are at different angles to the grid axes. If the algorithm has insufficient numerical diffusion the shocks will not stay as straight lines, and in particular there will be problems near the reflection boundary.

The results of simulation of this test problem is shown in Fig. 3.5. The two-dimensional simulation with 1200×300 cells in x and y -direction, respectively, was

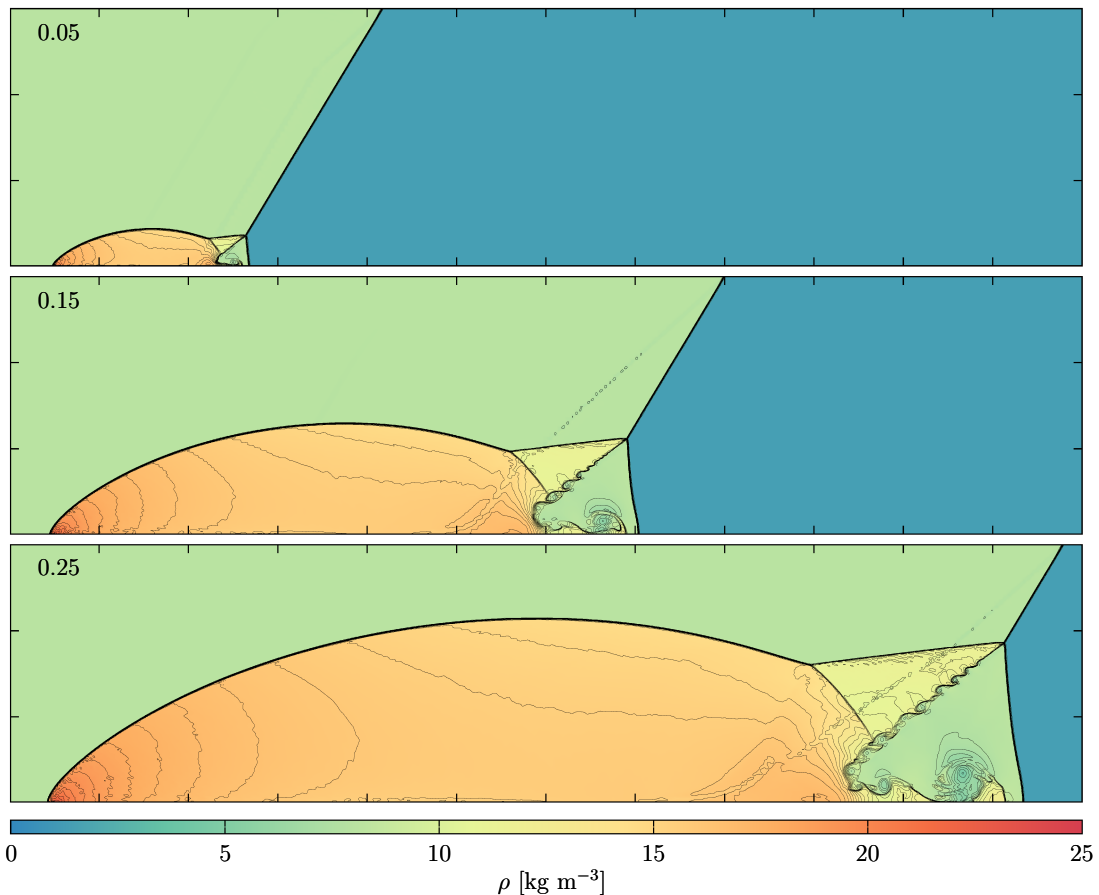


Figure 3.5: The time evolution of the density distribution of the double Mach reflection problem. The results were produced with our hydrodynamic code utilizing the PPM scheme. Resolution of this simulation is 1200×300 in x and y -direction, respectively. The time index at the top-left corner of each panel shows the progress of the simulation. By the end of the simulation, a dense jet is apparent at the leading edge of the shock, propagating along the x -axis. The shape of this jet is sensitive to numerical diffusion, and our result compares favourably to those shown in (Woodward & Colella 1984).

created with a domain of $x = [0, 4]$ and $y = [0, 1]$. We use the equation of state the ideal gas with $\gamma = 1.4$, a pre-shock density of 1.4, and a pre-shock specific internal energy of $2.5/1.4$ (all in arbitrary units). Values of all post-shock quantities satisfy the *Rankin-Hugeniote Conditions*, namely

$$\rho_2 v_2 = \rho_1 v_1 , \quad (3.19a)$$

$$\rho_2 v_2^2 + P_2 = \rho_1 v_1^2 + P_1 , \quad (3.19b)$$

$$v_2 \left(\frac{1}{2} \rho_2 v_2^2 + \rho_2 e_2 P_2 \right) = v_1 \left(\frac{1}{2} \rho_1 v_1^2 + \rho_1 e_1 P_1 \right) , \quad (3.19c)$$

Our test problem involves a Mach 10 shock which is initialized in 60° angle with the reflecting wall, and its initial position at the lower boundary is $x = 1/6$. The short region from $x = 0$ to $x = 1/6$ along the bottom boundary at $y = 0$ is always assigned values for the initial post-shock flow. This boundary condition forces the

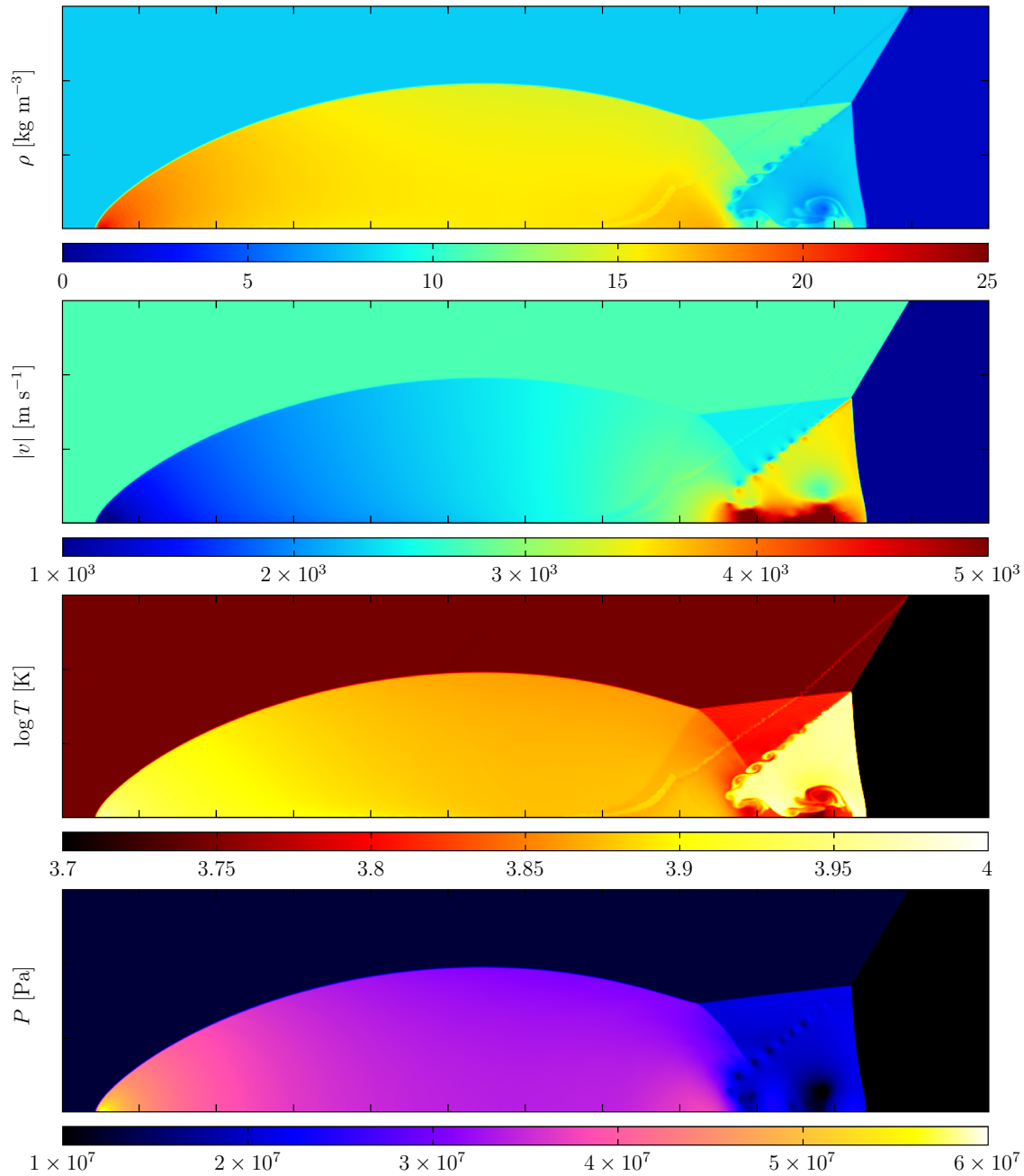


Figure 3.6: The distribution of various quantities for the double Mach reflection problem in time index 0.25 since the beginning of the simulation. The displayed quantities in the descending order of panels are density, velocity magnitude, temperature, and pressure.

reflected shock to be attached to the reflecting wall. The left-hand boundary, at $x = 0$, is also assigned values for the initial post-shock flow, and at the right-hand boundary, at $x = 4$, we adopt the outflow boundary condition where all gradients are set to zero. The values along the top boundary are set to correspond with the exact motion of the initial Mach 10 shock that allows the shock to propagate into



Figure 3.7: The time evolution of the density distribution of the double Mach reflection problem as calculated by Athena code at time index 0.23 s from the beginning of the simulations. Compare with the topmost panel of Fig. 3.6.

the computational domain as if it extends to infinity.

The simulation starts at $t = 0$ and runs until $t = 0.25$ (arbitrary units), at which point the rightmost extent of the shock is at roughly $x = 4$. Fig. 3.5 displays the time evolution of the density distribution as calculated at the time index 0.05, 0.15 and 0.25. The shock propagations through the computational volume with the reflection forming behind it.

Fig. 3.6, we show the remaining quantities of interest as they are calculated at time index 0.23 s after the beginning of the simulation. The panels in the descending order represent density, velocity magnitude, temperature and pressure of the flow. At this point, two Mach wings form with two contact discontinuities. The second contact discontinuity is extremely weak and is more easily noticed by the velocity jump across it rather than the density jump. The second Mach shock is rather weak, and it dies out entirely by the time it reaches the contact discontinuity from the first Mach reflection. This variation of the strength of the second Mach shock is very difficult to compute accurately. At the point where the first contact discontinuity approaches the reflecting boundary the flow of the denser fluid is deflected by a pressure gradient built up in the region. The result is that a jet of the denser fluid is formed and shoots to the right along the boundary. To compute the formation of this jet properly is extremely difficult. A further computational difficulty is presented by the region bounded by the second Mach shock, and the reflecting boundary. In this region, there is very little vertical motion. Therefore, the numerical methods whose dissipation vanishes with zero flow velocity have a tendency to oscillate here.

As in the previous case, we compare our results with computational outcomes of different hydrodynamic code. In Fig. 3.7, we present the same testing problem calculated with Athena, a grid-based code for compressible magnetohydrodynamics. The displayed quantity is density distribution with the color scale ranging from 1.4 to 22.74, thus making Fig. 3.7 directly comparable with the topmost panel of Fig. 3.6.

Chapter IV

Model of HDE 226868/Cygnus X-1

In this Section, we present simulations of our radiation hydrodynamic code which we use to investigate the properties and dynamics of the stellar wind in Cygnus X-1. First, using two-dimensional computational grid, we investigate the role of various physical parameters that influence the interplay between the stellar wind and the compact companion, namely, the mass ratio of the binary components, and parameters of the line-driven wind model. Then, we show the results of three-dimensional simulations, revealing the importance of X-ray photo-ionization. In Sec. 4.1, we give a detailed description of the physical model we use in our simulations and a summary of all physical effects and phenomena involved in the model. A detailed settings of the numerical hydrodynamic code is given in Sec. 4.2. The revised results of anisotropic stellar wind in HMXBs can be found in Sec. 4.3 all together with the description of the grid of simulations computed for specific values of selected physical parameters.

4.1 The physical model of the stellar wind

4.1.1 The m-CAK model & finite-disk correction factor

In CAK formalism, authors adopted the point-like source approximation of a star's radiation field. This assumption is, however, a poor one close to the star's photosphere where the wind is rapidly accelerated. Later improvements to the theory done by Friend & Abbott (1986), and Pauldrach et al. (1986) extended the CAK formalism by adding the effect of an outward centrifugal acceleration to one-dimensional models of the wind outflow in the equatorial plane. Both papers independently derived a modified CAK model (m-CAK) that relaxes the CAK simplifying approximation of point-like star and properly accounts for the finite cone angle subtended by the star. Assuming a uniformly bright spherical source of radiation, they introduced a multiplicative finite-disk correction factor K_{FDCF} (commonly referred to as the FDCF) to the force multiplier $M(t)$. The FDCF is attained by adopting the exact optical depth rather than the radial one,

$$K_{\text{FDCF}}(r, v, dv/dr) = \frac{(1 + \sigma)^{1+\alpha} - (1 + \sigma\mu_*^2)^{1+\alpha}}{\sigma(1 + \alpha)(1 + \sigma)^\alpha(1 - \mu_*^2)}, \quad (4.1)$$

where $\mu_* = \sqrt{1 - (R_*/r)^2}$ for the stellar radius R_* , and σ given by Castor (1974)

$$\sigma = \frac{r}{v} \frac{dv}{dr} - 1. \quad (4.2)$$

4.1.2 Photo-ionization

By its nature, the dynamics of the wind can be strongly influenced by the ionization structure of the medium. The heating and photo-ionization by the X-ray flux depopulate the electron levels available to absorb the momentum of radiation from the primary and decrease the radiative drag on the wind.

Assuming an optically thin gas in local ionization and thermal balance, irradiated by a point-like source of X-rays of a given spectral shape, the ionization structure of the medium is determined solely by the ionization parameter ξ (Tarter et al. 1969) given as

$$\xi = \frac{L_x}{n_n r_x^2}, \quad (4.3)$$

where L_x is the X-ray luminosity of the source, n_n is the nucleon number density of the gas, and r_x is the distance from the X-ray source. While, in reality, optical depth effects are likely to play a role in the wind dynamics in HMXBs, the difficulty of realistically calculating the radiative transfer makes the problem beyond the scope of this work. Therefore, for the purposes of our calculations, the gas will be assumed optically thin.

The preliminary results of our model support the hypothesis that the X-ray ionization tends to slow down the wind material in the immediate vicinity of the compact companion and thus to increase the overall accretion rate (Hatchett & McCray 1977). However, if the zone of full ionization extends to the proximity of the surface of the donor where the wind does not reach the escape velocity yet, the outflow is obstructed right at the base of the wind. Therefore, the X-ray feedback effectively cuts out the accretion process from additional material. The variation of the line force with ξ is very complicated owing to the many different ions responsible. The value of ξ at which the cut-off occurs depends on the nature of process responsible for the acceleration of the wind. For a conservative estimate in the case of typical abundance of the absorbing element relative to hydrogen of 10^{-4} we get the cut-off value of $\log \xi \simeq 2$ for C IV and O VI (Hatchett et al. 1976).

4.1.3 Parameterizing the force multiplier

To capture the flattening of $M(t)$ for small t , we follow Owocki et al. (1988), and modify Eq. (2.35) in such a manner that the force multiplier becomes constant for small t (as it must be in the optically thin limit),

$$M(t, \xi) = k(\xi) t^{-\alpha} \left[\frac{(1 + \tau_{\max})^{1-\alpha} - 1}{\tau_{\max}^{1-\alpha}} \right], \quad (4.4)$$

where $\tau_{\max} = t \eta_{\max}(\xi)$ and η_{\max} is a cutoff to the maximum line strength. Eq. (4.4) now explicitly indicates that M depends on both t and ξ . Consequently, we describe

the influence of ξ to the stellar wind dynamics via the CAK parameters $k(\xi)$ and $\eta(\xi)$. Allowing for ξ -dependence in these quantities captures two systematic changes in $M(t, \xi)$ with ξ : decreasing $\eta_{\max}(\xi)$ with increasing ξ allows the turnover in $M(t)$ to shift to higher t with increasing ξ , while a reduction in $k(\xi)$ at large ξ describes the overall decrease in M for larger ionization parameters.

We follow Stevens & Kallman (1990) in choosing that α does not explicitly depend on ξ . Although, it is possible to allow α to vary, by doing that, we only add unwarranted complexity to the parametrization. We choose value of α that allows us to reproduce the correct observed terminal velocity for a single star of the appropriate spectral type in the standard CAK theory. In their work, Stevens & Kallman (1990) fitted $M(t)$ with two relevant parameters k and η_{\max} as a function of ξ . They found that in the regime of $\log_{10} \xi \leq 2$, the fitting parameters k and η_{\max} can in turn to be fitted with the following exponential functions of ξ only:

$$k = 0.03 + 0.385 \exp(-1.4\xi^{0.6}) , \quad (4.5)$$

and

$$\begin{aligned} \log_{10} \eta_{\max} &= 6.9 \exp(0.16\xi^{0.4}) , & \text{for } \log_{10} \xi \leq 0.5 \\ &= 9.1 \exp(-7.96 \times 10^{-3}\xi) , & \text{for } \log_{10} \xi > 0.5 . \end{aligned} \quad (4.6)$$

Thus, the complicated behaviour of $M(t)$ with ξ can be approximated by an analytic function of ξ . Using the analytic formulae for k and η_{\max} somewhat reduces the accuracy of the representation of $M(t)$, but, for the typical wind model we employ in our simulations, the accuracy of the fits is still within a factor of 2 for the appropriate values of ξ and t .

Taking into account Eqs. (2.31) and (4.4), we finally arrive to an expression for the line force in the framework of the m-CAK model with the inherent dependency on ξ parameter

$$f_{\text{rad}} = \frac{\sigma_e L_*}{4\pi c r^2} k K_{\text{FDCF}} \left(\frac{1}{\sigma_e \rho v_{\text{th}}} \frac{dv}{dr} \right)^\alpha \left[\frac{(1 + \tau_{\max})^{1-\alpha} - 1}{\tau_{\max}^{1-\alpha}} \right] . \quad (4.7)$$

4.1.4 Limb-darkening & gravity-darkening

In the m-CAK model, the calculation of the radiation force is often carried out assuming a uniformly bright finite-sized spherical star. As Cranmer & Owocki (1995); Pelupessy et al. (2000) showed for the case of the rapidly rotating stars, or Hadrava & Čechura (2012) for the tidally distorted surface of the primary, the changes of the shape of the star's surface induce the gravity darkening effect (von Zeipel 1924) as function of latitude or both latitude and longitude, resp. In both cases of a rotating or non-rotating star the decrease of the temperature outwards in the photosphere produces a limb darkening effect which also modifies the finite-disk correction factor. The theoretical formalism for computing a self-consistent radiation force for non-spherical rotating stars, including the effects of stellar oblateness, limb darkening and gravity darkening, was developed by Cranmer & Owocki (1995). However, to

disentangle the effects of each one of these competing processes upon the wind structure, these authors present a semi-quantitative analysis and estimated that the limb darkening effect could increase the mass-loss rate (\dot{M}) in an amount of cca. 11% to 13% over the uniformly bright models. However, that larger mass-loss would imply a reduction in the wind terminal speed.

According to von Zeipel's theorem (von Zeipel 1924), the distribution of the radiative flux F and the effective temperature T_{eff} across the tidally or rotationally distorted surface of a star should be given by the local gravity acceleration g as

$$F \sim T_{\text{eff}}^4 \sim g^{4\beta}, \quad (4.8)$$

where $\beta \equiv 0.25$ in the standard von Zeipel's formula. Because the radiative force f_{rad} given by Eq. (4.7) is proportional to the flux, it enhances the wind more in the polar region of the star where g reaches its highest value, than in the equator and especially in the line joining the component stars where it has its smallest value. For the values of parameters chosen in our calculations, g is higher by 23% at the poles and lower by 15% and 40% in the directions towards the Lagrangian points L_2 and L_1 , respectively, than its value in the perpendicular direction. This effect is thus the opposite of the direct modulation of the wind by the effective potential. In the region, where the distance from the star is comparable to its radius, this effect is additionally enhanced by the ellipticity of the star.

4.1.5 Radiative cooling & X-ray heating

The physical mechanisms which are taken into account include cooling due to free-free and free-bound transitions, the Compton heating via X-ray scattering on electrons, and the inverse Compton cooling in the regions where the temperature of the matter becomes sufficiently large to be able to transfer part of its internal energy to photons. The radiative cooling and X-ray heating are computed under the assumptions of optically thin gas illuminated by an isotropic photon flux with 10 keV bremsstrahlung spectrum (cf. Kallman & McCray (1982) for details of the photo-ionization calculation). We have approximated these rates with an analytic expression as a function of the local gas density, temperature, and ionization parameter – cf. Blondin (1994). The net heating/cooling rate for our approximate formula is given by $(\Gamma_{\text{Com}} + \Gamma_{\text{x}} - \Lambda)$ where

$$\Gamma_{\text{Comp}} = 8.9 \times 10^{-36} \xi (T_{\text{x}} - 4T), \quad (4.9)$$

$$\Gamma_{\text{x}} = 1.5 \times 10^{-21} \xi^{1/4} T^{-1/2} (1 - T/T_{\text{x}}), \quad (4.10)$$

$$\Lambda = 3.3 \times 10^{-27} T^{-1/2} + \quad (4.11)$$

$$[1.7 \times 10^{-18} \exp(-1.3 \times 10^{-5}/T) \xi^{-1} T^{-1/2} + 10^{24}]. \quad (4.12)$$

Here the T_{x} is the characteristic temperature of the bremsstrahlung radiation. The energy sources are calculated in a separate step from the hydrodynamics and are computed under the assumption that the gas is in ionization equilibrium with a constant isotropic X-ray photon flux from the compact companion. The recombination time scale is assumed to be sufficiently fast that the ionization state of the gas

can be given solely by the local density, temperature, and photon flux (Fransson & Fabian 1980). At each point in the wind, the heating rates Γ_x due to X-rays and Γ_{Comp} due to Compton heating, and cooling rate Λ due to locally emitted radiation are calculated as a function of local temperature and ionization parameter ξ . The effects of the primary are accounted for by preventing the wind temperature from dropping below the photospheric temperature of the primary T_{eff} which simulates the UV heating. Although it is likely that the temperature of the wind is slightly lower because of adiabatic cooling, the results of our simulations depend only very weakly on this temperature.

4.2 Numerical settings

The simulations of the radiation-hydrodynamic model of the stellar wind in HMXBs presented in this Section are conducted on either two or three-dimensional Cartesian coordinate grid co-rotating with the modelled components of binary. The model utilizes the time-dependent equations of the Eulerian hydrodynamics. In this case, the continuity equations for mass, momentum, and energy are

$$\frac{\partial \rho}{\partial t} + \nabla \cdot \rho \mathbf{v} = 0, \quad (4.13a)$$

$$\frac{\partial \rho \mathbf{v}}{\partial t} + \nabla \cdot \rho \mathbf{v} \mathbf{v} + \nabla P = \rho \mathbf{f}, \quad (4.13b)$$

$$\frac{\partial \epsilon}{\partial t} + \nabla \cdot [(\epsilon + P)\mathbf{v}] = \left(\frac{\rho}{m_{\text{H}}}\right)^2 (\Gamma_{\text{Com}} + \Gamma_x - \Lambda), \quad (4.13c)$$

– cf. Eqs. (3.1). The model incorporates the physical effects discussed in Sec. 4.1: gravity of the primary and compact component, centrifugal force due to the orbital motion, acceleration of the wind caused by the radiative pressure in continuum (Thomson scattering) and in lines, and the Coriolis force due to the caused by the non-inertial reference frame.

In the case of all three-dimensional simulations, we adopt an equidistantly spaced grid of $207 \times 157 \times 157$ cells in x , y and z -direction, respectively. Similarly, for the two-dimensional case, we use resolution of 407×307 cells in x and y -direction.

4.2.1 Boundary conditions

The grid is initialized with a smooth, steady wind outflow coming from a specific Roche equipotential that represents the surface of the primary. Density is kept uniform across the whole inner boundary condition and constant at the value of ρ_0 . We estimate ρ_0 by assuming the initial mass-loss rate $\dot{M} = 2 \times 10^{-6} M_{\odot} \text{ yr}^{-1}$ and the radial outflow velocity from the surface to be equal to the isothermal speed of sound c_s . The inner boundary condition is specified as inflow. Velocity of the material coming from the inner boundary, thus, always points inside the computationally active area and its tangential component is set to 0. Its magnitude, however, is allowed to vary so the amount of inflowing material is dependent on the conditions in

Table 4.1: Simulation parameters

Parameter	Symbol	Used value
Effective temperature of primary	T_{eff} [K]	30000
Average radius of primary ...	R_* [R_{\odot}]	18
Luminosity of primary	L_* [L_{\odot}]	2.25×10^5
X-ray luminosity		
Low/Hard state	L_{LH} [erg s $^{-1}$]	1.9×10^{37}
High/Soft state	L_{HS} [erg s $^{-1}$]	3.3×10^{37}
Mass of donor	M_* [M_{\odot}]	24
Mass of BH	M_{x} [M_{\odot}]	16
Mass-loss rate	\dot{M} [M_{\odot} yr $^{-1}$]	2×10^{-6}
Orbital period	P_{orb} [days]	5.599829
Binary separation	D [R_{\odot}]	45
Eccentricity	e	0

the computational active area. For the outer boundaries, we adopt outflow boundary condition by setting gradients of all quantities to 0, permitting the matter to flow freely out of the grid. Additionally, at the outer boundary, velocity is prevented from pointing inside the computationally active area.

As a boundary condition for the compact companion, we used the sink particle treatment. A sink particle is a region that accretes incoming material but has no internal structure. It is defined by the accretion radius r_a . Any matter that finds itself within the accretion radius of a sink particle is removed from the computational grid and its mass is added to the mass of the sink particle. If a computational cell lies only partially within the accretion radius, or if the accretion radius is smaller than a cell that a sink particle resides in, then only a proportional amount of matter is accreted onto the sink particle. The position of the sink particle is not arbitrarily fixed within the computational grid but since we neglect the amount of angular and linear momentum that is being transferred from the accreted gas, the sink particle, representing the compact companion, remains stationary for the whole duration of the simulation.

4.3 Results of the stellar wind simulations

The parameters of the following simulations were chosen in accordance with the observed parameters of Cygnus X-1/HD 226868 (see Table 4.1) – a representative of the HMXBs and a well-known black hole candidate. The compact component of the system is a stellar-mass black hole orbiting a massive O9.7Iab supergiant. In the past four decades, many estimates have been made of the masses of both components of the binary – e.g., Caballero-Nieves et al. (2009) inferred wide observational limits stating the mass of $23_{-6}^{+8} M_{\odot}$ and $11_{-3}^{+5} M_{\odot}$ for the primary and the compact component of the system, respectively. However, most of these estimates are unreliable

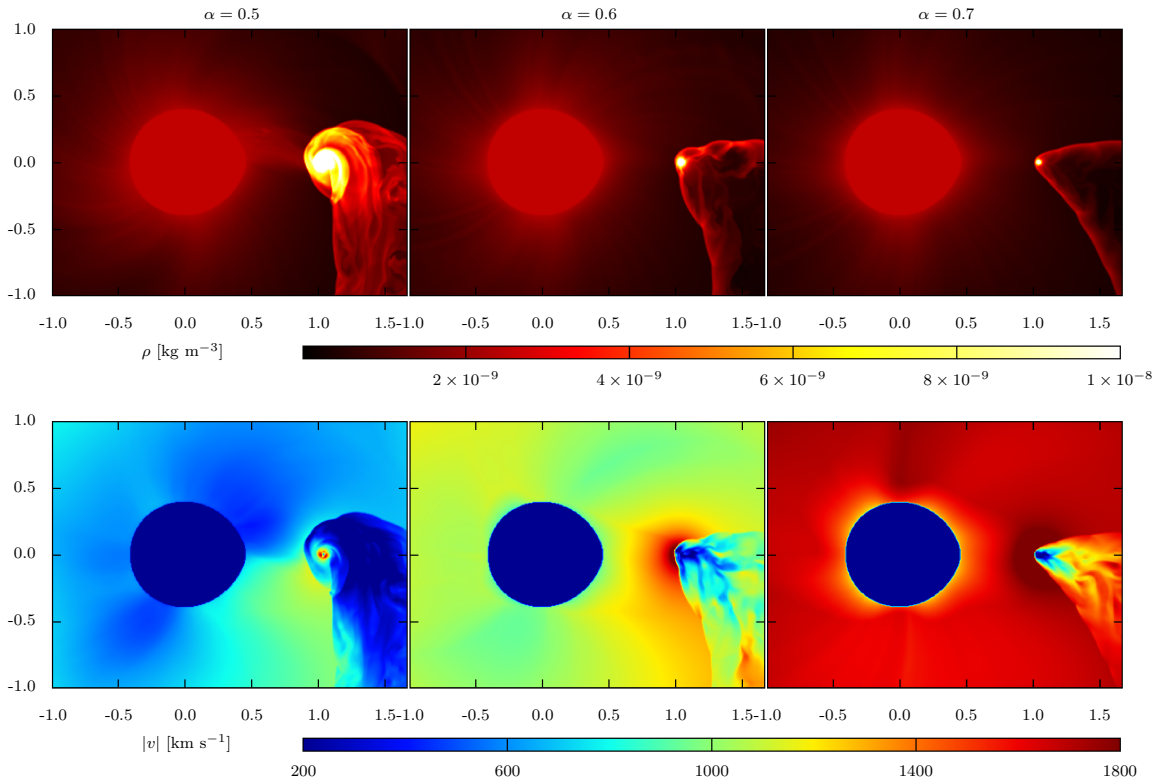


Figure 4.1: Series of three two-dimensional simulations of the stellar wind in the equatorial plane of Cygnus X-1 with increasing value of α parameter. This simulation disregard the effects of the X-ray ionization on the dynamics of the wind. Additionally, k parameter is kept on a constant value 0.25. We can notice a clear trend of shrinking of the gaseous tail, and decreasing the amount of matter captured in the vicinity of the compact companion with the increasing value of α . The three upper-most panels shows a density distribution after solution reached the quasi-stationary state, $\sim P_{\text{orb}}$. The lower panels represent a corresponding velocity magnitude plots.

because they are based on unsatisfactory determination of the distance to Cygnus X-1. In their recent paper, Orosz et al. (2011) were able to strongly constrain some of the principal parameters of the Cygnus X-1. By utilizing an unprecedentedly precise distance from a trigonometric parallax measurement for Cygnus X-1 (Reid et al. 2011), which is $1.86_{-0.11}^{+0.12}$ kpc, they found masses of $M_* = 19.16 \pm 1.90 M_{\odot}$ and $M_x = 14.81 \pm 0.98 M_{\odot}$ for the O-star and black hole, respectively. These estimates are considerably more direct and robust than previous ones, owing largely to the new parallax distance. In a recent paper, however, Ziółkowski (2014) showed that the mass of the supergiant is inconsistent with the evolutionary models for the massive core hydrogen burning stars. Based on the evolutionary models, the mass of the supergiant is, most likely, in the range of 25 to 35 M_{\odot} . The corresponding mass of the black hole is in the range of 13 to 23 M_{\odot} . If, as a result of the rotation induced mixing, the hydrogen content of HD 226868 is equal to about 0.6 (as suggested by

some observational data), then its present mass may be somewhat lower $\sim 24 M_{\odot}$.

For the purpose of our model, we have adopted values of $M_* = 24 M_{\odot}$ and $M_x = 16 M_{\odot}$. The orbital period is 5.6 days and the corresponding orbital separation of the components is $45.4 R_{\odot}$. The critical Roche lobe of this system has a mean radius of $18.9 R_{\odot}$: the Lagrangian point L_1 is at a distance of $24.5 R_{\odot}$, while the intersection of the critical equipotential with the rotational axis of the supergiant is $17.7 R_{\odot}$ from the supergiant centre. We have set the surface of the donor star to a mean radius of $18.5 R_{\odot}$ (i.e. at the equipotential of size $22.3 R_{\odot}$ towards the companion and $17.5 R_{\odot}$ towards the pole). The gravity acceleration g varies across this equipotential from 1.5 to $3.1 \times 10^3 \text{ cm s}^{-2}$ towards the L_1 and the pole, respectively, i.e. the mean value $\log g = 3.3$ is close to the observational limit 3.00 ± 0.25 found by Caballero-Nieves et al. (2009). We assume the primary is tidally locked with the companion and exhibits synchronous rotation.

The interplay between a stellar wind and the gravitational field of a compact object in HMXBs can be complicated by the interaction of several competing processes. In order to isolate and understand the importance of each of the physical effects that influence the gas flow, we present a series of simulations in which only a specific parameter is being changed. In the following Subsections we will show results of restricted simulations we ran in order to discuss the effects of α parameter, mass ratio of the compact companion to the primary, and the X-ray ionization on the over all solution. Considering the number of simulations and their high computational time requirements, we were forced to restrict our model to two-dimensional grid. But here we are only interested in qualitative changes that take place in the gas flow with for varying parameters. The general conclusions we make can be easily extended to the three-dimensional case. Later, we examine the full three-dimensional case that incorporates all of the physics available in our numerical model.

In the two-dimensional simulations, we use an equidistantly spaced grid of 407×307 cells in x and y -direction, respectively. The computational volume has a range of $x = [-1, 1.66] \times D$ and $y = [-1, 1] \times D$, where $D^3 = G(M_* + M_x) P_{\text{orb}}^2 / 4\pi^2 = 3.16 \times 10^{10} \text{ m}$, yielding a spatial resolution of the computational grid $dl = 2.1 \times 10^8 \text{ m}$. The material donating primary star is centred at $[x, y] = [0, 0]$, while the position of the compact companion is $[x, y] = [D, 0]$.

The time-step Δt is adjusted every computational step, satisfying the condition given by Eq. (3.8) and typically reaching value of $\sim 10^{-4} P_{\text{orb}}$.

Most of our simulations were run for the total duration of up to three orbital periods. In all cases, the simulations quickly converge to a quasi-stationary solution, taking less than one orbital period to establish a dynamical balance.

4.3.1 Dependency on α parameter

Our first two-dimensional simulation is of the stellar wind from co-rotating primary in which the only influence of the compact companion on the gas flow is via its gravity. The X-ray luminosity of the source is set to 0 and the value of k parameter is kept constant on 0.25. The parameter α takes progressively higher values of 0.5, 0.6, and 0.7. Other parameters of the simulations are taken from Table 4.1. Because

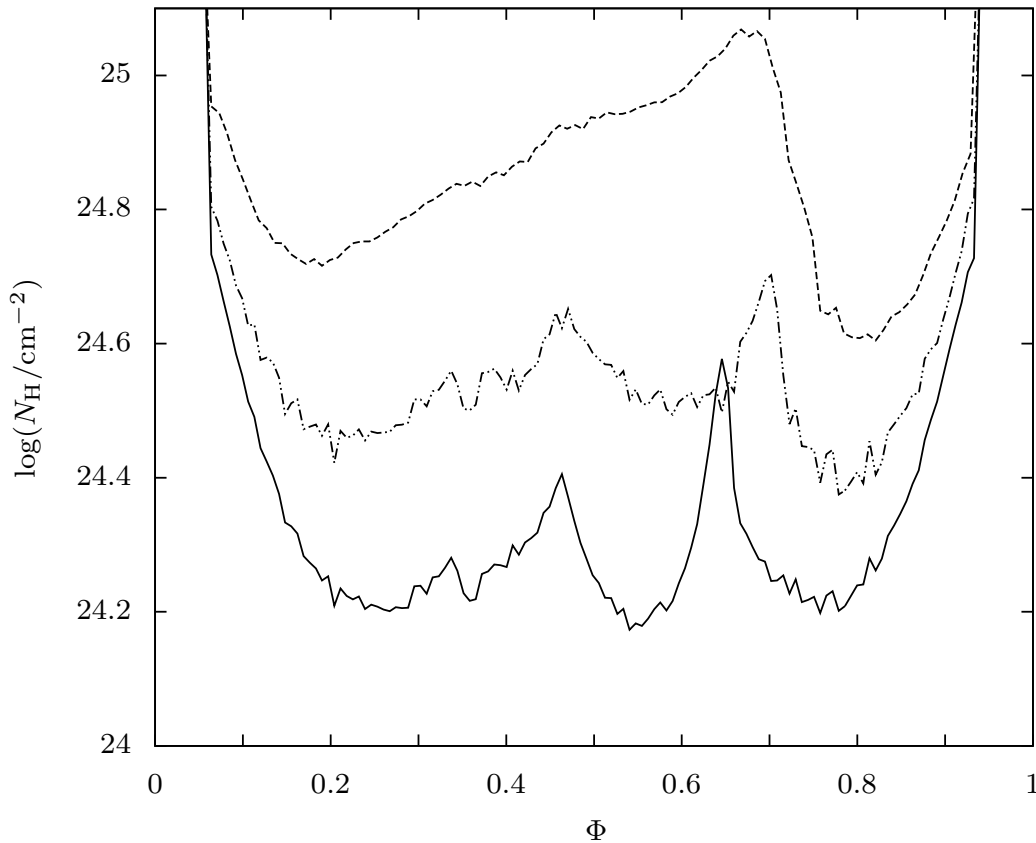


Figure 4.2: Integrated column density for the simulation shown in Fig. 4.1 as a function of orbital phase Φ time-averaged over one orbital period. Each line represents column density profile for different value of α – 0.5 (dashed line), 0.6 (dash-dotted line), and 0.7 (solid line).

of the lack of the effects of the X-ray ionization, this simulation should be closest to the approximation of uniform, axisymmetric accretion - Bondi-Hoyle-Lyttleton accretion (BHL hereafter).

The density distribution and the velocity magnitude of the wind in the orbital plane, after the quasi-stationary solution was reached (typically $\sim 3P_{\text{orb}}$), are displayed in Fig. 4.1. The red and blue disks in the upper and bottom panels, respectively, represent the surface of the supergiant with a pre-set value of density ρ_0 . Small tangential variations in density are caused by imperfection of the inner boundary condition, more specifically, by the fact that we try to capture a round object within the Cartesian coordinate grid. Nonetheless, the variations are small and do not influence the overall picture. We can use them, on the other hand, as streamline markers. By doing so, we reveal spiralling trajectories of the wind out of the system - clearly the effect of the Coriolis force.

For the ideal gas with the adiabatic index $\gamma = 5/3$, capturing of the stellar wind in the vicinity of the compact companion leads to the formation of an accretion disk. The size of the disk is predominantly determined by the amount of material captured within the gravity well of compact companion, which is inversely related

to the velocity magnitude of the wind passing in the close proximity of the compact object. When the supersonic wind meets the obstacle in form of the accretion disk, it creates a standing bow shock extending to a tail-like structure of hot turbulent slowly moving gas. As the bow shock extends downstream, it is affected by the Coriolis force which causes the flow to curve clockwise. However, the shape of the bow shock remains roughly axisymmetric.

We notice that increasing values of α leads to higher velocities of the wind passing near the compact companion. This effect has two consequences. Firstly, the size of the accretion disk shrinks as the amount of material being captured is considerably lowered. The obstacle profile is smaller, therefore, the bow shock is less pronounced. Secondly, the angle of the bow shock "wings" decreases, leaving the shock cone narrower. The higher values of α also cause the gas within the tail to be less turbulent. This is a consequence of several effects that the higher velocity profile has on the gas dynamics. The occasional oscillations seen in the first two columns of Fig. 4.1 are a result of the non-zero angular momentum in the accreting stellar wind with respect to the compact object. The exact axisymmetry of the accretion flow is violated by the orbital velocity of the system, even for a co-rotating companion. Because the wind approaches the compact object at a finite angle with respect to the line of centres. Wind on the trailing side of the compact object (lagging behind in orbit) is closer to the primary and therefore denser than the wind on the leading side due to the $1/r^2$ divergence of the wind. Initially, the asymmetry in the flow leads to a larger ram pressure on the high-density side that drives the bow shock off towards the low-density side. As the bow swings over to this side, it begins to intercept more of the wind from this side than from the high-density side, and is eventually pushed back to the high-density side, where the whole process repeats itself in a quasi-periodic fashion. The higher value of α tends to homogenize the outflow of material in the direction of L_1 point. For $\alpha = 0.5$, we see origins of the formation of the focused stellar wind, whilst for the higher values of α the wind becomes more isotropic.

To illustrate the density distribution in the system, we have calculated column density along the line-of-sight to the X-ray source N_{H} in the orbital plane. Fig. 4.2 shows the absorbing column density as a function of orbital phase Φ derived from the simulation results in Fig. 4.1, and time-averaged over one orbital period. All profiles, each corresponding to a different value of α parameter, exhibit some common characteristics. At early phases, the smooth wind component dominates, followed by a rise in N_{H} starting from orbital phase ~ 0.25 . This increase represents the bow shock and the tail forming behind the accretion disk. However, the shape of the central part of the profile for various values of α differs significantly. For α equals to 0.6 and 0.7, we obtain a double peak structure which is a clear sign of well defined bow shock that accumulates most of the gas. In the case of $\alpha = 0.5$, the amount of gas captured in the accretion disk is significantly higher and the distribution of matter within the tail is more isotropic. The column density profile is, thus, more homogeneous with a growing trend towards the peak value around orbital phase ~ 0.67 . It declines from here to another local minimum at phase around ~ 0.78

4.3.2 Effects of the mass of the companion

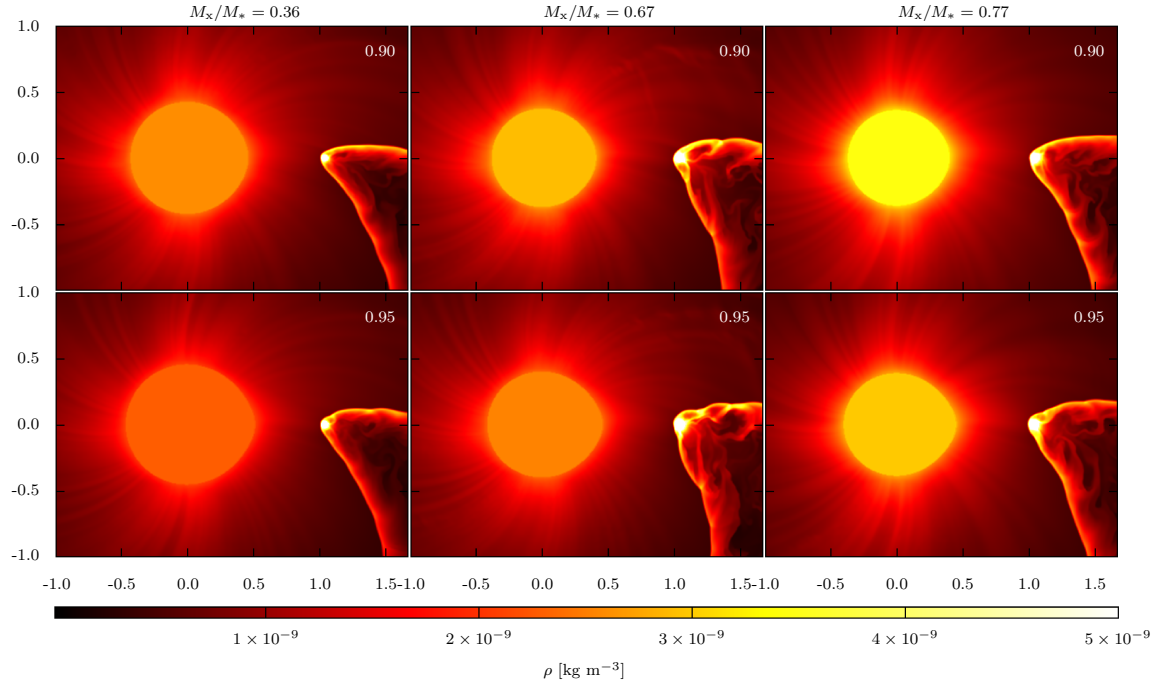


Figure 4.3: Similarly as in Fig. 4.1, this series of six two-dimensional simulations in the equatorial plane shows a dependency of the solution on the mass ratio M_x/M_* and the mean radius of the primary. The used masses of the primary and the compact companion for all three cases can be found in Table 4.2. The shape of the primary, represented by an equipotential surface, is a function of M_* and M_x . The white index in the upper-right corner of each panel represents the volume of the primary as a fraction of volume of the critical Roche equipotential. We disregard the effects of the X-ray ionization in these simulations. α is set to 0.6 and the value of k parameter is kept constant on 0.25. Changes among the simulations become more pronounced as we take into account the scale differences. For a given value of P_{orb} , D grows with the increasing value of the overall mass of the system. The panels show the density distribution after the solution reached the quasi-stationary state, $\sim 3P_{\text{orb}}$.

As stated at the beginning of this Section, there is no clear consensus on the masses of the both components of Cygnus X-1. We wish to investigate the effects that different masses and, consequently, ratios of M_x/M_* might have on the wind structure and dynamics. The gravitational potential of the compact companion affects the wind mass-loss rate and its distribution across the surface of the primary. The mass-loss rate is enhanced along the line of centres of the binary system via two related effects. The first one is the tidal distortion of the primary, which lifts the base of the wind farther away from the center of the primary in the direction of the compact companion. The second one related effect is the weakening of the gravitational force along the line of centres so the wind has to overcome less gravity in this direction. Thus, the mass-loss rate is strongly enhanced in the direction to the

Table 4.2: Parameters used in the simulations described in Sec. 4.3.2

Parameter	Case I	Case II	Case III
$M_x [M_\odot]$	8.7	16.0	14.81
$M_* [M_\odot]$	24.0	24.0	19.16
M_x/M_*	0.36	0.67	0.77

companion, giving rise to the highly anisotropic modulated stellar wind. This effect, however, is reduced by taking into account the gravity darkening of the photosphere of the primary.

The value of the mean radius of the primary, derived from the observations, is even less established than in the case of its mass. Thus, the need of investigating how the mean radius effects the wind structure and dynamics becomes apparent. The photosphere of the primary in our simulations is set to coincide with a selected surface of the effective equipotential with a given volume. The inner boundary condition is, thus, defined by specifying its volume as a fraction of the volume of the critical Roche lobe. We use two values of this parameter throughout all six simulations – 90% and 95% of the critical Roche equipotential.

In Fig. 4.3, there is a series of the two-dimensional simulations showing the density distribution of the stellar wind in the orbital plane. We used three sets of masses of the primary and the compact companion (see Table 4.2) with unique mass ratio indicated on the top of each column. The first column refers to one of the limiting cases of the range given by Caballero-Nieves et al. (2009) with the corresponding mass ratio $M_x/M_* = 0.36$. The second column represents the outcomes of the evolutionary models of the massive core hydrogen burning stars by Ziółkowski (2014) – low hydrogen content case – with $M_x/M_* = 0.67$. And the last column uses values found by Orosz et al. (2011) with $M_x/M_* = 0.77$. In the upper-most panels, the volume of the primary corresponds to the 90% of the volume of the critical Roche equipotential. In the bottom-most panels the value is 95%. Similarly to the previous simulations, we use the ideal gas with an adiabatic index $\gamma = 5/3$, and we do not take into account the effects of the X-ray ionization, $\xi = 0$. The value of k is kept constant at 0.25, and α is set to 0.6.

When looking at the results of our simulations in Fig. 4.3, it is important to point out that the spacial scale, with D as a unit of distance, is not constant. We determine D by specifying the orbital period P_{orb} and the masses of both component of the binary. Thus, by increasing the overall mass of the system, we also increase the distance unit D in the simulations. D defines the physical dimension of the computational region which is always set to $(2.66 \times 2)D$ in x and y -direction, respectively. Therefore, while the D changes, the relative distance between both component of the binary within the computational grid remains constant in all simulations. The size of the primary, on the other hand, is scaled up and down depending on the actual value of D . By changing the mass ratio M_x/M_* , we also change the shape of the effective potential and, consequently, the shape of the surface of the primary. To comply with our initial condition settings, we need to adjust ρ_0 with changing size of the

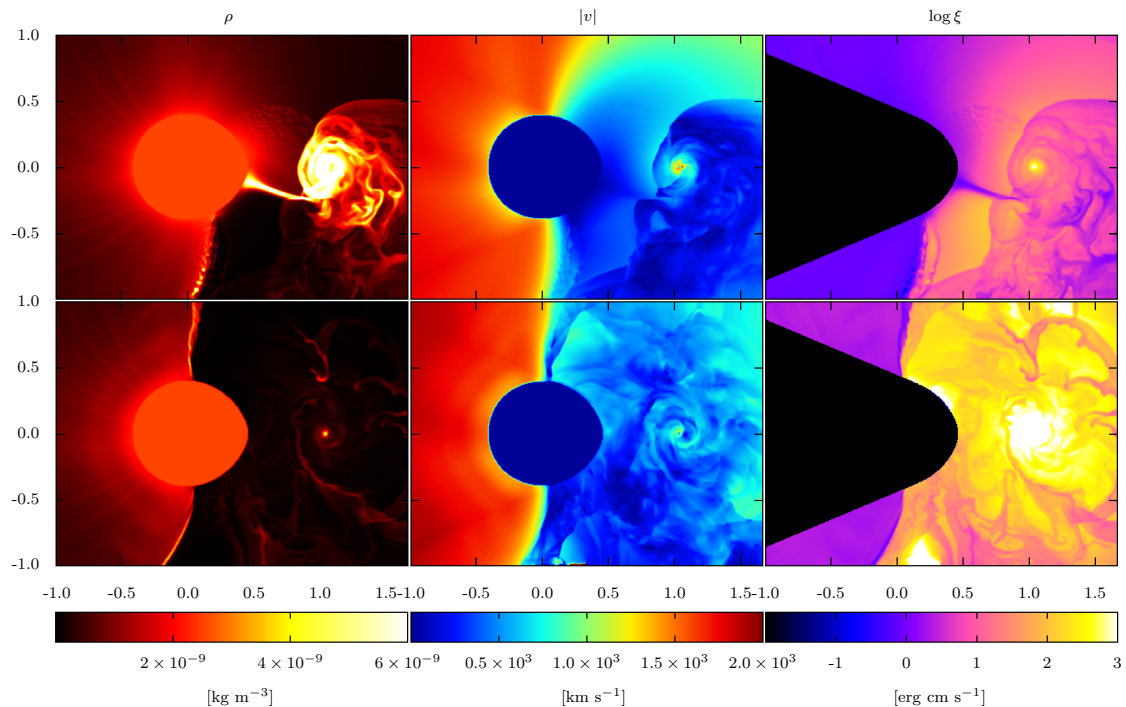


Figure 4.4: Two-dimensional simulations of the stellar wind in the equatorial plane of Cygnus X-1 including the effects of the X-ray ionization. Panels show the density distribution ρ , the velocity magnitude \bar{v} , and the ionization parameter ξ . α is set to 0.6, and $k = k(\xi)$. The wind lurching from the hemisphere facing the X-ray source is noticeably slowed down in comparison with the wind coming from the opposite hemisphere which lies in the X-ray shadow (the dark cone-like region in the right-most panels). A strong shock forms in the region where the fast and slow winds collide. The accretion of the slow wind is much more effective, giving rise to an extent disk that is enveloped by a strong shock front. In the region where $\log \xi \geq 2$, the line-driven acceleration mechanism of the material of the wind is switched off, resulting in the slow wind coming from the hemisphere facing to the X-ray source.

primary in order to obtain the initial pre-set mass-loss rate $\dot{M} = 2 \times 10^{-6} M_{\odot} \text{ yr}^{-1}$.

In Fig. 4.3, we conclude from the outcomes of our simulations that the effects of the arbitrarily chosen mean radius on the wind structure and dynamics are rather small. There are no qualitative changes in the solutions corresponding to the cases when the volume of the primary equals to 90% or 95% of the critical Roche equipotential. Even quantitatively, the solutions are virtually identical. The small-scale fluctuation are caused by numerical instabilities and generally random turbulent motion of the gas. Therefore, we will adopt value of 95% of the volume of the critical Roche equipotential as the volume of the primary in all following simulations.

The dependency of the solution on the mass ratio M_x/M_* seems to be of more importance. By increasing the mass of the compact companion M_x , we also increase the amount of matter captured in the accretion disk, thus, the bow shock grows larger. The matter is accumulated within the gravity well of the compact companion and then released in a quasi-periodic fashion. The interaction of these released

clumps with the rest of the shock give rise to the turbulent environment of the tail.

4.3.3 Effects of the X-ray ionization

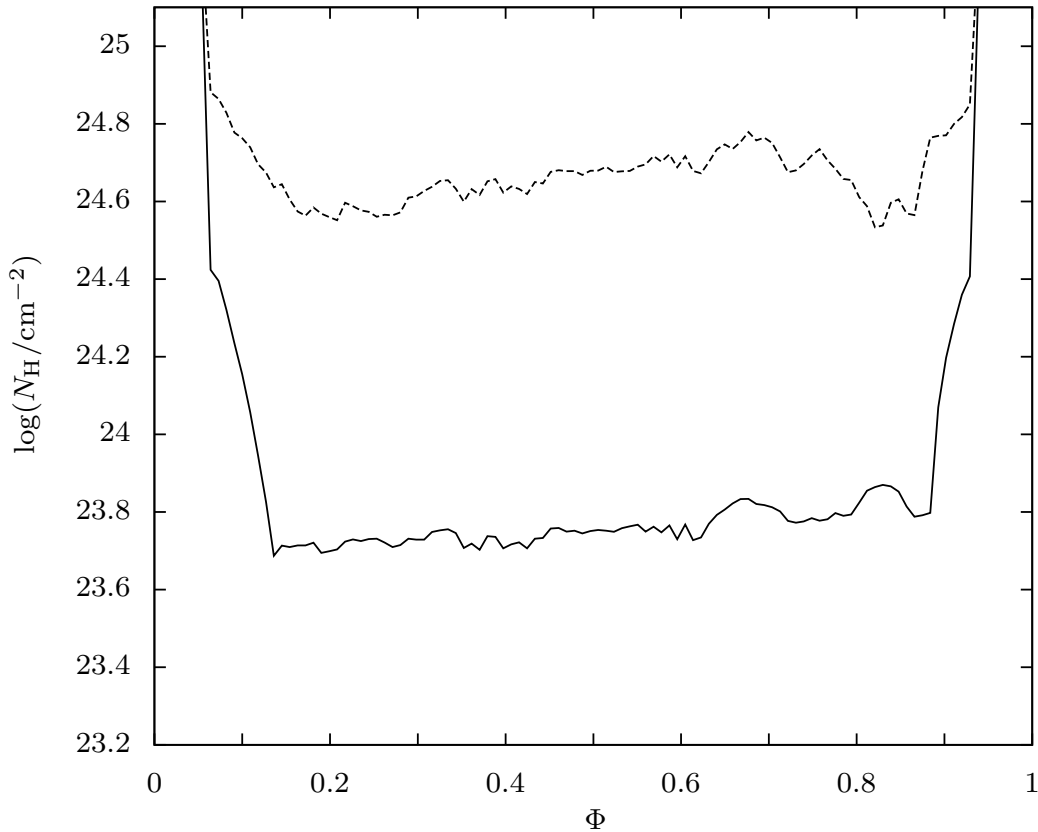


Figure 4.5: Integrated column density for the simulation shown in Fig. 4.4 as a function of orbital phase Φ time-averaged over one orbital period. The solid and dashed line correspond to the High/Soft and Low/Hard X-ray state of Cygnus X-1, respectively.

Up until now, we have neglected all effects of the strong X-ray source within the system on the wind from the primary. In the following two-dimensional simulations, we have expanded our physical model by identifying the source of the X-ray luminosity with the position of the compact companion. We have used parameters from Table 4.1 amended by the value of $\alpha = 0.6$, thus, making the results comparable with the previous simulations in Sec. 4.3.1 (the case of $\alpha = 0.6$), and in Sec. 4.3.2 (the case of $M_x/M_* = 0.67$). The ionization parameter ξ is now, in contrast to the previous physical model, computed as a function of the local quantities – gas density, X-ray luminosity, and the distance from the X-ray source – as indicated in Eq. (4.3). CAK parameters k and η have no longer fixed values. They are calculated as $k = k(\xi)$ and $\eta = \eta(\xi)$ according to Eqs. (4.5) and (4.6), respectively. We assume that the X-ray radiation field is blocked by the surface of the supergiant. The primary, thus, casts an X-ray shadow, leaving the region behind it relatively uninfluenced by the presence of the X-ray source.

In Fig. 4.4, we present the results of our simulations for two values of the X-ray luminosity. The upper panels, represent the case with the X-ray luminosity equal to $1.9 \times 10^{37} \text{ erg s}^{-1}$, thus, corresponding to the Low/Hard X-ray state of Cygnus X-1. The lower panels, then, show the case of the X-ray luminosity equal to $3.3 \times 10^{37} \text{ erg s}^{-1}$ which corresponds to the High/Soft X-ray state. Each column in Fig. 4.4 represents a different physical quantity. From the left, it is the density distribution ρ , the velocity magnitude $|v|$, and the ionization parameter ξ of the stellar wind in the orbital plane of Cygnus X-1.

It is evident, in comparison with the corresponding simulations in the previous Subsections, that the X-ray radiation field has a profound effect on the structure and dynamics of the wind. Ionizing the gas material severely limits the efficiency of the CAK line-driven mechanism and decreases the radiative drag on the wind. Even in the Low/Hard state, the outflow from the hemisphere facing the X-ray source is noticeably slowed down in comparison with the previous simulations. This is in direct contrast with the wind lurching from the opposite hemisphere lying in the X-ray shadow (depicted in the right-most panel of Fig. 4.4 as the dark cone-like region) where the wind is relatively unaffected by the presence of strong X-ray source. The shadow cast by the primary provides an environment where the wind can be accelerated without interruption, leading to velocities that are an order of magnitude higher than in the slow-wind region where the acceleration mechanism is impaired right at the base of the wind. Similarly to the simulation in Fig. 4.1, slowing down the wind caused the broadening of the bow shock which forms in front of the accretion disk around the compact object. The amount of the material captured in the accretion disk also increases.

The intensity of the stellar wind is highly anisotropic. In directions where the stellar wind coming from the facing hemisphere is additionally rarefied by the divergence of the streamlines, ξ parameter reaches its highest values, thus, effectively cuts off the outflow of the wind in these directions. The gas from these regions condensates into a narrow dense stream and passes in the vicinity of L_1 point in the direction of the compact companion. The mass-loss rate in the direction to the L_1 point is, thus, significantly enhanced. This focused stellar wind which resembles the Roche lobe overflow, interacts with the bow shock and the outer layers of the accretion disk. The region undergoes quasi-periodic changes in density. First, the material of the focused wind is accumulated by the bow shock. A part of it is accreted by the compact companion but most of it stick together in a form of a dense clump. When a critical density is reached, the whole clump is released and flows downstream out of the computational region.

Next to the interplay between the stellar wind and the compact companion, there is additional source of hydrodynamic shocks in this simulation. This shock is a direct consequence of the X-ray source in the system. The streamlines of the slow rarefied parts of the wind from the facing hemisphere are bent more by the Coriolis force and are brought to the region dominated by the fast less dense wind originating from the shadowed hemisphere. In the region that precedes the primary in orbit, both types of wind join together, giving rise to a strong shock. There is no hydrodynamic shock in the region that lags behind the primary in orbit because

the streamlines of the fast and slow wind diverge.

In the case of the High/Soft state (the bottom panels in Fig. 4.4), the increase in X-ray luminosity of the compact object effectively cuts off the outflow of the material from the entire facing hemisphere. The most prominent consequence of the increased X-ray luminosity is the disruption of the narrow dense stream between both components of the binary. The mass transfer from the primary to the accretion disk is, thus, interrupted and the accretion disk shrinks as the matter within it is accreted onto the compact companion. Lacking the incoming flow of gas to compress the accretion disk, the gas from the disk is scattered in the wide region around the compact companion. Without any prevailing velocity field, the movement of the gas in this region is mostly slow and turbulent. The bow shock around the accretion disk completely disappears. The hydrodynamic shock preceding the primary in orbit transforms into a contact discontinuity. The same phenomenon appears in the region that lags behind the primary in orbit.

Corresponding simulated time-averaged column densities for both X-ray states of Cygnus X-1 are shown in Fig. 4.5. The profile of column density of the Low/Hard state is similar to one in Fig. 4.2 for $\alpha = 0.5$. At early phases, the smooth wind component dominates, followed by a rise in N_{H} in orbital phase ~ 0.2 . Similarly, the column density in the central part of the profile gradually grows, although, the peak is not as sharp as in the case of $\alpha = 0.5$. When we increase the X-ray luminosity, in order to simulate the transition to the High/Soft state, the column density decreases as the gas is accreted onto the compact object or leaves its vicinity. The relative flatness of the central part of the profile suggests that, neglecting small-scale fluctuations in density, the gas around the compact object is distributed rather isotropically.

4.3.4 The three-dimensional model

Having developed and extensively tested our code in various two-dimensional simulations, we can now proceed with more complex and extensive three-dimensional simulation of Cygnus X-1. So far, we have studied the roles of particular parameters and their influences on the shape of the solution separately. In this Section, we present the results of the three-dimensional simulations that encompass the entire physical model described in Sec. 4.1. We employ an equidistantly spaced grid of $207 \times 157 \times 157$ computational cells in x , y , and z -direction, respectively. Similarly to the simulations discussed in Sec. 4.3.3, we use parameters appropriate for Cygnus X-1 from Table 4.1. We set α equal to 0.6. The ionization parameter ξ is calculated from Eq. (4.3) as a function of local gas density, X-ray luminosity, and distance from the X-ray source. The quantities $k = k(\xi)$ and $\eta = \eta(\xi)$ are functions of ξ according to Eqs. (4.5) and (4.6), respectively. The computational volume has a range of $x = [-1, 1.66] \times D$, $y = [-1, 1] \times D$, and $z = [-1, 1] \times D$, where $D = 3.16 \times 10^{10}$ m, yielding a spatial resolution of the computational grid $dl = 4.2 \times 10^8$ m. The primary star is centred at $[x, y, z] = [0, 0, 0]$, while the position of the compact companion is $[x, y, z] = [D, 0, 0]$. The time-step Δt is adjusted every computational step, satisfying the condition given by Eq. (3.8) and typically

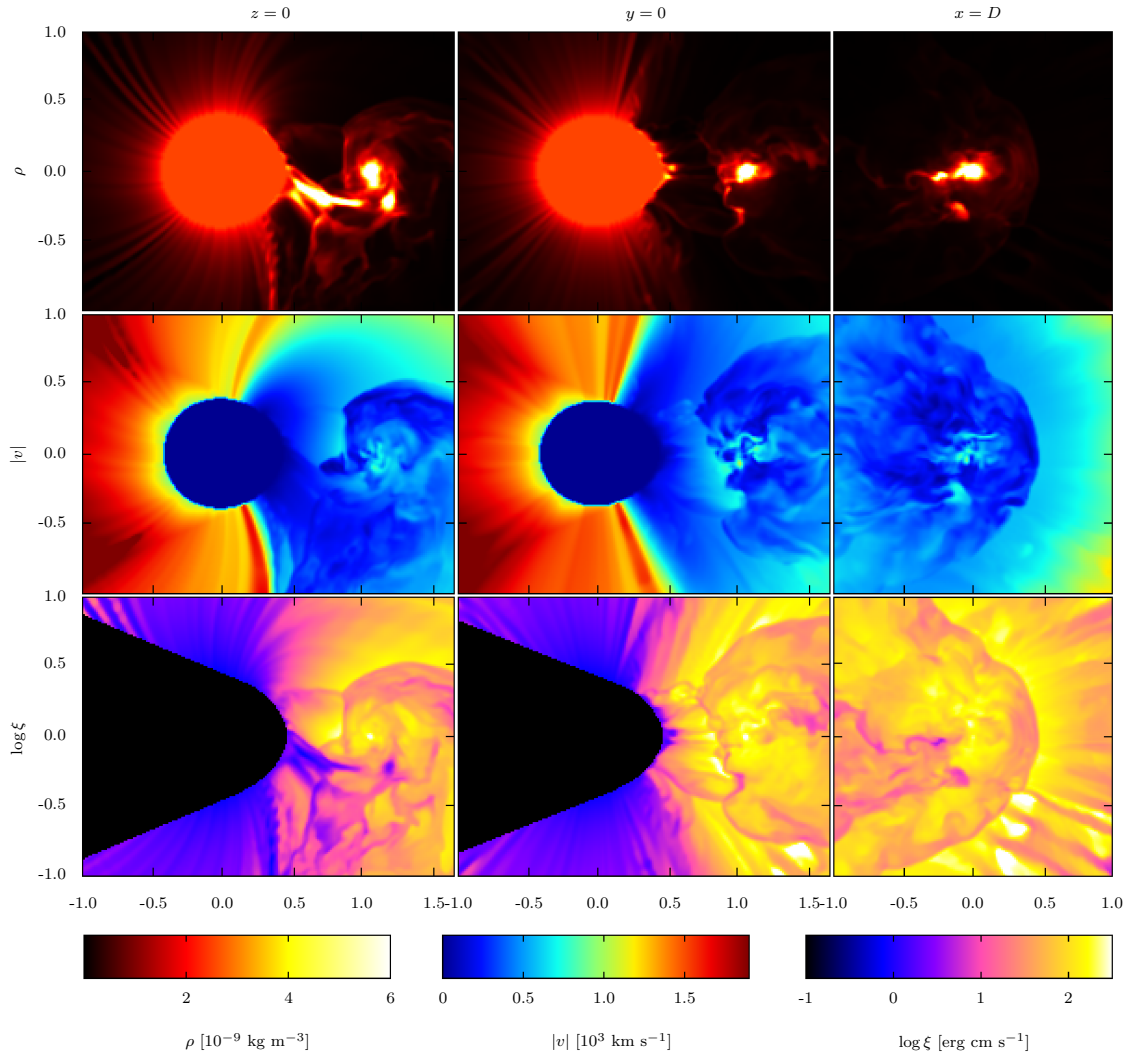


Figure 4.6: Three-dimensional simulation of the stellar wind of HD 226868 with the X-ray luminosity equal to $1.9 \times 10^{37} \text{ erg s}^{-1}$ corresponding to the Low/Hard X-ray state of Cygnus X-1. α is set to 0.6. $\eta = \eta(\xi)$, and $k = k(\xi)$ are functions of ξ . Columns show various cross-sections through the computational volume. All mutually perpendicular planes are centred on the compact companion and are defined as $x = D$, $y = 0$, $z = 0$. The displayed quantities are the density distribution (the top-most panels), the velocity magnitude (the middle panels), and the ionization parameter ξ (bottom-most panels).

reaching value of $\sim 10^{-4} P_{\text{orb}}$.

In the first simulation, we set the X-ray luminosity of the compact companion equal to $1.9 \times 10^{37} \text{ erg s}^{-1}$. This value corresponds to the Low/Hard state of Cygnus X-1, making the results directly comparable with the first simulation in Fig. 4.4. Fig. 4.6 shows various cross-sections through the computational volume. All planes, defined as $z = 0$, $y = 0$, $x = D$, are mutually perpendicular and centred on the compact companion. The displayed quantities are the density distribution (the top-most panels), the velocity magnitude (the central panels), and the ionization parameter ξ (bottom-most panels). The results of the three-dimensional simulation resemble

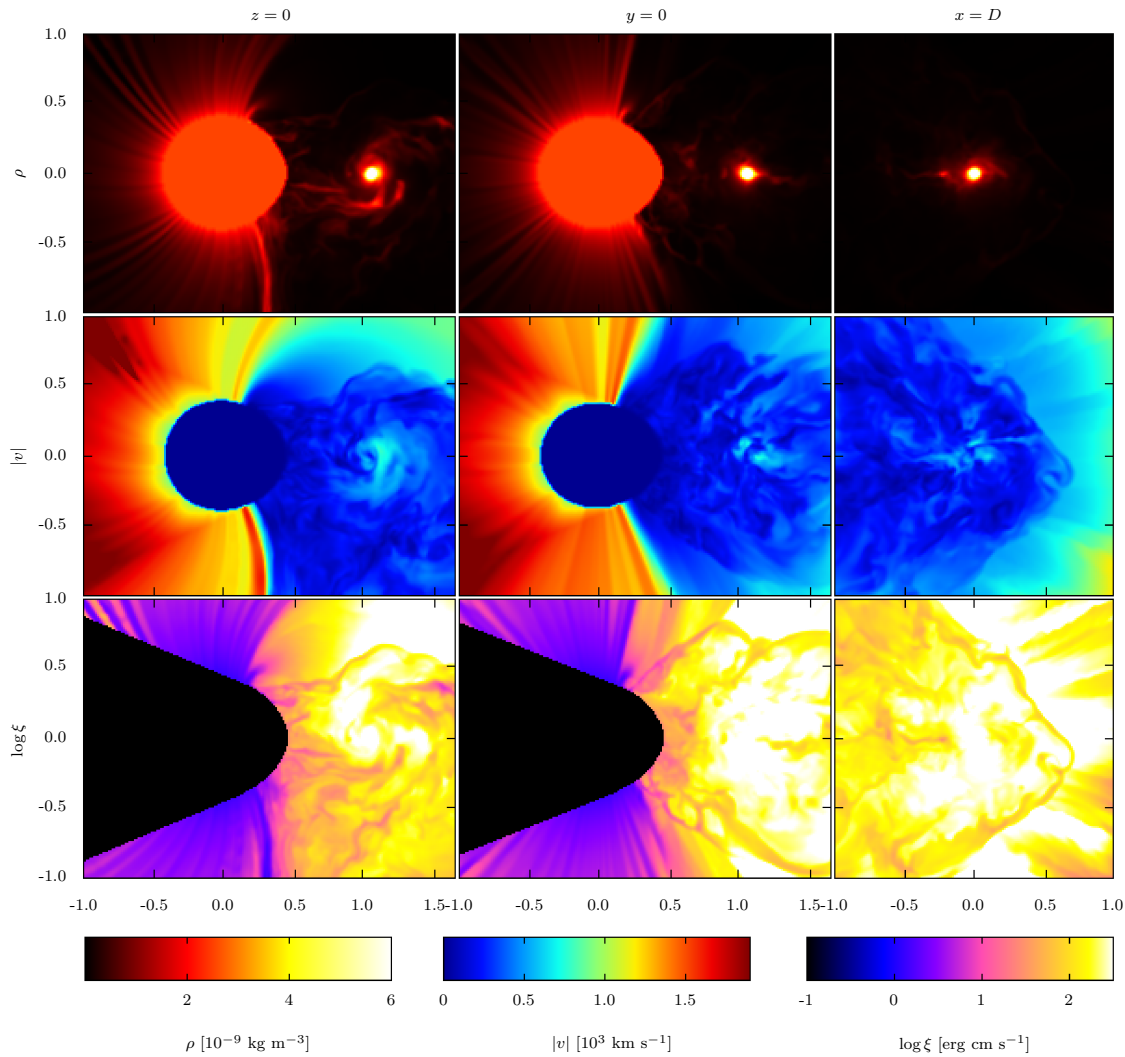


Figure 4.7: Three-dimensional simulation of the stellar wind of HD 226868 with the X-ray luminosity equal to $3.3 \times 10^{37} \text{ erg s}^{-1}$ corresponding to the High/Soft X-ray state of Cygnus X-1. α is set to 0.6. $\eta = \eta(\xi)$, and $k = k(\xi)$ are functions of ξ . Columns show various cross-sections through the computational volume. All mutually perpendicular planes are centred on the compact companion and are defined as $x = D$, $y = 0$, $z = 0$. The displayed quantities are the density distribution (the top-most panels), the velocity magnitude (the middle panels), and the ionization parameter ξ (bottom-most panels).

those acquired with the two-dimensional model. The most prominent feature in the orbital plane is a dense gas stream in the direction of L_1 point. The stream is brought to the proximity of the compact companion where it interferes with an extensive accretion disk enveloped by a bow shock. As the bow shock extends downstream, it creates a tail that has a similar turbulent nature as the one we saw earlier in the two-dimensional case in Fig. 4.4. We also have additional information about the vertical structure of the accretion disk and the tail. The accretion disk, especially its central region, is rather thick. This is likely caused by the insufficient grid resolution of the accreting region. One computational cell corresponds to over 4000

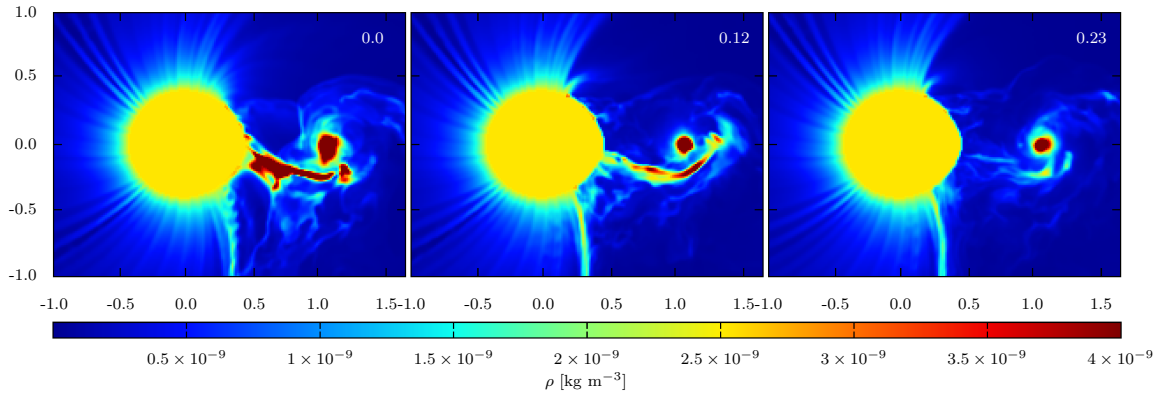


Figure 4.8: Evolution of the density distribution in the orbital plane of Cygnus X-1 showing gradual decay of the high density flow in the proximity of L_1 point. The left-hand side panel corresponds to the quasi-stationary solution representing the Low/Hard X-ray state of Cygnus X-1. The right-hand panel shows the outcome of the simulation when the new equilibrium is reached after adjusting the X-ray luminosity of the compact object to the level corresponding to the High/Soft state. The central panel represents a transient state roughly in the middle of the transition. The time index in the upper right corner of each panel is expressed in the units of P_{orb} .

Schwarzschild radii and several cells are needed in order to create a large enough pressure gradient to counter the gravitational force of the compact companion. The tail is mostly symmetric in the xz and yz -plane with a fine turbulent structure.

We also notice the second hydrodynamic shock in the region that precedes the primary in orbit where the slow wind hits the fast parts of the wind launched from the hemisphere in the X-ray shadow. The shock is less pronounced than in the two-dimensional case and also slightly shifted counter-clockwise with respect to the projection of the surface of the primary in the orbital plane. Similarly, we notice a spread of the region of the wind characterized by the fast solution. These effects are caused by the coarser computational grid we adopted in the three-dimensional case where the distance between two neighbouring grid nodes is roughly twice the distance in the simulations in Sec. 4.3.3. As a consequence, the subsonic region which lies in the immediate proximity of the surface of the primary and where the material of the wind is strongly accelerated, is not well resolved. This allows the wind to gain higher velocities before it leaves the X-ray shadow cast by the primary. There is no hydrodynamic shock in the region lagging behind the primary in orbit because, similarly to the two-dimensional case, the streamlines there diverge.

Density of the gas stream and, and consequently, in the inner parts of the accretion disk, is higher approximately by factor of 2 in comparison with the two-dimensional case. This increase is caused by the gravitational force which focuses the streamlines of the wind launched from the higher latitudes of the surface of the primary into the orbital plane and, thus, brings more material into the stream. There is also an overall increase of velocity of the wind in the region of the X-ray shadow. This increase originates from the different geometrical formulation of the problem. In the two-dimensional simulation, gas pouring inside the computational

region from the inner boundary condition is diluted as $1/r^2$ as it advances towards the outer boundary. In the three-dimensional case this dilution factor is $1/r^3$. Density of the wind, therefore, generally decreases more quickly with the distance from the primary in the three-dimensional case. As a result, the line-driven force is enhanced since Eq. (4.7) is inversely related to the local density. This effect becomes more important further away from the surface of the supergiant in the region of the X-ray shadow where it is not influenced by the ionization. Velocity of the outflowing gas in those regions is increased by approximately 10%. On the other hand, lower density increases the value of ξ parameter. In the regions close enough to the X-ray source, the drop of k parameter with growing ξ in Eq. (4.7) completely nullifies and, in some regions, even surpasses the effect of lower density on the velocity structure of the wind. There is also a numerical artefact due to the poorer resolution in the three-dimensional simulations which enables the small tangential variations in density and velocity of the wind. This artefact is caused by the roughness of the inner boundary condition and grows stronger as the computational grid becomes less refined. Especially, streamlines lurching from the transient region between areas in the X-ray shadow and the areas that are completely exposed to the X-ray source, are strongly influenced.

The simulation evolves for $2.5 P_{\text{orb}}$ and reaches a quasi-stationary state in $\sim 1 P_{\text{orb}}$ after which we observe only quasi-periodic releases of material accumulated in the vicinity of the compact companion. At $2.5 P_{\text{orb}}$ after the beginning of the simulation, we abruptly increase the X-ray luminosity of the compact object to $3.3 \times 10^{37} \text{ erg s}^{-1}$ corresponding to the High/Soft state of the Cygnus X-1. The new equilibrium is found relatively quickly after around $0.25 P_{\text{orb}}$ which roughly corresponds to the time needed for the gas lunched from the facing hemisphere to leave the computational area. The results of the simulation after the new quasi-stationary solution is reached are shown in Fig. 4.7. The planes defining the cross-sections of the computational volume are the same as in the previous case. The displayed quantities are the density distribution (the top-most panels), the velocity magnitude (the central panels), and the ionization parameter ξ (bottom-most panels).

We notice that the parametric change of X-ray luminosity significantly influences gas dynamics in the vicinity of Cygnus X-1. While the wind, lunched from the parts of the surface of the primary that lie in the X-ray shadow, is relatively unaffected, the wind originating from the facing hemisphere experiences dramatic changes as the CAK line-driven mechanism is seriously impaired. As the ξ parameter grows, the efficiency of the momentum transfer between the material of the wind and the radiation field declines. At this value of the X-ray luminosity the bubble of full ionization (approximated by the condition $\log \xi \geq 2$) almost reaches the surface of the supergiant, thus, preventing the wind to achieve the escape velocity. The wind falls back and the outflow of the material in the direction of L_1 point is interrupted. The process of disruption of the dense stream of gas between the components of the binary is depicted in Fig. 4.8 where we show the density distribution in the orbital plane. The decline of the dense gas stream is a quick process, it takes only around $0.2 P_{\text{orb}}$ since the increase of the X-ray intensity, before it vanishes.

As the gas in the accretion disk gets accreted and the transfer of the new material

from the primary is obstructed, the accretion disk becomes less dense and shrinks in size. Eventually, the whole material entrapped in the gravity well of the compact companion would be accreted and the accretion disk would cease to exist. This would, however, require a considerably longer duration of the simulation which is beyond our computational capabilities.

4.3.5 3D visualization

For illustrative purposes, we produced an interactive figure (Fig. 4.9) containing an iso-density surface for $\rho = 2.5 \times 10^{-9} \text{ kg m}^{-3}$. The iso-density surface corresponds to the Low/Hard X-ray state of Cygnus X-1 from the simulation presented in Fig. 4.6. This approach allows us to visualize the global distribution of the accretion disk and the hydrodynamic shocks.

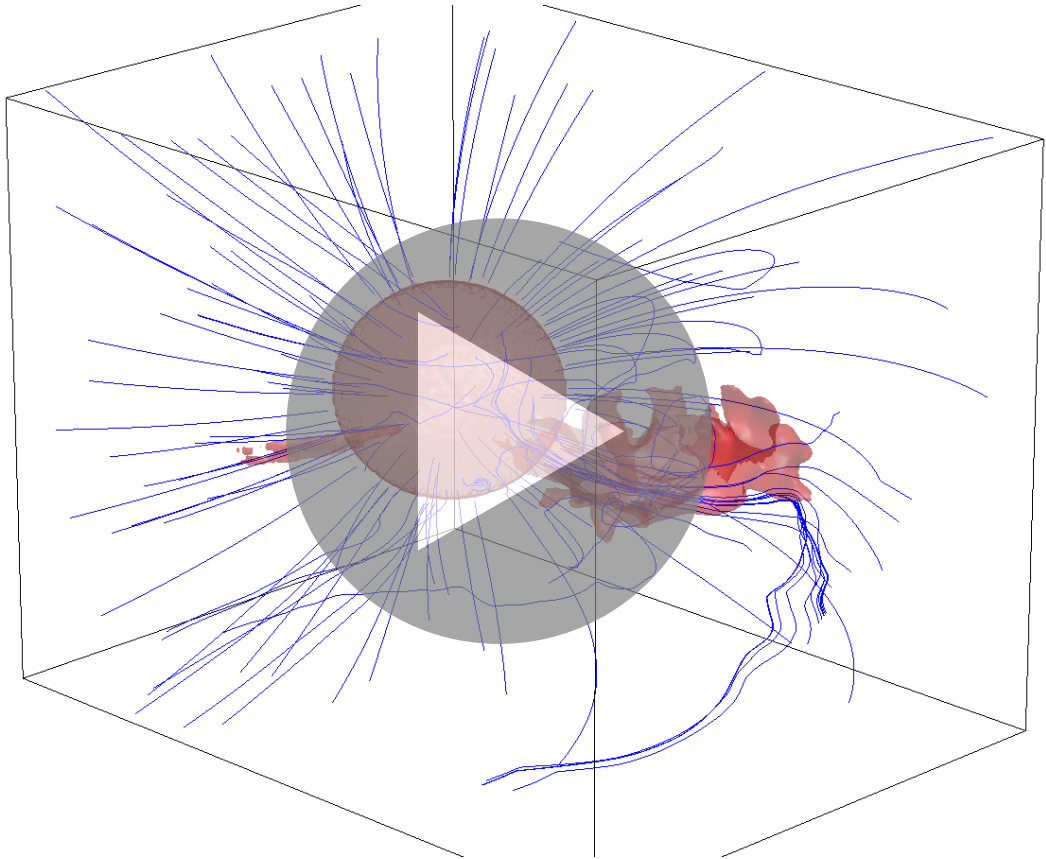


Figure 4.9: Interactive three-dimensional iso-density surface for $\rho = 2.5 \times 10^{-9} \text{ kg m}^{-3}$. The blue curves represent streamlines of the stellar wind.

Chapter V

Doppler tomography

Until now, we have examined the mass transfer process in high-mass X-ray binaries through the predictions of our radiation hydrodynamic model. But is there a way to determine if the numerical results correspond to observations? Even with a precipitous advance in observational techniques and instrumental equipment in the last decades, we can not simply point our telescopes to an X-ray binary system in order to 'take a look' what the distribution of matter around the star may be like. The X-ray binaries are far too small to be observed through direct imaging – they typically subtend $< 10^{-4}$ arcsecond when observed from Earth. In order to learn something about the wind structure, we have to use more indirect methods like Doppler tomography that resolves the accretion flow in binaries on micro-arcsecond scales using time-resolved spectroscopy. This technique (similar in principle to medical CT scan) utilizes binary spectral line profiles taken at a series of different orbital phases and transforms them into a distribution of emission over the binary.

At the beginning of this Chapter, we will introduce the Doppler tomography as an indirect imaging method, following Marsh (2001). We will discuss its basic principles, including a description of maximum entropy regularization which will be implemented on the observational data later. Following this, we discuss an extension to Doppler tomography that relaxes one of its fundamental axioms and permits the mapping of time-dependent emission sources. In Sec. 5.6, we will apply the Doppler mapping on new optical data of Cygnus X-1, a part of which we observed at the Ondřejov observatory in 2013. The spectra were taken during all major X-ray spectral states of Cygnus X-1, and we intend to analyse them separately, in order to determine the structural changes of the stellar wind during the transition event. In Sec. 5.7, we will introduce a novel data interpretation method based on the results of our radiation hydrodynamic model (discussed in Chapter IV) for the distribution of circumstellar matter in HDE 226868/Cygnus X-1 system.

5.1 Introduction

The presence of prominent emission lines in spectra of close binaries is one of the indications of a circumstellar matter which can feed the accretion on the compact companion. The highly structured and time-dependent emission line profiles ob-

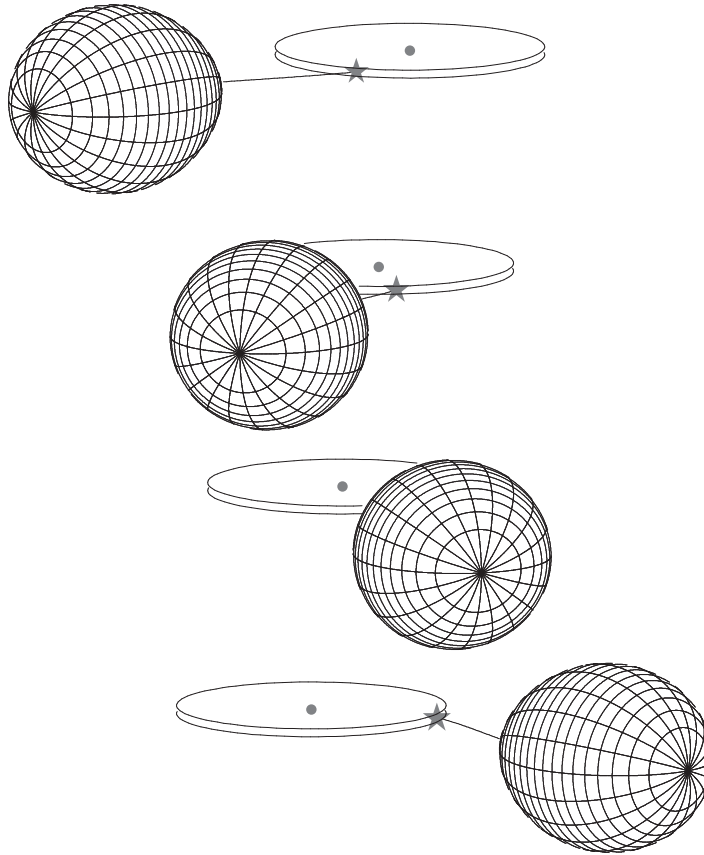


Figure 5.1: A schematic illustration of a cataclysmic variable viewed from four orbital phases (Marsh 2001).

served in cataclysmic variables and X-ray binaries provide us with additional information about the distribution of emission in such systems. Since the flow is highly supersonic, the overall line profile is determined by the dynamics of the flow rather than by the local properties of the gas material, thus providing a direct kinematic signature of the accretion structure (Smak 1981; Horne & Marsh 1986). This motivated the development of Doppler tomography (Marsh & Horne 1988) as a tool to reconstruct the image of the accretion flow from the observed line profiles in CVs. Even though the Doppler tomography was originally developed for CVs, its applicability is not restricted to them. The basic layout of X-ray binaries is virtually identical to CVs so we start by describing our standard picture. Fig. 5.1 shows a schematic representation of our model of X-ray binary with a compact companion surrounded by a flat disk, orbiting a tidally distorted main sequence star. In addition a stream of matter flows from the main sequence star and hits the disk in a bright spot. In eclipsing binaries, as seen in Fig. 5.1, the main-sequence star occults

the accreting region allowing us to locate the primary source of emission. This is what led to the development of the standard model of CVs in the early 1970s (Smak 1979; Wood et al. 1986).

One of the underlying assumption of classical Doppler tomography is that the source of the emission remains constant throughout the period of observation. For many rapidly rotating single stars and binaries, we find that the distribution of emission changes little in the course of a single rotational period. The spots on a single star surface can persist for many days, while cataclysmic variable stars may stay in outburst for over 100 orbits and in quiescence of an order of magnitude longer. The frequency of transitions of the X-ray spectral states in X-ray binaries – suggesting large matter redistribution in such systems – shows that the viability of various spectral state can stretch from several weeks to many years. However, from the observer’s perspective, orbital motion can cause considerable variability both in flux and spectra. This arises from a combination of changes in aspect angle and visibility, caused by geometrical effects, and the rotation of all velocity vectors with the binary orbit. These effects are very complex and the variability of the source can be hard to interpret, nonetheless, without them we would know considerably less about such stars.

5.2 The principles of Doppler tomography

To understand the basic concept of the Doppler tomography, first we have to consider a point-like source of emission in a binary. Assuming this has a motion parallel to the orbital plane of the binary, line emission from such a source will trace out a sinusoid around the mean velocity of the system. Assuming one observes such a sinusoid, one can associate it with a particular velocity vector in the binary, depending upon its phase and amplitude. We have to cope with any number of such sinusoids, even when they are so overlapped and blended that one cannot distinguish one from another.

The observational data used in Doppler tomography are sets of velocity-resolved line profiles covering a variety of phases across the binary orbit. For identifying subtle patterns in the data, it is useful to assemble the spectra into two-dimensional trailed spectrogram which shows the observed flux density as a function of wavelength λ (or velocity v) and binary phase Φ . These may exhibit double-peaked emission lines from an accretion disk, narrow S-waves components (following sinusoidal velocity curve) from the donor star, and a single-peaked (often blue-shifted) components possibly from the stellar winds.

There are two main methods used for implementing Doppler tomography. We will discuss both of them briefly here, for detailed description – cf., e.g Marsh & Horne (1988); Marsh (2001). The first one is based upon the maximum entropy regularisation used by Horne (1985). In this method we divide velocity space into many elements and seek the image of maximum entropy for a given goodness of fit measured with χ^2 . The advantage of this approach is production of a model fit which can be compared directly with the observational data. A second approach is also a linear method which directly inverts the integrals defining the emission line

formation by projection (the Radon transform). Most common employed method is 'filtered back-projection'. This is fast to compute, although speed is usually only an issue if hundreds of maps are being computed.

5.2.1 Profile formation

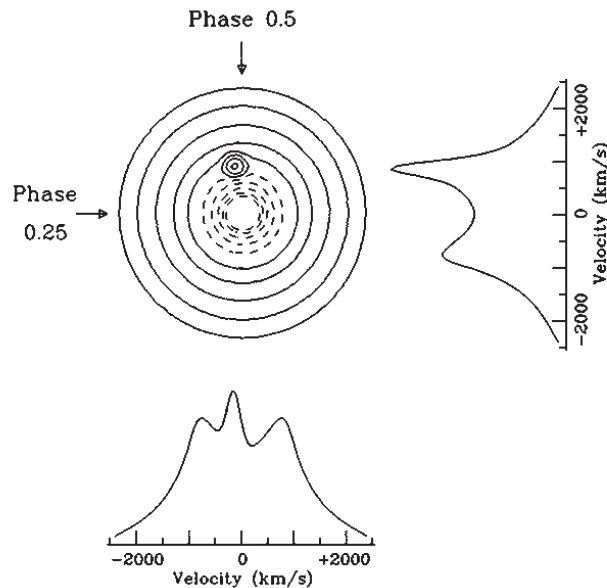


Figure 5.2: A model image and the appropriate spectral line profiles formed by projection at orbital phases 0.25 (right-most profile) and 0.5 (lower profile) (Marsh & Horne 1988).

Every given parcel of gas can be defined by both position, (x, y, z) , and velocity (v_x, v_y, v_z) . This velocity coordinates are relative to the inertial rather than co-rotating frame. In many interesting cases (gas stream and accretion disk for example), the small v_z component allows us to treat the motion as a two-dimensional problem confined to the orbital plane. Since we observe the radial velocities of the emitting material in the line profiles through Doppler shifts, the choice of working in velocity space is one of the major advantages of standard Doppler tomography. The inertial frame velocities, however, are constantly changing as the binary rotates, so it is convenient to define unique values of v_x and v_y corresponding to a particular orbital phase. Conventionally, this is taken to be when the inertial frame lines up with the co-rotating frame. In the case of X-ray binaries it is common to define the x -axis (in the co-rotating frame) to point from the compact companion to the mass donor, and the y -axis to point in the direction of motion of the mass donor. With this convention, and by defining orbital phase equal to zero at the moment when the donor star is closest to us (time of the X-ray minimum for the eclipsing X-ray binaries), the radial velocity of the gas parcel as a function of orbital phase Φ is given by

$$v_r(v_x, v_y, \Phi) = \gamma - v_x \cos(2\pi\Phi) + v_y \sin(2\pi\Phi), \quad (5.1)$$

where γ represents the systemic radial velocity of the binary.

While not perhaps as intuitive to interpret as spatial images in the Cartesian (x, y) frame, Doppler tomograms in velocity space (v_x, v_y) can be obtained without prior assumptions about the velocity field in the flow as a function of position. This significantly simplifies the inversion process and allows application of Doppler tomography in a variety of conditions where the nature of the flow is not a-priori known. A disadvantage is that two distinct parcels of gas can have precisely the same velocity coordinates, and this must be kept in mind when interpreting Doppler tomograms.

One way of thinking about the relationship between the Doppler map and the trailed spectrogram data is: if you project the Doppler map along various directions, by integration between pairs of parallel lines crossing the map, you obtain a set of velocity profiles for each of the corresponding binary phases. These predicted velocity profiles must fit the observed line profiles. From the second viewpoint, we may consider each pixel on the Doppler map, labelled with its velocity coordinates, as a particular S-wave component that follows a sinusoidal velocity curve. A trailed spectrogram is produced by summing up the S-waves components from all the pixels of the Doppler map.

5.2.2 Filtered back-projection

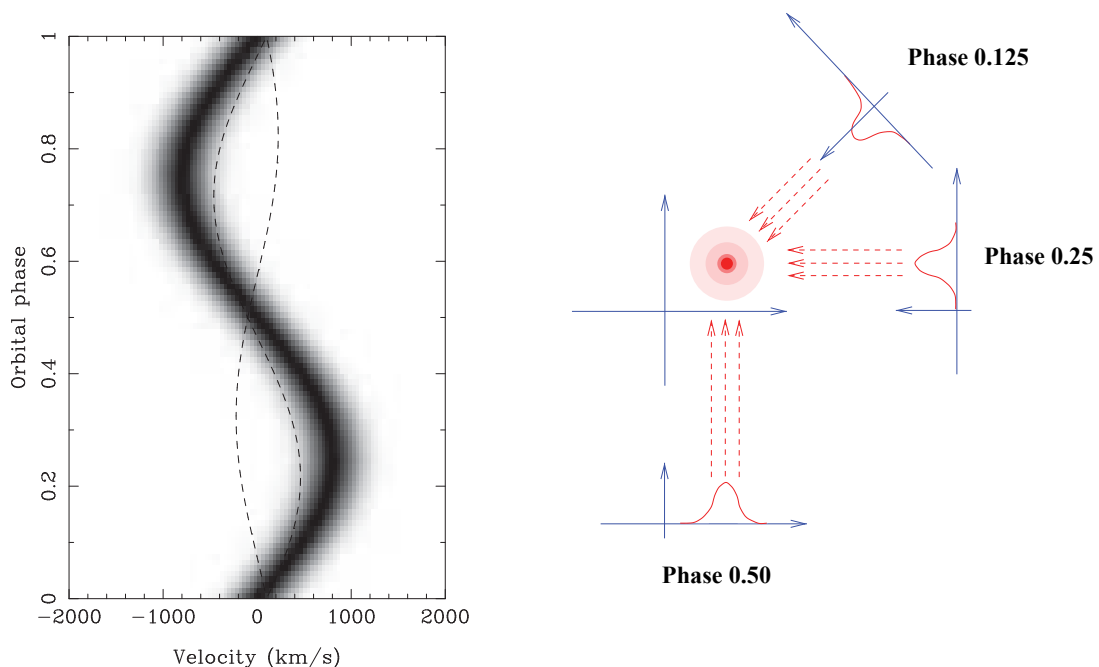


Figure 5.3: Two views of back-projection: on the left are paths of integration through trailed spectra (spectra plotted as grey-scale images with time running upwards and wavelength from left to right). A track close to a sinusoidal component gives a spot in the final image. On the right three profiles are smeared back along their original projection directions to give a spot (Marsh 2001).

This process can be summarized in the two following steps. First, the line profiles are filtered in velocity to derive modified profiles and then we use the back-projection to obtain the Doppler map. In Fourier space, the filter is proportional to $|k|$, where k is the wave number, and hence enhances higher frequencies. Applying the Fourier filter involves computing the Fourier transform of the each of the observed spectra, multiplying the resulting Fourier amplitudes by the Fourier filter, and then inverse Fourier transforming to recover the Fourier-filtered spectrum.

The Fourier filter needed to correct for back-projection's point-spread function turns out to be a high-pass RAMP filter. Each Fourier component of the observed spectrum must be amplified in proportion to its Fourier frequency. A potential problem with the Fourier filter is the amplification of high frequency noise. This may not be too serious in practice if the signal-to-noise ratio of the data are reasonably high. However, in real observed spectra, there is always a noise component present to some extent and the signal-to-noise ratio can be poor at the highest Fourier frequencies. A practical remedy is to curtail the high frequency ramp filter by including a Gaussian cutoff.

The second step is that of the back-projection. We can understand the process as an each point in the image can be built by integration along a sinusoidal path through the trailed spectrogram. The particular sinusoid is exactly that which a spot at the particular place in the image would produce in the trailed spectrum. This is illustrated on the left panel of Fig. 5.3. Another way how to read this process is that the image is built up by smearing each filtered profile along the same direction as the original projection which formed it. This way of looking at back-projection shows very clearly why small numbers of spectra cause linear artefacts in Doppler maps as illustrated in Fig. 5.4. Similarly, any anomalies, such as unmasked cosmic rays, dead pixels, flares or unmasked eclipses are liable to cause streaks across Doppler maps.

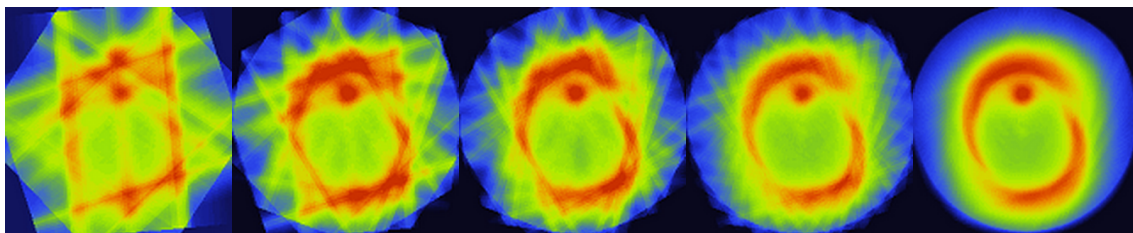


Figure 5.4: The influence of the number of spectra on the Doppler image. Resulted images (from left to right) were created from 4, 8, 10 and 15 spectra selected in regular interval. The final image is obtained with 57 spectra interpolated from the 15 original ones. (Illustrative picture adopted from http://www.astrosurf.com/rondi/spectro/doppler_tomography.htm, credit to André & Sylvain Rondi.)

5.2.3 Maximum entropy inversion

The maximum entropy regularization method (MEM) is probably the best way to reconstruct Doppler maps from the trailed spectrogram data. Its application to

Doppler tomography is based on adjusting a grid of pixels spanning velocity space to achieve a reasonably good fit of the observed data. This goodness is measured by χ^2 . In general, there is an infinite number of such images and so the image of maximum entropy is selected. A refined form of entropy which measures departures from a default image is used. Usually a moving default is used, computed as a blurred version of the image. This constrains the map to be smooth on scales shorter than the blurring, but fixed by the data alone on larger scales. For reasonable data, the choice of default appears to have little effect on the final reconstructed image. A thorough description of MEM is given by (Marsh & Horne 1988), including tests with simulated datasets to illustrate various artefacts due to noise, finite spectral and phase resolution of the data, blending of the adjacent spectral lines, and occultation effects.

MEM requires a sophisticated algorithm to search through the space of all positive maps to find the map with maximum entropy subject to the data consistency constraint. Such algorithms are generally iterative, and require hundreds or thousands of more computer time than the previously described back-projection method. Even so, for single images, the absolute amount of time taken is not large, especially when compared with the steps taken to get the data in the first place.

5.3 Axioms of Doppler tomography

Standard Doppler tomography reconstructing the distribution of line emission in the binary in a velocity coordinate frame rests on certain approximations to reality that are, at best, only partially fulfilled. The basic axioms as given by Marsh (2001) are shown below:

- All points are equally visible at all times.
- The flux from any point fixed in the rotating frame is constant.
- All motion is parallel to the orbital plane.
- All velocity vectors rotate with the binary star.
- The spectral line from any point has a profile of a δ -function.

Violations of these assumptions do not imply that Doppler tomography cannot be performed, or that the maps are meaningless, but these assumptions must be borne in mind when interpreting Doppler maps. As such, the tomogram is a representation of the observed data given the above assumptions and the accuracy and reliability of that representation is thus intimately tied in with the validity of the above axioms.

Exceptions exist to each of these axioms. For instance, the local line profile is expected to be set by a thermally broadened profile, contributing to a width of order 10 km s^{-1} for typical temperatures. Compared to Doppler velocities of hundreds to thousands of km s^{-1} makes axiom 5 generally satisfied under a wide range of conditions. However, non-thermal broadening mechanisms may be at work in parts of the flow, and can, in particular, affect low velocity emission. Axioms 3 and 4 can

be violated in parts of the flow, but the derived Doppler map should then be seen as approximations whereby the flow is projected onto the orbital frame of the binary and the map provides a time averaged representation of the flow in the co-rotating frame. Axiom 1 is usually the most challenging to deal with since we do not generally know the full geometry of the flow that is being mapped. After all, the whole point of Doppler mapping is to probe this geometry. In high inclination systems, self-shadowing effects may play a role, and complicate the analysis of emission line profiles.

5.4 Modulated Doppler tomography

The remaining axiom from the previous Subsection, is that the flux from each point in the co-rotating frame is assumed to be constant in time. However, observations show that the typical emission sources one is mapping modulate their flux in time. This can be because the line source emits anisotropically (e.g. the emission from density waves and shocks in an accretion disk) or because axiom 1 is violated and the geometry is responsible for a strong modulation of the flux (e.g. the buried bright spot) or a combination of both. Doppler tomography can still be used in that case, since the Doppler map serves to present a time averaged image of the distribution of line emission, ignoring such a phase dependent complications altogether. However, one will not be able to fit the data very well, and the phase dependent information contained in the observed line profiles is lost.

This motivated the development of an extension of classical Doppler which tomography has been introduced by Steeghs (2003) in order to allow mapping of time-dependent emission sources. Significant variability on the orbital period is a common characteristic of the emission sources that are observed in the accretion flows of cataclysmic variables and X-ray binaries. Modulation Doppler tomography maps sources varying harmonically as a function of the orbital period through the simultaneous reconstruction of three Doppler tomograms. One image describes the average flux distribution like in standard tomography, while the two additional images describe the variable component in terms of its sine and cosine amplitudes. We describe the implementation of such an extension in the form of the maximum entropy based fitting code MODMAP (Steeghs 2003). Test reconstructions of synthetic data illustrate that the technique is robust and well constrained. Artefact free reconstructions of complex emission distributions can be achieved under a wide range of signal to noise levels.

MODMAP employs the MEM which is advantageous since a back-projection would suffer from serious cross-talks among the three image terms and produces significant imaging artefacts. It uses the MEMSYS algorithm (Skilling & Bryan 1984) in order iteratively adjust the Doppler images while achieving a user specified χ^2 . The algorithm gradually steers toward the requested χ^2 value while maximizing the entropy of the image in order to converge to a unique solution. It delivers the simplest image that can fit data to the specified level, where simplicity is measured by the image entropy. Since the entropy is only defined for positive image values, but the cosine and sine amplitudes of the modulation can be both positive or negative,

the Doppler image vector passed to the fitting code is split into a sequence of five velocity maps. The first image array represents the average image values, while the cosine and sine values are represented by two image arrays each. For those two images, one image reflects positive amplitudes, the other negative amplitudes. In this way all possible modulations are included while a positive image vector is maintained under all circumstances for which an entropy can be defined.

5.5 The application of Doppler tomography

Before we move on to discuss Doppler tomography results in the context of Cygnus X-1, we consider the interpretation of Doppler maps of CVs and X-ray binaries.

5.5.1 Interpreting Doppler maps in X-ray binaries

Based on the standard model presented in Sec. 5.1, one can easily predict the locations of the various components in velocity-space. Fig. 5.5 shows some of the key components of an interacting binary represented in velocity space.

X-ray binaries with a large accretion disk can produce strong optical emission lines, with double-peaked velocity profile arising from the nearly Keplerian orbital motion within the accretion disk. This nearly Keplerian velocity field of the disk gives rise to a distorted 'inside-out' image of the disk in the velocity space. Gas flowing with constant velocity at a circular orbit will map into a circle with a radius equal to the orbital speed. This property is somewhat misleading, since the disk ends up being turned inside-out because the outer rim of the disk, where the Keplerian velocity is smallest, maps into the inner edge of the Doppler image. Since the gas in the accretion disk orbits around the compact companion, orbital motion of the companion around the center of mass of the system will cause the centroid of the disk's Doppler image to be displaced downward on the map to $v_y = -K_1$, where K_1 is the semi-amplitude of the companion's orbit.

The mass-losing primary star is assumed to co-rotate with the binary, which means that it appears with the same shape in velocity as it does in position coordinates, although rotated by 90° owing to the relation $\mathbf{v} = \boldsymbol{\Omega} \times \mathbf{r}$ between velocity and position for solid-body rotation. Line-forming regions on the donor star map into a Roche-lobe-shaped region centred at $v_y = +K_2$, where K_2 is the radial velocity semi-amplitude of the orbit of the primary star around the center of mass of the system. The location of the Doppler image of the Roche lobe generally lies inside the inner edge of the Doppler image of the disk, since the orbital velocity of the donor star is less than the Keplerian velocity within the disk.

The core of the gas stream follows a ballistic trajectory starting from the facing hemisphere of the mass-losing star and reaching down to the collision point on the outer rim of the disk. The expected location of emission from the gas stream may be calculated by integrating the ballistic equations of motion in the co-rotating reference frame of the binary. The velocity vectors at different points along the ballistic trajectory define a curve in the Doppler map starting at the image of the surface of the donor star, accelerating first in the v_x -direction, and gradually curving

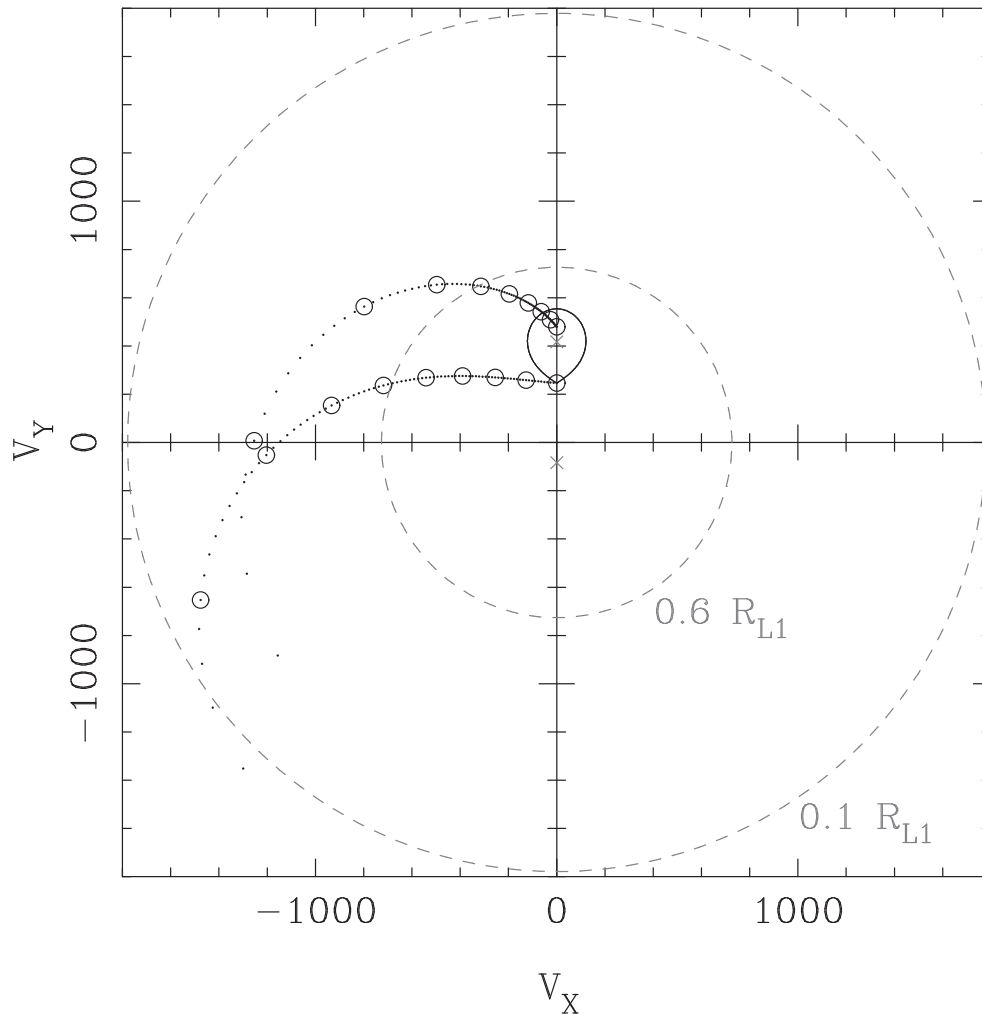


Figure 5.5: A schematic depiction of some key components in velocity coordinates (Marsh 2001).

toward the v_y direction due to the Coriolis force. Emission may also be expected at the disk's Keplerian velocity evaluated at locations along the stream trajectory, since the disk material may be excited to emission as the stream material skims across its surface. This second trajectory is similar to the first one but it is displaced slightly upward. Intermediate cases of the emission are also possible.

The positions of the critical Roche equipotential also displayed in Doppler maps is fully specified by the projected orbital velocities of the two stars, K_1 and K_2 , and orbital period. The overall scale is set by $K_1 + K_2$; their ratio, which is the mass ratio $q = K_1/K_2 = M_1/M_2$, defines the detailed shape of the stream and Roche lobe. The orbital phase sets the orientation of the image, and if it is not known the image will be rotated by an unknown amount relative to the standard orientation shown in 5.5.

5.6 Doppler imaging results for Cygnus X-1

In order to perform the Doppler mapping of Cygnus X-1, we have collected spectroscopic data from 2-m telescope at Ondřejov observatory of the Astronomical Institute of the Academy of Sciences of the Czech Republic, and 2.16 m telescope at Xinglong station of National Astronomical Observatories, China (NAOC). The data consist of isolated measurements as well as several series of observations, and cover a period between 2003 to 2013. At the Ondřejov observatory, 89 spectra were obtained with CCD in the focal point of 700 mm camera of Coudé spectrograph. A typical resolution is about 0.25 \AA per pixel. At the Xinglong station, additional 18 spectra were acquired with a CCD grating spectrograph at Cassegrain focal point of the telescope with an intermediate resolution of 1.22 \AA per pixel. The spectra were taken in all major X-ray spectral states of Cygnus X-1, namely in Low/Hard, High/Soft and Intermediate state. The complete list of the spectra used in the Doppler analysis is summarized in Table 5.1, including observational date, UT time of the beginning of the observation, exposure time, heliocentric Julian date of the center of the observation interval, wavelength range, and spectral state. Orbital phase is also indicated, the ephemeris of the inferior conjunction of the companion star is adopted from Gies et al. (2003),

$$2451730.449 + 5.599829E .$$

Table 5.1: The list of spectra used for the Doppler tomography

Date (yyyy/mm/dd)	UT start (hh:mm:ss)	Exposure time (s)	Heliocentric Julian date	Wavelength range (\AA)	Orbital phase	Spectral state*
2003/04/01	03:27:09	2000	2452730.6420	6257-6769	0.613	LH
2003/04/17	02:14:28	3466	2452746.5924	6258-6770	0.463	LH
2003/07/14	21:55:29	4000	2452835.4167	6258-6771	0.326	HS
2003/07/20	23:39:47	3600	2452841.4893	6258-6771	0.231	HS
2003/07/25	23:16:59	3600	2452846.4735	6258-6771	0.300	HS
2003/08/05	22:28:34	600	2452857.4399	6258-6771	0.255	I
2003/08/05	22:43:14	3600	2452857.4501	6258-6771	0.260	I
2003/08/08	23:54:02	1800	2452860.4993	6259-6771	0.624	I
2003/08/09	00:30:30	1800	2452860.5246	6259-6771	0.807	I
2003/08/09	01:04:10	1800	2452860.5480	6259-6771	0.811	I
2003/08/10	00:21:41	3600	2452861.5185	6258-6771	0.987	LH
2003/08/11	01:01:03	300	2452862.5458	6259-6771	0.167	LH
2003/08/11	01:08:55	3600	2452862.5513	6259-6771	0.171	LH
2003/08/22	22:59:45	1800	2452874.4614	6259-6772	0.296	I
2003/08/22	23:32:08	1800	2452874.4839	6259-6772	0.300	I
2003/08/23	00:03:43	1800	2452874.5059	6259-6772	0.304	I
2003/08/23	00:34:51	1800	2452874.5275	6259-6772	0.308	I
2003/08/24	20:20:45	1800	2452876.3510	6259-6772	0.632	I
2003/08/24	20:54:48	1800	2452876.3746	6259-6772	0.636	I
2003/08/24	21:27:09	1800	2452876.3971	6259-6772	0.640	I
2003/08/24	22:01:29	1800	2452876.4209	6259-6772	0.644	I
2003/08/25	01:26:12	1800	2452876.5631	6259-6772	0.669	I

Date (yyyy/mm/dd)	UT start (hh:mm:ss)	Exposure time (s)	Heliocentric Julian date	Wavelength range (Å)	Orbital phase	Spectral state*
2003/08/25	02:04:27	1800	2452876.5897	6259-6772	0.674	I
2003/08/26	21:52:08	400	2452878.4144	6259-6772	0.000	LH
2003/08/26	22:02:47	3300	2452878.4218	6259-6772	0.005	LH
2003/09/15	22:33:24	4000	2452898.4425	6258-6770	0.581	LH
2003/09/16	22:20:30	3600	2452899.4335	6258-6770	0.754	LH
2003/09/18	19:57:43	4000	2452901.3343	6261-6773	0.097	LH
2003/09/20	22:13:42	1200	2452903.4286	6259-6772	0.468	LH
2003/09/20	22:37:49	5175	2452903.4454	6259-6772	0.475	LH
2003/09/21	22:41:52	5499	2452904.4481	6259-6771	0.655	LH
2003/09/24	23:19:04	300	2452907.4756	6258-6770	0.190	LH
2003/09/24	23:26:23	3600	2452907.4998	6258-6770	0.194	LH
2003/09/25	23:44:19	180	2452908.4924	6258-6770	0.371	LH
2003/09/25	23:49:54	3077	2452908.5130	6258-6770	0.375	LH
2004/04/12	00:33:19	7200	2453107.5636	6257-6769	0.921	LH
2004/06/21**	14:46:04	900	2453270.1205	6338-6718	0.949	HS
2004/06/21**	15:01:51	900	2453270.1315	6338-6718	0.951	HS
2004/06/22**	14:36:11	900	2453271.1137	6337-6811	0.126	HS
2004/08/09	00:20:20	6300	2453226.5540	6264-6776	0.170	LH
2004/08/24	22:46:10	300	2453242.4537	6263-6776	0.009	LH
2004/08/24	22:54:29	3600	2453242.4786	6263-6776	0.013	LH
2004/09/02	20:13:36	300	2453251.3475	6263-6776	0.597	LH
2004/09/02	20:24:29	1800	2453251.3638	6263-6776	0.600	LH
2004/09/25**	13:47:11	1000	2453274.0802	6338-6738	0.656	HS
2004/09/25**	14:04:44	1000	2453274.0924	6338-6738	0.658	HS
2004/09/26**	13:23:08	1000	2453275.0635	6340-6700	0.831	HS
2004/09/26**	13:40:42	1000	2453275.0757	6340-6700	0.834	HS
2004/10/24	19:01:57	300	2453303.2954	6266-6779	0.874	I
2004/10/24	19:12:04	1800	2453303.3112	6266-6779	0.877	I
2004/11/24	16:50:00	300	2453334.2020	6264-6776	0.393	I
2004/11/24	16:57:04	2400	2453334.2191	6264-6776	0.396	I
2006/09/26**	13:55:43	1200	2454005.0873	6339-6777	0.196	LH
2006/09/26**	14:17:18	1200	2454005.1023	6339-6777	0.199	LH
2006/09/27**	13:16:20	1200	2454006.0600	6339-6777	0.370	LH
2006/09/27**	13:55:07	1200	2454006.0869	6339-6777	0.375	LH
2006/09/28**	12:14:02	1200	2454007.0167	6339-6866	0.541	LH
2006/09/28**	13:15:46	1200	2454007.0596	6340-6867	0.549	LH
2006/09/29**	12:19:54	1200	2454008.0138	6338-6787	0.720	LH
2006/10/01**	11:59:59	600	2454010.0035	6335-6798	0.075	LH
2006/10/01**	15:04:09	600	2454010.1314	6334-6797	0.098	LH
2006/10/02**	12:04:59	600	2454011.0069	6333-6797	0.254	LH
2006/10/02**	14:30:00	600	2454011.1076	6332-6796	0.272	LH
2007/07/06	22:49:27	3600	2454288.4748	6257-6769	0.804	LH
2008/04/24	21:24:46	7200	2454581.4334	6251-6764	0.120	LH
2008/05/06	20:53:11	7200	2454593.4121	6251-6764	0.259	LH
2008/05/07	00:28:20	7200	2454593.5615	6251-6764	0.286	LH
2008/06/02	23:48:45	7200	2454620.5355	6249-6762	0.103	LH
2008/09/09	21:36:53	8000	2454719.4497	6252-6765	0.766	LH
2009/08/14	22:07:44	3600	2455058.4462	6253-6765	0.303	LH
2010/04/27	00:53:04	2600	2455313.5515	6261-6774	0.859	LH
2010/09/17	20:53:54	4200	2455457.3976	6256-6768	0.547	HS
2010/10/08	19:07:35	3600	2455478.3194	6255-6767	0.283	HS

Date (yyyy/mm/dd)	UT start (hh:mm:ss)	Exposure time (s)	Heliocentric Julian date	Wavelength range (Å)	Orbital phase	Spectral state*
2011/05/05	20:52:34	1836	2455687.3805	6252-6765	0.616	LH
2011/10/21	18:45:58	1800	2455856.2932	6252-6764	0.780	HS
2011/10/21	19:19:18	1800	2455856.3164	6252-6764	0.784	HS
2011/10/21	21:30:30	1800	2455856.4075	6252-6764	0.801	HS
2011/10/21	22:03:19	1800	2455856.4303	6252-6764	0.805	HS
2011/10/22	21:59:24	1800	2455857.4275	6251-6763	0.983	HS
2011/10/22	22:32:19	1500	2455857.4486	6251-6763	0.987	HS
2011/11/12	16:25:29	1800	2455878.1944	6252-6764	0.691	HS
2011/11/12	19:06:26	1800	2455878.3062	6252-6764	0.711	HS
2011/11/13	17:51:39	1800	2455879.2542	6252-6765	0.881	HS
2011/11/13	19:40:10	1800	2455879.3295	6252-6765	0.894	HS
2011/12/10	16:56:27	1800	2455906.2144	6252-6765	0.695	LH
2012/08/20	22:21:20	1031	2456160.4408	6253-6766	0.094	HS
2012/08/27	18:58:18	4500	2456167.3197	6253-6766	0.322	HS
2013/07/17	00:47:50	1801	2456490.5469	6263-6736	0.043	HS
2013/07/18	20:52:57	2001	2456492.3850	6263-6736	0.372	HS
2013/07/19	01:55:16	1394	2456492.5914	6263-6736	0.408	HS
2013/08/16	22:35:10	3001	2456521.4618	6262-6735	0.564	HS
2013/08/17	23:15:07	3001	2456522.4895	6262-6735	0.748	HS
2013/08/22	23:48:31	3001	2456527.5127	6262-6735	0.645	HS
2013/08/23	21:20:18	6203	2456528.4283	6262-6735	0.808	HS
2013/08/24	19:00:15	5256	2456529.3255	6262-6734	0.968	HS
2013/08/28	22:16:02	2307	2456533.4443	6262-6734	0.704	HS
2013/08/29	22:53:50	3001	2456534.4746	6262-6734	0.888	HS
2013/09/04	23:07:07	3001	2456540.4836	6262-6734	0.961	HS
2013/09/09	20:52:24	2701	2456545.3882	6262-6734	0.837	HS
2013/09/27	20:17:04	8991	2456563.3993	6262-6735	0.053	HS
2013/09/29	21:34:03	2501	2456565.4151	6262-6735	0.413	HS
2013/09/30	21:40:51	3601	2456566.4262	6262-6734	0.594	HS
2013/10/06	20:30:59	6282	2456572.3929	6262-6734	0.659	HS
2013/10/07	22:23:27	5114	2456573.4642	6262-6734	0.850	HS
2013/10/08	18:55:12	2968	2456574.3071	6262-6735	0.001	HS
2013/10/19	20:23:17	4037	2456585.3739	6262-6735	0.977	HS
2013/10/31	20:43:25	3795	2456597.3858	6262-6735	0.122	HS

* Low/Hard state (LH), High/Soft state (HS) and Intermediate state (I)

** spectra observed at the Xinglong station (China)

The observation were reduced using standard reduction routines in IRAF. All spectra were bias-subtracted, flat-field corrected, and had cosmic rays removed. After cleaning and wavelength calibration, the spectra were converted to ASCII format to be further processed in MOLLY, a one-dimensional spectrum analysis program developed by Tom Marsh. In MOLLY, the spectra were corrected for the heliocentric effects, and normalized by fitting polynomials. This process was followed by subtraction of these polynomials from the corresponding spectra.

An example of optical spectra of HDE 226868 is displayed in Fig. 5.6. The most prominent feature in the observed spectral range is variable H α line. Its profile strongly depends on orbital phase and spectral state. It is apparent from the observations that the spectra taken in the Low/Hard state have a strong emission in

the whole H α line profile, while in the High/Soft state period, the emission remains only in the long-wavelength wing of the line and the short-wavelength side of the line profiles reveals an absorption, as is typical for the P-Cygni profiles of stars with intense mass-loss via a stellar wind.

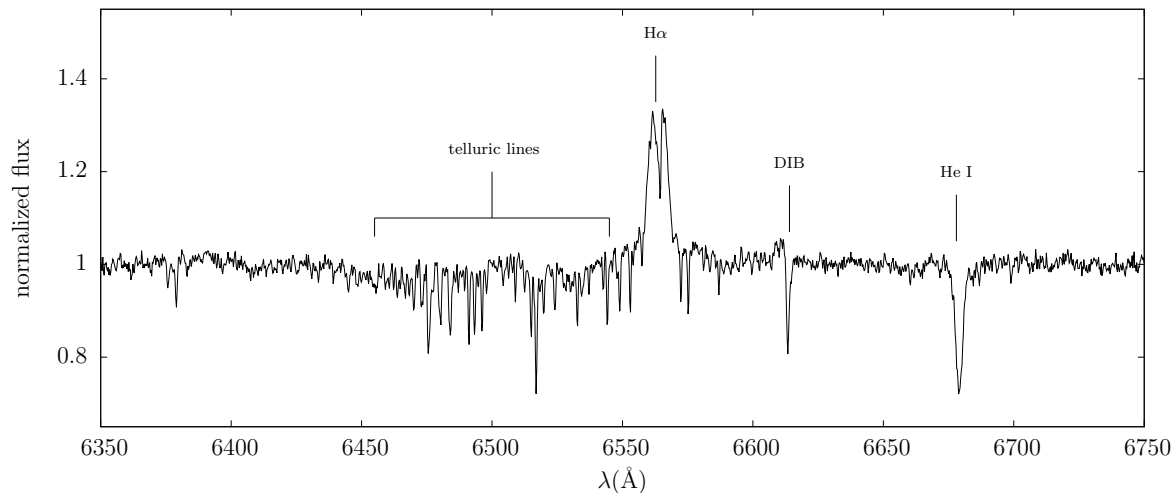


Figure 5.6: Example of normalized spectra of HDE 226868 taken by Ondřejov telescope on June 2, 2008. The main spectral features are indicated, including H α line, He I λ 6678, DIB λ 6614 and contamination by telluric lines.

The He I λ 6678 line is practically free of emission in both states. It means that this line may enable us to reliably measure radial velocities of the primary component to get a constraint on the orbital parameters of the system (Hadrava 1995, 1997, 2004).

One of the pronounced spectral features is the absorption at $\lambda = 6614 \text{ \AA}$. It is actually an example of a diffuse interstellar band (DIB) in our spectra. The carrier molecule of these interstellar absorption bands is still unknown (Herbig 1995; Krelowski 2003). The identification of the carriers of these bands remains an important problem in astronomy to date, and the current consensus on the nature of the carriers is that they are probably carbon-bearing molecules that resides ubiquitously in the interstellar gas (Ehrenfreund & Charnley 2000). The most promising carrier candidates are carbon chains, polycyclic aromatic hydrocarbons (PAHs), and fullerenes (Salama et al. 1996, 1999; Foing & Ehrenfreund 1994; Schulz et al. 2000; Motylewski et al. 2000). The DIB at $\lambda = 6614 \text{ \AA}$ has a finer structure consisting of 3 absorption lines (Galazutdinov et al. 2002) which are, however, below the resolving power of our instruments. Since DIBs do not follow the orbital motion of the binary, we use them to increase accuracy in wavelength scaling. For this purpose, we calculated radial velocities (RVs) of the systemic shifts for each spectra using KOREL, a code employing a method of Fourier disentangling of spectra of binary and multiple stars – cf. e.g., Hadrava (2009a,b).

The spectra are of good quality in terms of spectral resolution which makes them suitable for Doppler tomography. However, in the terms of time coverage, things get more complicated. In order to satisfy one of the assumption of Doppler

tomography that distribution of emission from the system is constant throughout the time of an observation, we should only use spectra taken during a short period of time - typically a couple of orbital periods. Cygnus X-1 has orbital period of 5.6 days which provides us with roughly a month long window of opportunity where all the observations should be made so we can still claim that the distribution of the circumstellar matter remains roughly the same. But with two exceptions of observational series in 2003 and 2013, most of our data are scattered throughout a period of almost a decade. Because of this difficulty, we balance the need for the optimal orbital phase coverage while trying to minimize the observation interval. In order to solve this problem, we assume that the general characteristics of the stellar wind distribution is specified by the particular spectral state. Although we expect short time variations in emission, most likely to be caused by a turbulent motion of gas, we suppose that the fundamental distribution of emission remains stable and unique for a particular spectral state. This assumption allows us to divide all observations in group according to their spectral state. This provides us with sufficient orbital phase coverage to perform reliable Doppler analysis. In the cases of the observational series in 2003 and 2013, we gathered, in the period of several months, enough spectra for the independent Doppler analysis. Even though the orbital phase coverage is not optimal, we can still make some general conclusions and compare the results with the tomograms obtained from the whole period 2003–2013.

5.6.1 Determination of X-ray state of Cygnus X-1

To determine the X-ray spectral state of Cygnus X-1 we need to use an X-ray observational data. In the past decade, state information was readily available using the All Sky Monitor on the Rossi X-ray Timing Explorer (RXTE-ASM) and regular pointed monitoring observations. Unfortunately, RXTE ceased science operation on January 5, 2012 (MJD 55931) but even prior to this date since January 2010, ASM experienced an instrumental decline which had made all the observed data unsuitable for the spectral state determination. In order to determine spectral state corresponding to our optical observations we had to combine X-ray data from multiple sources. Here, various state definitions exist, which use, e.g., measured count rates and/or color – cf., e.g., Remillard (2005a); Gies et al. (2008), or sophisticated mapping between these measurements and spectral parameters – cf., e.g., Ibragimov et al. (2007); Zdziarski et al. (2011). The former prescription is easy to use, but is very instrument specific and cannot be easily translated to other X-ray all sky monitors. The latter approach requires a sophisticated knowledge of the instrumentation of all sky monitors, as well as of the detailed spectral modelling. Furthermore, the previously used state definitions are slightly inconsistent among themselves. The source behaviour from early 1996 (RXTE lunch) until the end of 2004 has been discussed by Wilms et al. (2006), who used a crude definition of ASM based states using only the count rate. This classification is sufficient to distinguish main activity patterns, and also consistent with more detailed studies (Zdziarski et al. 2011). But in this work, we use a novel approach to classify states of Cygnus X-1 using all sky

monitors RXTE-ASM, MAXI, and *Swift*-BAT based on 16 years of pointed RXTE observations and suggested by Grinberg et al. (2013).

Table 5.2: Overview of X-ray state definitions according to different all sky monitors

State	ASM-based	MAXI-based	BAT-based
Low/Hard	$c \leq 20 \vee c \leq 55(h - h_0)$	$c_M \leq 1.4h_M$...
Intermediate	$c > 20 \wedge 55(h - h_0) < c \leq 350(h - h_0)$	$1.4h_M < c_M \leq 8/3h_M$...
High/Soft	$c > 20 \wedge c > 350(h - h_0)$	$8/3h_M < c_M$	$c_B \leq 0.09$

Notes: ASM 1.5–12 keV count rate c is in counts s^{-1} , and h is ASM hardness defined as (5–12 keV/1.5–3 keV), $h_0 = 0.28$. MAXI 2–4 keV count rate c_M is in counts s^{-1} , and h_M is MAXI hardness defined as (4–10 keV/2–4 keV). BAT normalized 15–50 keV count rate c_B is in counts $\text{cm}^{-2} \text{s}^{-1}$. Distinguishing between hard and intermediate state is not possible from the BAT light curves alone. The source is defined as in BAT-based hard or intermediate state for $c_B > 0.09$ counts $\text{cm}^{-2} \text{s}^{-1}$ (Grinberg et al. 2013).

As mentioned before, the ASM experienced an instrumental decline rendering all data post January 2010 unsuitable for defining the state of Cygnus X-1. Data from 2010–2012 can still be used to assess trends with large changes in count rate; however, for the following analysis, which relies on absolute values of both count rate and hardness, we ignore all ASM data after MJD 55200.

MAXI is an all-sky monitor on board the Japanese module of the International Space Station (Matsuoka et al. 2009). Light curves from the Gas Slit Camera detector (GSC) are available in three energy bands (2–4 keV, 4–10 keV, and 10–20 keV) on a dedicated website¹. MAXI light curves show prolonged gaps of several days due to observational constraints. MAXI coverage started on MJD 55058 (August 15, 2009). No simultaneous coverage with ASM exists during the intermediate and soft states, except during the phase of ASM deterioration.

Swift-BAT is sensitive in the 15–150 keV regime (Barthelmy et al. 2005). Satellite-orbit averaged light curves in the 15–50 keV energy band from this coded mask instrument are available on a dedicated website². BAT coverage started on MJD 53414 (mid-February 2005).

Table 5.2 shows the determination of state based on the data from different all-sky monitors taken from (Grinberg et al. 2013). A graphical representation of determining conditions of particular spectral state can be found in Fig. 5.7. The first two panels show the RXTE-ASM data coloured according to their established spectral states (blue is for the Low/Hard, green for the Intermediate and red for the High/Soft state). The first panel represents the sum of counts in ASM 1.5–12 keV energy range, the second panel shows the hardness of spectra. The hardness is defined as a ratio of count rates in C band (5.0–12 keV) and A band (1.5–3.0 keV). The period of the instrumental deterioration of ASM is indicated by dotted line. All data from RXTE-ASM after January 2010 (grey colour) are excluded from our analysis. The third and fourth panels show the data from MAXI energy band 2–20 keV and *Swift*-BAT energy band 15–50 keV. Black colour represents

¹<http://maxi.riken.jp/top/index.php?cid=1&jname=J1958+352>

²<http://swift.gsfc.nasa.gov/results/transients/>

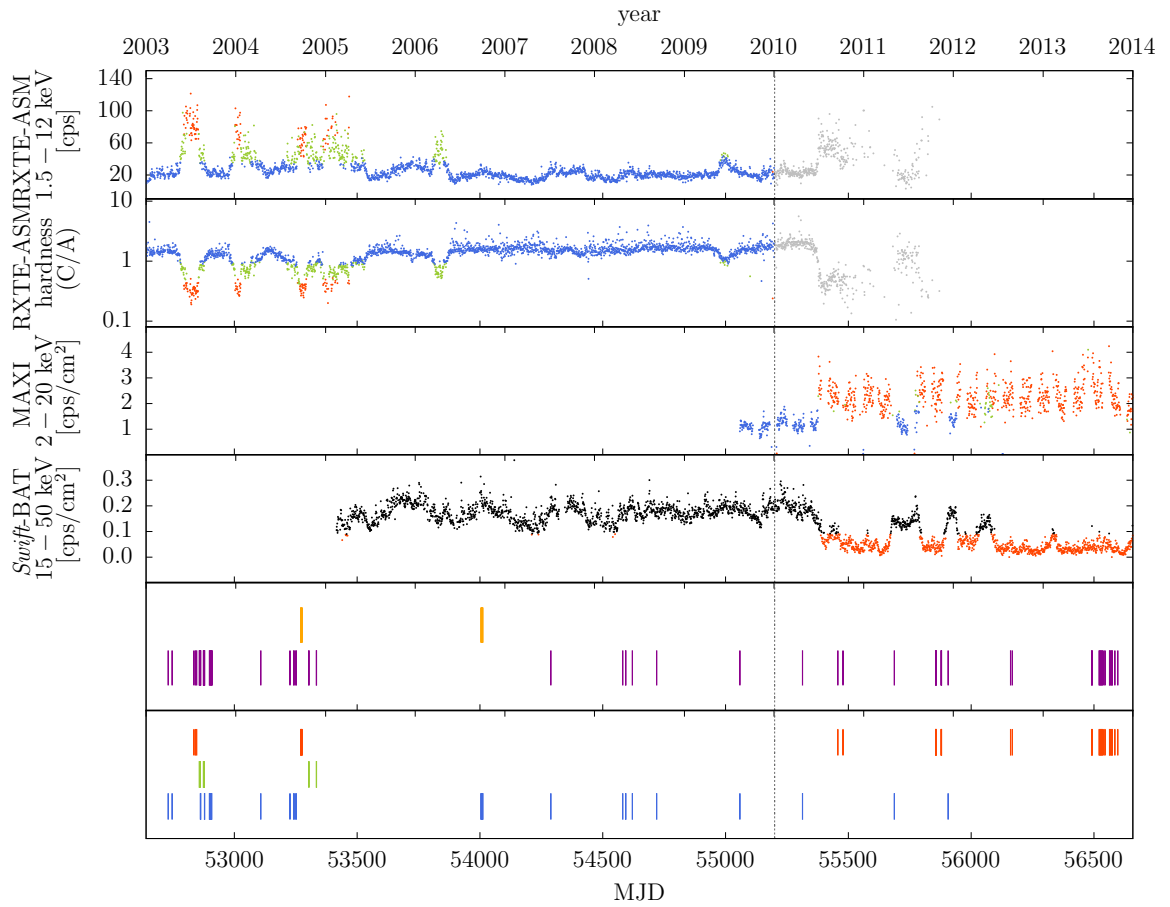


Figure 5.7: X-ray light curves (RXTE-ASM, MAXI, and *Swift*-BAT) of Cygnus X-1 in the highest available resolution. ASM hardness is calculated by dividing count rates in *C* band (5.0–12 keV) by count rates in *A* band (1.5–3.0 keV). Vertical dotted line represents starting point of instrumental decline of ASM. Blue, green and red colors represent X-ray spectral states of individual measurements classified by respective classification for the given instruments as described in Table 5.2: blue represents the Low/Hard, green the Intermediate state, and red the High/Soft state. ASM data after MJD 55200 (shown in gray) are affected by instrumental decline. The Low/Hard and Intermediate states cannot be distinguished in BAT, data corresponding to these periods of the Low/Hard or Intermediate state are therefore shown in black. The second bottom most panel shows distribution of the available optical spectra from Ondřejov (magenta) and Xinglong (orange). The last panel divides the spectra into groups according to the spectral state.

the Low/Hard and Intermediate state which are indistinguishable from the *Swift*-BAT data alone. The second panel from the bottom displays the distribution of optical spectra available for our analysis. The Ondřejov spectra are shown in magenta while the Xinglong data from 2004 and 2006 are shown in orange. From this, we can notice how scattered the data are. The best series we have available are 2003 with 35 spectra and 2013 with 20 spectra. In the bottom-most panel, we show the distribution of all optical spectra between 2003 and 2013 altogether with their corresponding spectral states. The colours of the spectra are consistent with the

colours used to describe the spectral state in the above panels.

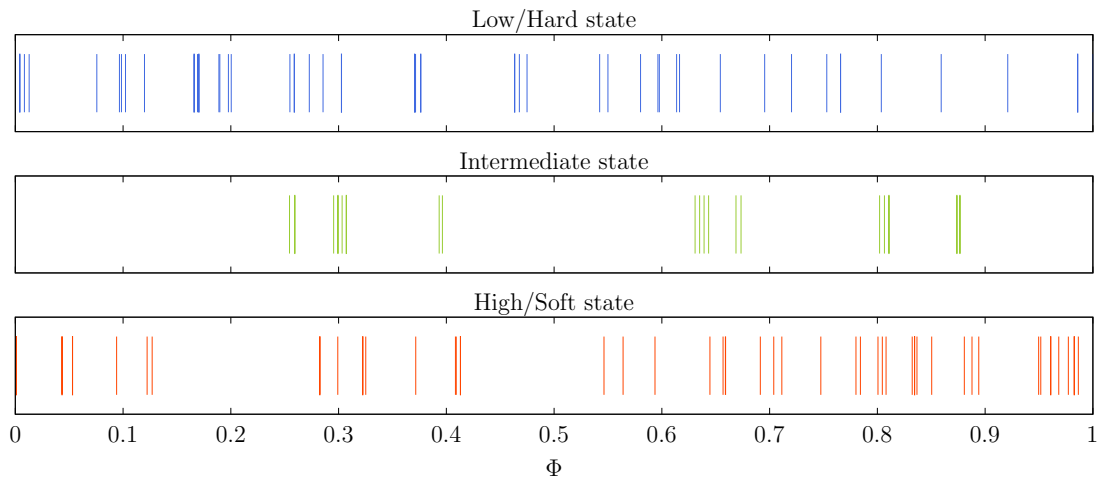


Figure 5.8: Distribution of the optical spectra of HDE 226868 in orbital phase corresponding to different X-ray states. The Low/Hard state in blue (44 spectra), the Intermediate state in green (19 spectra), and the High/Soft state in red (44 spectra).

Based on our X-ray data analysis, we were able to divide the optical spectra into groups according to their corresponding X-ray state. In Fig. 5.8, we show distribution of optical spectra from Ondřejov and Xinglong in orbital phase of Cygnus X-1 with respect to their corresponding X-ray states. We assigned 44 spectra to the Low/Hard state, 19 spectra to the Intermediate state, and 44 remaining spectra to the High/Soft state. With these numbers, we should be able to get sufficient phase coverage with the exception of the Intermediate state. Unfortunately, most of the spectra are clustered together (we have two expositions in many observation nights leading to almost identical orbital phase of these measurements) so the effective orbital phase coverage is worse than in completely random distribution. Despite the clustering problem, the orbital coverage is, again with the exception of the Intermediate state, quite homogeneous and allows us to use the data for the Doppler analysis.

Fig. 5.9 shows the evolution of the main spectral features of HDE 226868 over orbital period. The left panel shows selected optical spectra from 2003 that correspond to the Low/Hard state of Cygnus X-1. The corresponding observation dates and orbital phases calculated according to the above given ephemeris are written on the left and right side of each spectrum, respectively. Upon close examination, the trailed spectra in $H\alpha$ were found to consist of two superimposed components, shifted in orbital phase. The first component corresponds to a P-Cygni profile of an expanding stellar wind coming from the donor star. The second component is consistent with a presence of strongly variable circumstellar matter in the system. In the right panel, we show the spectra obtained in 2013. All of them are appropriate to the High/Soft state. We only see the P-Cygni component varying with the orbital movement of the donor. There are no traces of the companion or the circumstellar matter in the He I $\lambda 6678$ in either spectral state.

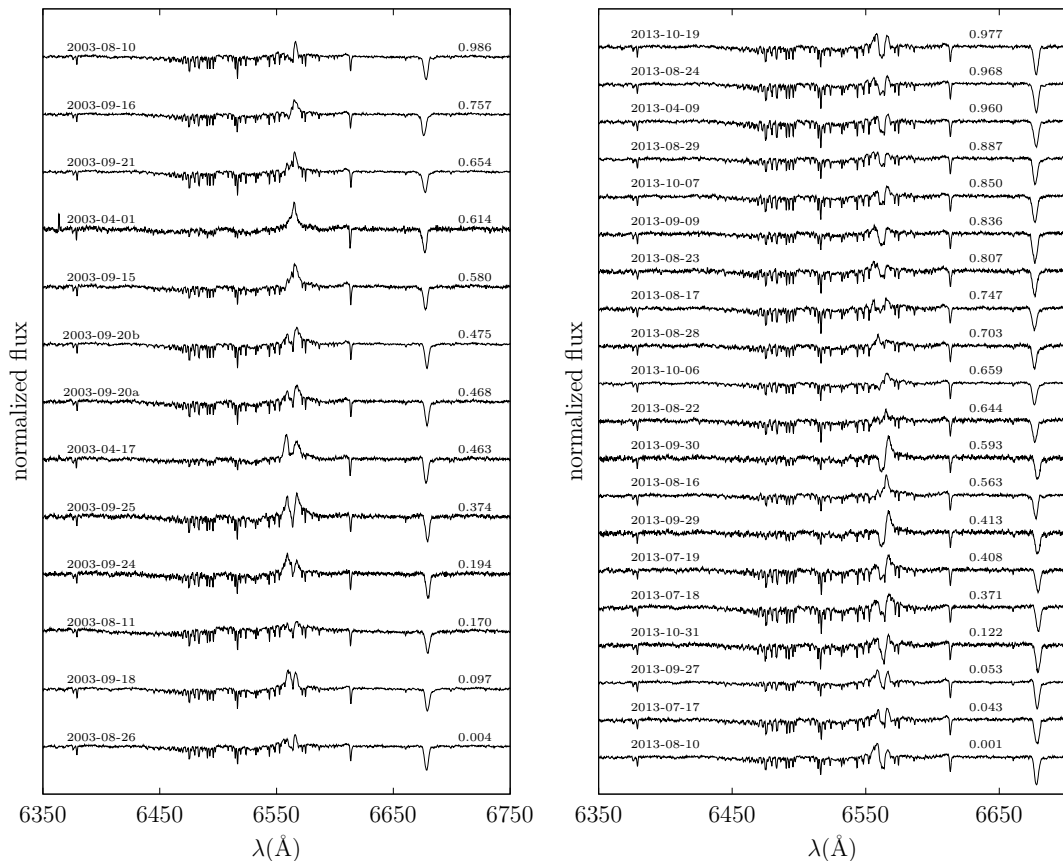


Figure 5.9: Optical spectra showing the orbital phase evolution of the major spectral features – H α line and He I λ 6678. The observation dates and orbital phases are given in the left and right sides of each spectrum, respectively. The left panel shows the selected spectra corresponding to the Low/Hard state in 2003. The right panel represents the High/Soft state in 2013.

5.6.2 The Low/Hard state

To analyse our optical spectra, we use MODMAP – a program for modulated Doppler tomography introduced and developed by Steeghs (2003). The Doppler tomograms we present were created using MEM. A grid of pixels spanning velocity space is adjusted to achieve a target goodness of fit measured with χ^2 , while simultaneously maximizing the entropy of the image. A refined form of entropy which measures departure from a default image is used. For an excellent summary of the method, see Marsh (2001).

For the Doppler tomography of Cygnus X-1, we used the systemic radial velocity $\gamma = -2.7 \text{ km s}^{-1}$, published by Gontcharov (2006). The systemic velocity needs to be known in order to calculate the correct radial velocity curve of a line source with velocity (v_x, v_y) . If one attempts to reconstruct a data set with an incorrect γ , it will be difficult to achieve a good fit to the data since MODMAP is not tracing the correct velocity curves – cf. Marsh & Horne (1988).

We adopt the orbital period $P_{\text{orb}} = 5.599829 \pm 0.000016$ days calculated by

Brocksopp et al. (1999). A high precision in the determination of orbital period is needed since we attempt to analyse the phase resolved data spanning over a decade. If the period is not sufficiently well determined, the tomography will fail completely. Less severe consequences would have an incorrect determination of zero point ephemeris. In this case, the resulted tomogram would be inaccurately positioned. The mass donor star and the compact companion would be rotated by an unknown angle in respect to the emission.

Based on our X-ray analysis in the previous Subsection, we have divided the optical spectra according to their appropriate X-ray state. Here, we present the results of the Doppler tomography of $H\alpha$ $\lambda 6562.76$ for the Low/Hard state of Cygnus X-1. First, we conduct the analysis on the entire ensemble of 44 spectra corresponding to the Low/Hard state, we have available. Then, we run the analysis on 2003 data only (17 spectra in total) to assess the influence of length of the spectra-gathering period on the quality of the result. The orbital coverage of the 2003 data is displayed in Fig. 5.10. The distribution of spectra across the orbital phase is not optimal, showing two large gaps around $\Phi = 0.29$ and 0.86 but we still should be able to get reasonable results showing the distribution of emission in the velocity space.

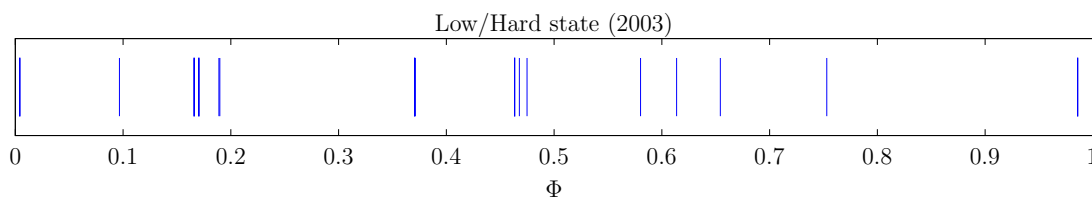


Figure 5.10: Distribution of 17 optical spectra of HDE 226868 in the orbital phase corresponding to the Low/Hard state in 2003.

The Doppler tomograms of $H\alpha$ $\lambda 6562.76$ are shown in Fig. 5.11 and 5.12. The top panels show the input trailed spectra (on the left) and reproduced trail from the fitted emission distribution (on the right) used to evaluate the goodness of the fit. The four maps in the remaining panels correspond, starting top-left and moving in clockwise fashion; the recovered Doppler image of the average emission from the system, the total modulated emission, the sine amplitude map and the cosine amplitude map of the modulated emission. The spectra in Fig. 5.11 from the period 2003–2013 were binned to the orbital phase. 20 bins were used in total, with only 19 of them were filled. The bin 0.4–0.45 had no appropriate data in it, hence, it remains white. The Doppler tomogram in Fig. 5.12 using data from 2003 only, was produced with spectra divided in 8 phase bins - all of them were filled.

We see that the reconstructed trail in Fig. 5.11 and 5.12 reproduces the original data well in both cases. Poorer orbital phase resolution in the case the spectra from 2003 is obviously given by the highly limited spectra available in this period. The basic structure of the trail, however, remains clear and comparable to the trail constructed from the spectra from the entire observation period 2003–2013. The reconstructed Doppler images in both figures display, similarly, the same general structure. We notice a conspicuous emission spot near the position of the donor star depicted via its critical Roche lobe. The two transferring trajectories described

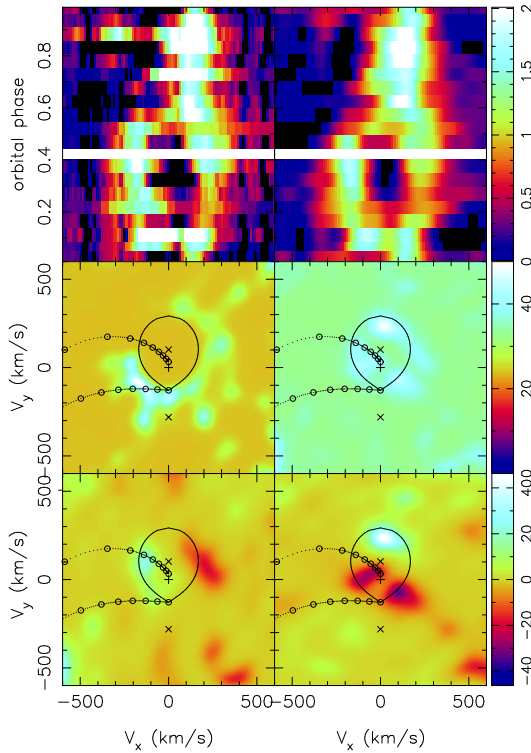


Figure 5.11: Doppler tomogram of $H\alpha$ $\lambda 6562.76$ line produced using all spectra from the period 2003–2013 appropriate to the Low/Hard state of Cygnus X-1. The spectra were divided into 20 phase bins. The figure shows the trailed spectra on top-left panel, the simulated trail on the top-right panel, the distribution of emission in the system in velocity space on the middle-left panel, and the variations of the emission on the middle-right panel. The bottom panels represents the cosine (on the left) and sine (on the right) amplitude maps.

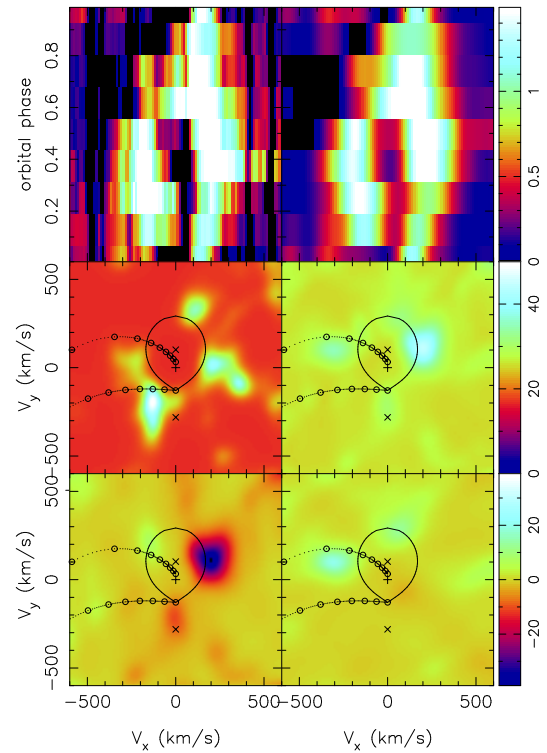


Figure 5.12: Doppler tomogram of $H\alpha$ $\lambda 6562.76$ line produced using spectra from 2003 only appropriate to the Low/Hard state of Cygnus X-1. The spectra were divided into 8 phase bins.

in the Subsection 5.5.1 are also displayed along with the position of the compact companion which is marked with the 'x' cross. The barycentre of the system is shown by '+' cross.

5.6.3 The High/Soft state

Similarly to the previous Section, we will now analyse the spectra appropriate to the High/Soft state of Cygnus X-1. First, we apply the Doppler mapping on the entire ensemble of 44 spectra taken in 2003–2013. Then, we run the analysis on 2013 data only when we gathered 20 spectra in four months period. The orbital coverage of the 2013 data is shown in Fig. 5.13. In this case, the situation is somewhat better

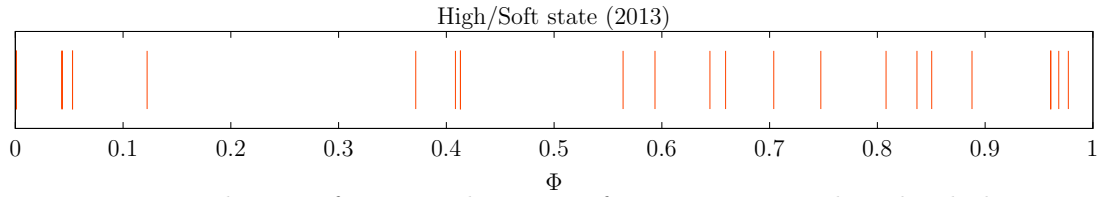


Figure 5.13: Distribution of 20 optical spectra of HDE 226868 in the orbital phase corresponding to the High/Soft state in 2013.

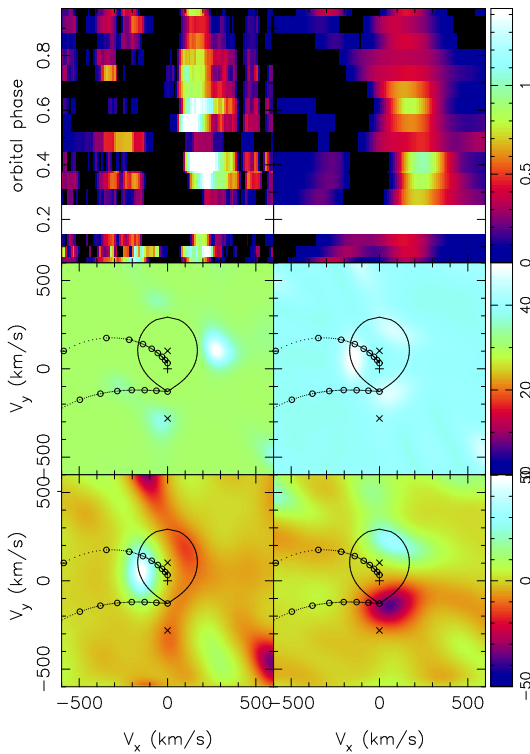


Figure 5.14: Doppler tomogram of H α λ 6562.76 line produced using all spectra from the period 2003–2013 appropriate to the High/Soft state of Cygnus X-1. The spectra were divided into 17 phase bins.

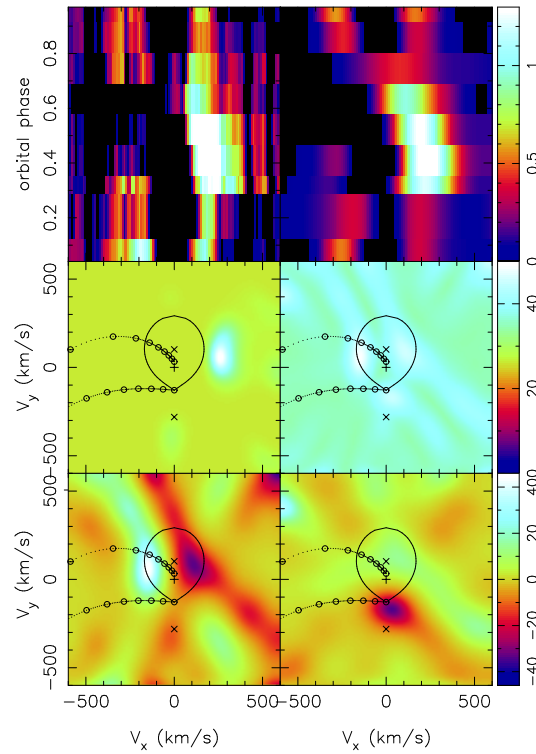


Figure 5.15: Doppler tomogram of H α λ 6562.76 line produced using spectra from 2013 when Cygnus X-1 was in the High/Soft state. The spectra were divided into 9 phase bins.

in comparison to the Low/Hard state in 2013. The data, however, also display a couple of large gaps with the most prominent being centred around $\Phi = 0.25$ and 0.5 .

The results of the Doppler mapping of H α line are shown in Fig. 5.14 and 5.15 for the data covering 2003–2013 period and the 2013 data only, respectively. The meaning of the all panels remain the same as in the previous case – with the top panels showing the input and reproduced trailed spectra and the bottom maps, in the clockwise fashion, showing the recovered Doppler image of the average emission from the system, the total modulated emission, the sine amplitude map and the cosine amplitude map. The spectra in Fig. 5.14 were binned to 17 orbital phase

bins, with 16 of them filled and one remained empty. The smaller number of bins is caused with the less ideal orbital phase distribution of the observed data. The Doppler tomogram in Fig. 5.15 uses the 2013 data only, was produced with spectra decided in 9 phase bins – all of them were filled.

The reconstruction of trail in Fig. 5.14 and 5.15 is somewhat poorer than in the previous case. This is mainly caused by the larger gaps in the phase distribution of the data and, by extension, by the need of having larger phase bins. Another feature worsening the situation is the complex structure of the H α line trail. All these effects complicate the Doppler analysis leaving the results less reliable. In general, the H α emission is less pronounced than in the Low/Hard state. But we still notice a number of bright spots in the emission distribution map. These can be remnants of a disk-like structure around the donor star which would correspond to the P-Cygni profile coming from the expanding stellar wind. But at least some of them are more likely to be numerical artefacts. Despite the poorer coverage and generally worse quality of produced tomograms, we can conclude that the emission representing the gas stream from the donor star towards the compact companion disappeared showing substantial redistribution of the circumstellar material during the transition between individual spectral states.

5.7 Production of synthetic Doppler tomograms

In theory, it is simple enough to convert the velocity coordinates into position coordinates. The only thing that is required is a specification of the velocity at every point in the system. However, there are two complications. First, the transformation between velocity and position is often not known. In fact, it is rarely known, given that it is likely that deviations from Keplerian flow occur. This means that position maps would require re-computation each time system parameters were updated. Second, the same place in the system can produce emission at more than one velocity. This ambiguity is a very real possibility, it happens in nearly every system that has been processed by Doppler imaging. There are many examples of bright-spot emission from the gas stream while the disk at the same location produces emission at a completely different velocity coordinates. If such data is imaged into position coordinates on the basis of Keplerian rotation, a spot of emission would be produced at a spurious location in the disk. These interpretation difficulties can be potentially resolved only in eclipsing binaries.

While it is not trivial to convert the observational data into position coordinates, there is no difficulty in translating predictions of any theoretical model into velocity space. Ideally, the model-observation comparison should be made by predicting trailed spectra, abandoning the Doppler maps altogether. However, Doppler maps still play a role in those theoretical models that are unable to include all peculiarities of real systems, and, thus, the comparison is easier in velocity coordinates. The way, we should think of Doppler maps is to try to imagine where various parcels of gas would appear in velocity space, rather than try to transform features of maps from velocity to position coordinates.

We use our model predictions for the matter distribution in vicinity of Cygnus

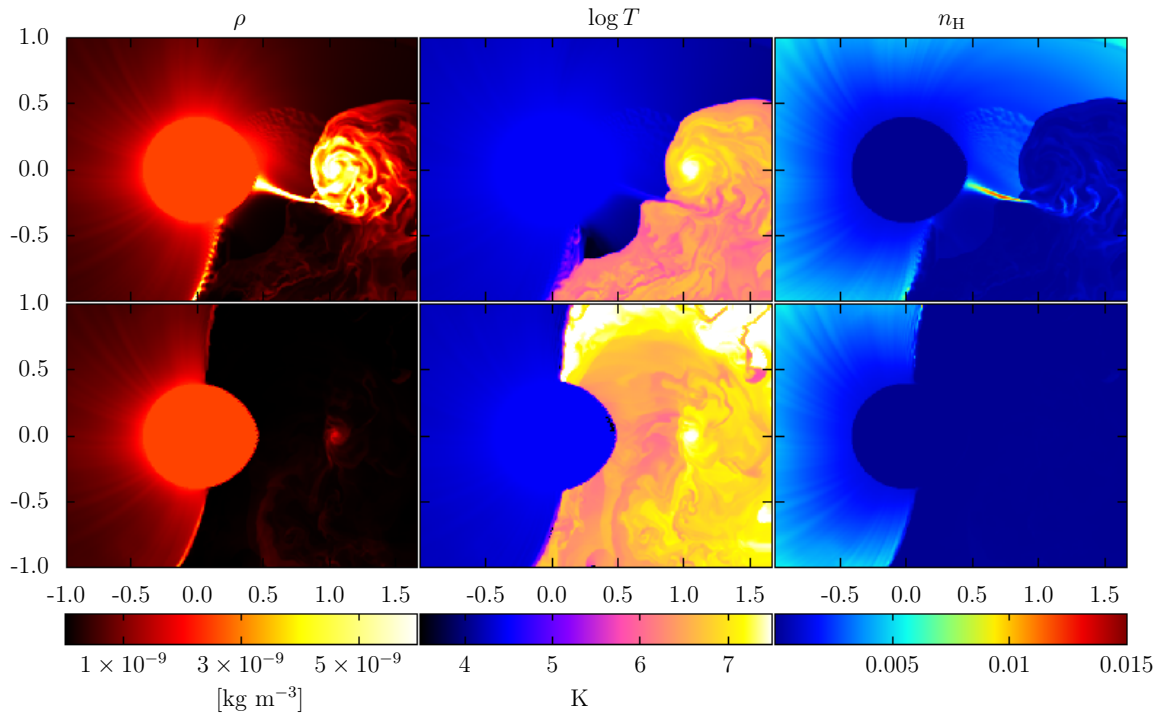


Figure 5.16: Simulated distributions of physical quantities in the equatorial plane of Cygnus X-1 in the Low/Hard (top panels) and High/Soft states (bottom panels). The displayed quantities are the density distribution, local temperature, and the amount of neutral hydrogen.

X-1 to compute a synthetic Doppler tomogram. From Fig. 4.4 (top panels), we can expect that the Doppler maps of Cygnus X-1 in the Low/Hard state will show presence of features corresponding to the gas stream and also the extensive accretion disk. Such a disk would manifest itself as a ring-like structure around the position of the compact companion. But we see no signs of the accretion disk present in the spectra of HDE 226868 (Fig. 5.11 and 5.12). In the High/Soft state (Fig. 4.4 - bottom panels), we expect that the increased X-ray emission from the compact companion cuts off the gas stream supplying the accretion disk which becomes much less pronounced and possibly not visible at all in $H\alpha$ line.

To appreciate the conditions within the circumstellar medium in different spectral states, it is convenient to display, along with the quantities we saw earlier in Fig. 4.4, also local temperature. Fig. 5.16 shows a situation practically identical to one displayed in Fig. 4.4 (even though we let the model to evolve for approximately $0.5 P_{\text{orb}}$). The displayed quantities here are density distribution, local temperature and an amount of neutral hydrogen n_{H} . We define as a ratio

$$n_{\text{H}} = \frac{n(\text{H}^0)}{n_{\text{p}} + n(\text{H}^0)}, \quad (5.2)$$

where $n(\text{H}^0)$ is number density of neutral hydrogen, and n_{p} is proton density. Since $H\alpha$ line is emitted by neutral hydrogen, n_{H} will serve as a tracer of $H\alpha$ line emis-

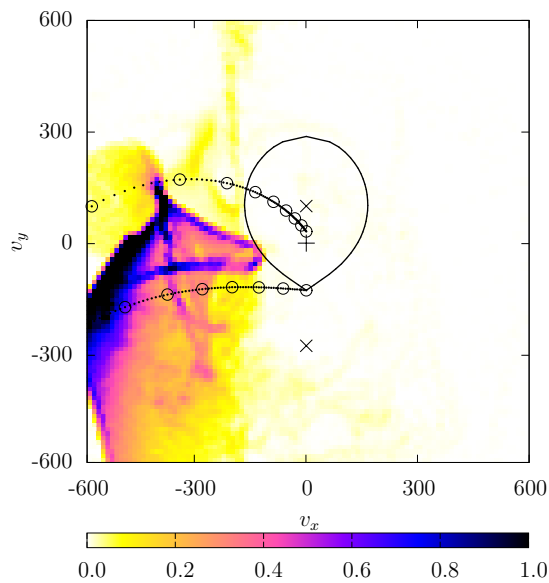


Figure 5.17: Synthetic Doppler tomogram of the predicted distribution of neutral hydrogen produced using model data corresponding to the Low/Hard state of Cygnus X-1 (top panels in Fig. 5.16). The map is directly comparable with the Doppler map acquired from the observational data for HDE 226868 in Fig. 5.11.

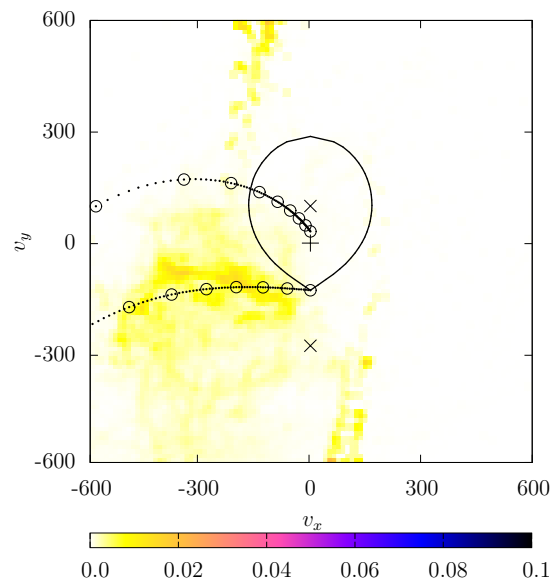


Figure 5.18: Synthetic Doppler tomogram of the predicted distribution of neutral hydrogen produced using model data corresponding to the High/Soft state of Cygnus X-1 (bottom panels in Fig. 5.16). The map is directly comparable with the Doppler map acquired from the observational data for HDE 226868 in Fig. 5.12.

sion. In Fig. 5.16 (top panels), the hydrodynamic shock around the accretion region abruptly increases temperature of the medium to 10^7 K. This temperature is sufficiently high enough to cause hydrogen to be completely ionized due to mutual collisions. The region around the compact companion shows only trace amounts of neutral hydrogen, thus, leaving the gas stream the richest source of $H\alpha$ line emission in the system. The bottom panels show Fig. 5.16 correspond to the High/Soft state. Due to the increased emission of X-ray, the outflow of material from the hemisphere facing the compact companion was interrupted. As a consequence, density in the half-volume around the compact companion was considerably lowered, allowing the hydrodynamic shock to expand. We may notice from Fig. 5.16 that there is no predicted neutral hydrogen in the vicinity of the compact companion.

We can transform the last column in Fig. 5.16 in velocity coordinates in order to create synthetic Doppler maps. The results are shown in Fig. 5.17 and 5.18 for the Low/Hard and High/Soft state, respectively. The color-scale shows a predicted relative flux in $H\alpha$ line. Notice, that there is a factor of 10 difference in the color-scales which was introduced to highlight the weak emission in Fig. 5.18. From direct comparison of Fig. 5.17 and 5.11, we see that the occurrence of the highest concentration of neutral hydrogen in the velocity space roughly coincides with the emission region of $H\alpha$ line determined from the optical observations. As expected, the emission in Fig. 5.18 practically disappeared when we switched the system to

the High/Soft state.

Chapter VI

Conclusion

We have presented our enhanced radiation hydrodynamic model of the stellar wind in HMXBs which we used to simulate the circumstellar environment of Cygnus X-1. First, in a series of two-dimensional simulations we investigated the role of various parameters on the distribution and dynamics of the stellar wind. Then we made use of the capabilities of our code to perform more complex three-dimensional analysis of the problem. We find that the wind parameters and its ionization structure established by the presence of a strong X-ray source, have a significant impact on the structure and dynamics of the stellar wind.

Both two and three-dimensional simulations show the formation of an extensive bow shock enveloping the accretion disk and the compact companion. This cone-like structure is curved by the Coriolis force as it advances out of the computational area but remains roughly axi-symmetric and resembles BHL accretion. The position and orientation of the shock depends on relative velocity of the compact object through the stellar wind, mass of the compact companion, and the X-ray luminosity. On the other hand, the shock is relatively insensitive to the changes in the mean radius of the primary.

The outcomes of the two-dimensional simulations support the importance of the X-ray feedback in HMXBs. The X-ray ionization tends to slow down the wind material in the immediate vicinity of the compact companion and, thus, to increase the overall accretion rate (Hatchett & McCray 1977). However, if the zone of full ionization extends to the proximity of the surface of the donor where the wind does not yet reach the escape velocity, the outflow can be obstructed right at the base of the wind. Hence, leaving the accretion process effectively cut out from the additional material.

We investigated the properties of the stellar wind in Cygnus X-1 in Low/Hard and High/Soft X-ray state and simulated the transition between these two states. The three-dimensional simulation revealed dramatic changes of the outflow of the material from the primary as a response to the increased X-ray luminosity. The dense gas stream in the proximity of L_1 point which resembles the Roche lobe overflow in semi-detached binaries, completely subsided. The increase of the X-ray radiation from the compact companion ionized the base of the wind in the stellar photosphere rendering the line-driven mechanism incapable of accelerating the wind.

The material cannot reach the escape velocity and falls back to the surface of the primary. The duration of the decline of the gas stream ($\sim 0.25 P_{\text{orb}}$) is relatively short and corresponds to the time needed for the gas lurching from the facing hemisphere of the primary to leave the accreting region.

The suppression of the dense gas stream as the system switches from Low/Hard state to High/Soft state is in full agreement with earlier optical observations of Cygnus X-1 (Hadrava & Čechura 2013) where a decomposed spectral line component of $\text{H}\alpha$ corresponding to the circumstellar matter anticorrelates with the soft X-ray emission.

To minimize the cost of the computation, we made several simplifying approximations in our three-dimensional numerical model. Probably the most drastic one was the neglecting of the optical depth effects that would require to solve the radiative transfer in the stellar wind simultaneously with the hydrodynamic calculations. These effects are likely to play a role in the wind dynamics in HMXBs, but the difficulty of realistically calculating the radiative transfer makes the problem beyond the scope of this work.

In addition to the radiation hydrodynamic simulations of the stellar wind in HMXBs, we also performed optical observations and Doppler analysis of the phase-resolved spectroscopic observations of $\text{H}\alpha$ line of Cygnus X-1 in the period of 2003–2013. In order to obtain the best orbital phase coverage possible, we put together the spectra we observed (in part) using the Ondřejov 2-m telescope in the Czech Republic with the spectra taken at the Xinglong station in China. We utilize the X-ray observations from RXTE, MAXI and *Swift*-BAT in order to compartmentalize the optical data according to their X-ray spectral state. The results of our analysis show dramatic redistribution of the circumstellar material in Cygnus X-1 during the transition between the Low/Hard and High/Soft states. In the Low/Hard state, we find an $\text{H}\alpha$ emission that is consistent with a dense matter stream (focused stellar wind) in the proximity of the inner Lagrangian point L_1 launching from the donor star and accreting onto the compact companion. Despite the poorer phase coverage leading to worsened quality of the resulted Doppler maps, we conclude that in the High/Soft state when the X-ray emission from the compact companion is increased, the $\text{H}\alpha$ emission from the matter stream is suppressed. This indicates disruption of the mass transfer between the components of the binary. In the case of the third most prominent X-ray spectral state in Cygnus X-1 – the Intermediate state – we did not acquire a sufficient amount of data which would allow us to carry out the Doppler analysis. Besides the insufficient phase coverage of the optical spectra, we can expect that during this state the distribution of the circumstellar matter is erratic and highly variable. In order to produce a reliable Doppler tomogram in this X-ray state, we would need observation data covering no more than a few orbital periods.

We use the results of our model of Cygnus X-1 to calculate amount of neutral hydrogen in the circumstellar matter which is responsible for generating the $\text{H}\alpha$ line emission. For this distribution, we produce synthetic Doppler tomograms corresponding to both major X-ray states of Cygnus X-1 – the Low/Hard and High/Soft state – and compare them with the tomograms obtained from the spectroscopic anal-

ysis. The comparison of the observational data with the numerical simulations is done in velocity rather than spatial coordinates to avoid the problem with ambiguity. In both X-ray states, we find the predicted distributions of neutral hydrogen to be in good agreement with the observations, thus confirming the underlying assumptions about Cygnus X-1.

Chapter VII

Future perspective

One possible way of advancing the simulation-data comparison method would be obviously to obtain higher quality phase-resolved spectra. An ideal source candidate would be a bright binary system with orbital period of several hours. In such a case, we should be able to obtain a number of spectra with sufficient phase coverage in matter of several consecutive days. As a consequence, precision of determination of the emission distribution in Doppler maps would increase considerably. For this purpose, a low mass X-ray binary with typically hours-long orbital period would be an ideal candidate. However, as we stated in the introduction, low mass main sequence stars do not possess stellar wind intense enough to power accretion process. The accretion in such systems is more likely to be due the Roche lobe overflow, for which our code has not been sufficiently tested yet.

Another way of further advancement of the numerical simulations would be to fully integrate radiative transfer into the hydrodynamic code. This is, however, very complex problem which was, to a limited extent, employed only in the most advanced and highly specialized radiation hydrodynamic codes. Besides other things, the main problem of the integration of the radiative transfer is a considerable increase of already very high demands on computational time. The possible ways to battle this challenge would be, for example, code parallelization, adopting an adaptive mesh refinement of the computational grid, or computing on graphical processing units (GPUs). All these proposed improvements will be subjects of the future development of our code.

A possible future enhancement of the capabilities of the numerical model for HMXBs would be to improve the adopted physical model. For instance, extending the computation of ionization structure of the wind material to other elements than hydrogen would be very beneficial for the further study of the wind structure and properties.

The most important question about the nature of the spectral states of X-ray binaries, however, remains unanswered. We still know little about the switching mechanism itself. The accretion process influences the circumstellar matter to much greater extent than only through the X-ray feedback. We have an evidence of a presence of jet in Cygnus X-1 (Gallo et al. 2005). Such a jet would be generated in the close proximity of the compact companion. Because of the high computational

demands, however, we cannot use fine enough resolution which would allow us to simulate satisfactorily the physical processes in this region. For further advancement in this matter, we have to first improve our model of the accretion disk region taking into account effects of magnetic field and general relativity (Roedig et al. 2012). This general relativistic radiation magnetohydrodynamic approach (GR-MHD) would provide us with more self-consistent model of X-ray binaries.

Despite the need for the further improvement of the radiation hydrodynamic code, it has already proven to be a very useful tool with a broad range of applications far exceeding simulations of the stellar wind in HMXBs. We used our code to simulate the circumstellar environment around a very orderly arranged model system – with circular orbit and with the donor star in tidally locked rotation. In wider range of applications, the radiation hydrodynamic model could be use for example to calculate the structure and dynamics of gas in systems with high eccentricity. This could lead to a better understanding of the enhanced stellar wind accretion model for X-ray binary transients (Avni & Goldman 1980; Boyle & Walker 1986; Stevens 1988; Kumar et al. 1995) and to increase our ability to interpret observational data (Mavromatakis & Haberl 1993). Another application of the code would be to rapidly rotating stars with rotationally distorted surfaces. These stars have enhanced stellar wind outflow from their equatorial regions. The wind interaction with possible companion could also be matter of interest.

Bibliography

- Aab, O. E. 1983, *Pisma v Astronomicheskii Zhurnal*, 9, 606
- Aarseth, S. J. 1963, *MNRAS*, 126, 223
- Abbott, D. C. 1982, *ApJ*, 259, 282
- Abubekеров, M. K., Antokhina, E. A., & Cherepashchuk, A. M. 2004, *Astronomy Reports*, 48, 550
- Avni, Y. & Bahcall, J. N. 1975, *ApJ*, 197, 675
- Avni, Y. & Goldman, I. 1980, *A&A*, 90, 44
- Bahcall, J. N., Dyson, F. J., Katz, J. I., & Paczynski, B. 1974, *ApJ*, 189, L17
- Bahcall, J. N., Rosenbluth, M. N., & Kulsrud, R. M. 1973, *Nature Physical Science*, 243, 27
- Barthelmy, S. D., Barbier, L. M., Cummings, J. R., et al. 2005, *Space Sci. Rev.*, 120, 143
- Ben-Dor, G. 2007, *Shock Wave Reflection Phenomena* (Springer Science+Business Media)
- Bisiacchi, G. F., Dultzin, D., Firmani, C., & Hacyan, S. 1974, *ApJ*, 190, L59
- Blondin, J. M. 1994, *ApJ*, 435, 756
- Blondin, J. M., Kallman, T. R., Fryxell, B. A., & Taam, R. E. 1990, *ApJ*, 356, 591
- Bodenheimer, P., Laughlin, G., Rozyczka, M., & Yorke, H. 2006, *Numerical Methods in Astrophysics: An Introduction*, Series in Astronomy and Astrophysics (Taylor & Francis)
- Bolton, C. T. 1972a, *Nature Physical Science*, 240, 124
- . 1972b, *Nature*, 235, 271
- . 1975, *ApJ*, 200, 269
- Bondi, H. 1952, *MNRAS*, 112, 195

- Bondi, H. & Hoyle, F. 1944, MNRAS, 104, 273
- Bowyer, S., Byram, E. T., Chubb, T. A., & Friedman, H. 1965, Science, 147, 394
- Boyle, C. B. & Walker, I. W. 1986, MNRAS, 222, 559
- Bradt, H. V. D. & McClintock, J. E. 1983, ARA&A, 21, 13
- Braes, L. L. E. & Miley, G. K. 1971, Nature, 232, 246
- Brocksopp, C., Tarasov, A. E., Lyuty, V. M., & Roche, P. 1999, A&A, 343, 861
- Brucato, R. J. & Kristian, J. 1972, ApJ, 173, L105
- Brucato, R. J. & Zappala, R. R. 1974, ApJ, 189, L71
- Byram, E. T., Chubb, T. A., & Friedman, H. 1966, Science, 152, 66
- Caballero-Nieves, S. M., Gies, D. R., Bolton, C. T., et al. 2009, ApJ, 701, 1895
- Canalizo, G., Koenigsberger, G., Peña, D., & Ruiz, E. 1995, Rev. Mexicana Astron. Astrofis., 31, 63
- Cannon, A. J. 1936, Annals of Harvard College Observatory, 100, 1
- Cassinelli, J. P. 1979, ARA&A, 17, 275
- Castor, J. I., Abbott, D. C., & Klein, R. I. 1975, ApJ, 195, 157
- Castor, J. L. 1974, MNRAS, 169, 279
- Colella, P. & Woodward, P. R. 1984, Journal of Computational Physics, 54, 174
- Conti, P. S. 1978, A&A, 63, 225
- Cowley, A. P. 1992, ARA&A, 30, 287
- Cranmer, S. R. & Owocki, S. P. 1995, ApJ, 440, 308
- Davidson, K. & Ostriker, J. P. 1973, ApJ, 179, 585
- Davies, R. E. & Pringle, J. E. 1980, MNRAS, 191, 599
- Davis, R. & Hartmann, L. 1983, ApJ, 270, 671
- Dolan, J. F. 1992, ApJ, 384, 249
- Dolan, J. F. & Tapia, S. 1989, ApJ, 344, 830
- Edgar, R. 2004, New A Rev., 48, 843
- Eggleton, P. P. 1983, ApJ, 268, 368
- Ehrenfreund, P. & Charnley, S. B. 2000, ARA&A, 38, 427

- Emery, A. F. 1968, *Journal of Computational Physics*, 2, 306
- Fabian, A. C., Pringle, J. E., & Whelan, J. A. J. 1974, *Nature*, 247, 351
- Fisher, P. C., Johnson, H. M., Jordan, W. C., Meyerott, A. J., & Acton, L. W. 1966, *ApJ*, 143, 203
- Foing, B. H. & Ehrenfreund, P. 1994, *Nature*, 369, 296
- Frank, J., King, A., & Raine, D. J. 2002, *Accretion Power in Astrophysics: Third Edition*
- Fransson, C. & Fabian, A. C. 1980, *A&A*, 87, 102
- Friend, D. B. & Abbott, D. C. 1986, *ApJ*, 311, 701
- Friend, D. B. & Castor, J. I. 1982, *ApJ*, 261, 293
- Galazutdinov, G., Moutou, C., Musaeov, F., & Krelowski, J. 2002, *A&A*, 384, 215
- Gallo, E., Fender, R., Kaiser, C., et al. 2005, *Nature*, 436, 819
- Giacconi, R., Gorenstein, P., Gursky, H., et al. 1967, *ApJ*, 148, L129
- Giacconi, R., Gursky, H., Paolini, F. R., & Rossi, B. B. 1962, *Physical Review Letters*, 9, 439
- Gies, D. R. & Bolton, C. T. 1982, *ApJ*, 260, 240
- . 1986a, *ApJ*, 304, 371
- . 1986b, *ApJ*, 304, 389
- Gies, D. R., Bolton, C. T., Blake, R. M., et al. 2008, *ApJ*, 678, 1237
- Gies, D. R., Bolton, C. T., Thomson, J. R., et al. 2003, *ApJ*, 583, 424
- Gingold, R. A. & Monaghan, J. J. 1977, *MNRAS*, 181, 375
- Gontcharov, G. A. 2006, *Astronomy Letters*, 32, 759
- Gottlieb, E. W., Wright, E. L., & Liller, W. 1975, *ApJ*, 195, L33
- Gould, R. J. & Burbidge, G. R. 1963, *ApJ*, 138, 969
- Grinberg, V., Hell, N., Pottschmidt, K., et al. 2013, *A&A*, 554, A88
- Guinan, E. F., Dorren, J. D., Siah, M. J., & Koch, R. H. 1979, *ApJ*, 229, 296
- Gursky, H. 1966, *S&T*, 32, 252
- Hadrava, P. 1987, *Publications of the Astronomical Institute of the Czechoslovak Academy of Sciences*, 70, 263

- . 1995, *A&AS*, 114, 393
- . 1997, *A&AS*, 122, 581
- . 2004, *Publications of the Astronomical Institute of the Czechoslovak Academy of Sciences*, 92, 15
- Hadrava, P. 2007, in *Proceedings of RAGtime 8/9: Workshops on Black Holes and Neutron Stars*, ed. S. Hledík & Z. Stuchlík, 71–78
- . 2009a, ArXiv e-prints
- . 2009b, *A&A*, 494, 399
- Hadrava, P. & Čechura, J. 2012, *A&A*, 542, A42
- Hadrava, P. & Čechura, J. 2013, in *IAU Symposium, Vol. 290, IAU Symposium*, ed. C. M. Zhang, T. Belloni, M. Méndez, & S. N. Zhang, 219–220
- Hatchett, S., Buff, J., & McCray, R. 1976, *ApJ*, 206, 847
- Hatchett, S. & McCray, R. 1977, *ApJ*, 211, 552
- Herbig, G. H. 1995, *ARA&A*, 33, 19
- Hjellming, R. M. & Wade, C. M. 1971, *ApJ*, 168, L21
- Homan, J., Wijnands, R., van der Klis, M., et al. 2001, *ApJS*, 132, 377
- Horne, K. 1985, *MNRAS*, 213, 129
- Horne, K. & Marsh, T. R. 1986, *MNRAS*, 218, 761
- Hoyle, F. & Lyttleton, R. A. 1939, *Proceedings of the Cambridge Philosophical Society*, 35, 405
- . 1940, *Proceedings of the Cambridge Philosophical Society*, 36, 424
- Hutchings, J. B. 1978, *ApJ*, 226, 264
- Hutchings, J. B., Cowley, A. P., Crampton, D., et al. 1974, *ApJ*, 191, 743
- Hutchings, J. B., Crampton, D., Glaspey, J., & Walker, G. A. H. 1973, *ApJ*, 182, 549
- Ibragimov, A., Zdziarski, A. A., & Poutanen, J. 2007, *MNRAS*, 381, 723
- Kallman, T. R. & McCray, R. 1982, *ApJS*, 50, 263
- Karitskaya, E. A., Agafonov, M. I., Bochkarev, N. G., et al. 2005, *Astronomical and Astrophysical Transactions*, 24, 383
- Kato, S., Fukue, J., & Mineshige, S., eds. 1998, *Black-hole accretion disks*

- Krelowski, J. 2003, in *Solid State Astrochemistry*, ed. V. Pirronello, J. Krelowski, & G. Manicò, 147–174
- Krumholz, M. R., McKee, C. F., & Klein, R. I. 2004, *ApJ*, 611, 399
- Kumar, P., Ao, C. O., & Quataert, E. J. 1995, *ApJ*, 449, 294
- Lamb, F. K., Pethick, C. J., & Pines, D. 1973, *ApJ*, 184, 271
- Lamers, H. J. G. L. M. & Cassinelli, J. P. 1999, *Introduction to Stellar Winds*
- Laney, C. B. 1998, *Computational gasdynamics* (Cambridge, New York, NY: Cambridge University Press)
- LaSala, J., Charles, P. A., Smith, R. A. D., Balucinska-Church, M., & Church, M. J. 1998, *MNRAS*, 301, 285
- Lemaster, M. N. & Stone, J. M. 2009, *ApJ*, 691, 1092
- Li, H. & Ben-Dor, G. 1995, *Shock Waves*, 5, 259
- Lightman, A. P. & Shapiro, S. L. 1976, *ApJ*, 203, 701
- Lubow, S. H. & Shu, F. H. 1975, *ApJ*, 198, 383
- Lucy, L. B. 1977, *AJ*, 82, 1013
- Lyutyi, V. M., Syunyaev, R. A., & Cherepashchuk, A. M. 1973, *AZh*, 50, 3
- Manousakis, A., Walter, R., & Blondin, J. M. 2012, *A&A*, 547, A20
- Marsh, T. R. 2001, in *Lecture Notes in Physics*, Berlin Springer Verlag, Vol. 573, *Astrotomography, Indirect Imaging Methods in Observational Astronomy*, ed. H. M. J. Boffin, D. Steeghs, & J. Cuypers, 1
- Marsh, T. R. & Horne, K. 1988, *MNRAS*, 235, 269
- Matsuoka, M., Kawasaki, K., Ueno, S., et al. 2009, *PASJ*, 61, 999
- Mavromatakis, F. & Haberl, F. 1993, *A&A*, 274, 304
- McClintock, J. E. & Remillard, R. A. 2006, *Black hole binaries*, ed. W. H. G. Lewin & M. van der Klis, 157–213
- Meszaros, P., Nagel, W., & Ventura, J. 1980, *ApJ*, 238, 1066
- Mitsuda, K., Inoue, H., Koyama, K., et al. 1984, *PASJ*, 36, 741
- Miyamoto, S., Iga, S., Kitamoto, S., & Kamado, Y. 1993, *ApJ*, 403, L39
- Miyamoto, S. & Kitamoto, S. 1991, *ApJ*, 374, 741
- Morgan, E. H., Remillard, R. A., & Greiner, J. 1997, *ApJ*, 482, 993

- Motylewski, T., Linnartz, H., Vaizert, O., et al. 2000, *ApJ*, 531, 312
- Murdin, P. & Webster, B. L. 1971, *Nature*, 233, 110
- Nagel, W. 1981a, *ApJ*, 251, 288
- . 1981b, *ApJ*, 251, 278
- Ninkov, Z., Walker, G. A. H., & Yang, S. 1987, *ApJ*, 321, 425
- Oda, M. 1977, *Space Sci. Rev.*, 20, 757
- Orosz, J. A., McClintock, J. E., Aufdenberg, J. P., et al. 2011, *ApJ*, 742, 84
- Overbeck, J. W. & Tananbaum, H. D. 1968, *Physical Review Letters*, 20, 24
- Overbeck, J. W., Womack, E. A., & Tananbaum, H. D. 1967, *ApJ*, 150, 47
- Owocki, S. P., Castor, J. I., & Rybicki, G. B. 1988, *ApJ*, 335, 914
- Parker, E. N. 1958, *ApJ*, 128, 664
- . 1960, *ApJ*, 132, 821
- Pauldrach, A., Puls, J., & Kudritzki, R. P. 1986, *A&A*, 164, 86
- Pelupessy, I., Lamers, H. J. G. L. M., & Vink, J. S. 2000, *A&A*, 359, 695
- Petterson, J. A. 1978, *ApJ*, 224, 625
- Pringle, J. E. & Rees, M. J. 1972, *A&A*, 21, 1
- Rappaport, S., Zaumen, W., & Doxsey, R. 1971, *ApJ*, 168, L17
- Reid, M. J., McClintock, J. E., Narayan, R., et al. 2011, *ApJ*, 742, 83
- Remillard, R. A. 2005a, *Astronomische Nachrichten*, 326, 804
- Remillard, R. A. 2005b, in *22nd Texas Symposium on Relativistic Astrophysics*, ed. P. Chen, E. Bloom, G. Madejski, & V. Patrosian, 79–88
- Remillard, R. A. & McClintock, J. E. 2006, *ARA&A*, 44, 49
- Roedig, C., Zanotti, O., & Alic, D. 2012, *MNRAS*, 426, 1613
- Ruffert, M. 1994, *A&AS*, 106, 505
- Salama, F., Bakes, E. L. O., Allamandola, L. J., & Tielens, A. G. G. M. 1996, *ApJ*, 458, 621
- Salama, F., Galazutdinov, G. A., Krelowski, J., Allamandola, L. J., & Musaev, F. A. 1999, *ApJ*, 526, 265
- Sandage, A., Osmer, P., Giacconi, R., et al. 1966, *ApJ*, 146, 316

- Savonije, J. 1983, in *Accretion-Driven Stellar X-ray Sources*, ed. W. H. G. Lewin & E. P. J. van den Heuvel, 343–366
- Schulz, S. A., King, J. E., & Glinski, R. J. 2000, *MNRAS*, 312, 769
- Shafter, A. W., Harms, R. J., Margon, B., & Katz, J. I. 1980, *ApJ*, 240, 612
- Shakura, N. I. & Sunyaev, R. A. 1973, *A&A*, 24, 337
- Shapiro, S. L., Lightman, A. P., & Eardley, D. M. 1976, *ApJ*, 204, 187
- Shapiro, S. L. & Teukolsky, S. A. 1983, *Black holes, white dwarfs, and neutron stars: The physics of compact objects*
- Skilling, J. & Bryan, R. K. 1984, *MNRAS*, 211, 111
- Smak, J. 1979, *Acta Astron.*, 29, 309
- . 1981, *Acta Astron.*, 31, 395
- Sobczak, G. J., McClintock, J. E., Remillard, R. A., et al. 2000, *ApJ*, 531, 537
- Sod, G. A. 1978, *Journal of Computational Physics*, 27, 1
- Sowers, J. W., Gies, D. R., Bagnuolo, W. G., et al. 1998, *ApJ*, 506, 424
- Steeghs, D. 2003, *MNRAS*, 344, 448
- Stevens, I. R. 1988, *MNRAS*, 232, 199
- Stevens, I. R. & Kallman, T. R. 1990, *ApJ*, 365, 321
- Stone, J. M., Gardiner, T. A., Teuben, P., Hawley, J. F., & Simon, J. B. 2008, *ApJS*, 178, 137
- Stone, J. M., Hawley, J. F., Evans, C. R., & Norman, M. L. 1992, *ApJ*, 388, 415
- Taam, R. E. & Fryxell, B. A. 1988, *ApJ*, 327, L73
- Tananbaum, H., Gursky, H., Kellogg, E., Giacconi, R., & Jones, C. 1972, *ApJ*, 177, L5
- Tananbaum, H., Kellogg, E., Gursky, H., et al. 1971, *ApJ*, 165, L37
- Tarasov, A. E., Brocksopp, C., & Lyuty, V. M. 2003, *A&A*, 402, 237
- Tarter, C. B., Tucker, W. H., & Salpeter, E. E. 1969, *ApJ*, 156, 943
- Toro, E. F. 1997, *Riemann solvers and numerical methods for fluid dynamics : a practical introduction* (Berlin, New York: Springer)
- Tóth, G. & Odstrčil, D. 1996, *Journal of Computational Physics*, 128, 82

- Treves, A., Chiappetti, L., Tanzi, E. G., et al. 1980, *ApJ*, 242, 1114
- Truelove, J. K., Klein, R. I., McKee, C. F., et al. 1997, *ApJ*, 489, L179
- Čechura, J. 2012, in *X-ray Binaries. Celebrating 50 Years Since the Discovery of Sco X-1*
- Čechura, J. & Hadrava, P. 2014, *A&A*, *submitted*
- van Paradijs, J. & Verbunt, F. 1984, in *American Institute of Physics Conference Series*, Vol. 115, *American Institute of Physics Conference Series*, ed. S. E. Woosley, 49–62
- Voloshina, I. B., Lyutyi, V. M., & Tarasov, A. E. 1997, *Astronomy Letters*, 23, 293
- von Zeipel, H. 1924, *MNRAS*, 84, 665
- Vrtilek, S. D., Boroson, B. S., Hunacek, A., Gies, D., & Bolton, C. T. 2008, *ApJ*, 678, 1248
- Vrtilek, S. D., Peris, C., & Čechura, J. 2013, *Imaging Black Hole and Neutron Star Binaries*, nOAO Proposal
- Wade, C. M. & Hjellming, R. M. 1972, *Nature*, 235, 271
- Walborn, N. R. 1973, *ApJ*, 179, L123
- Walker, E. N. 1972, *MNRAS*, 160, 9P
- Wang, Y.-M. & Welter, G. L. 1981, *A&A*, 102, 97
- Webster, B. L. & Murdin, P. 1972, *Nature*, 235, 37
- Wen, L., Cui, W., Levine, A. M., & Bradt, H. V. 1999, *ApJ*, 525, 968
- White, N. E., Kaluzienski, J. L., & Swank, J. H. 1984, in *American Institute of Physics Conference Series*, Vol. 115, *American Institute of Physics Conference Series*, ed. S. E. Woosley, 31–48
- Wilms, J., Nowak, M. A., Pottschmidt, K., Pooley, G. G., & Fritz, S. 2006, *A&A*, 447, 245
- Wood, J., Horne, K., Berriman, G., et al. 1986, *MNRAS*, 219, 629
- Woodward, P. & Colella, P. 1984, *Journal of Computational Physics*, 54, 115
- Yan, J., Liu, Q., & Hadrava, P. 2008, *AJ*, 136, 631
- Zdziarski, A. A., Skinner, G. K., Pooley, G. G., & Lubiński, P. 2011, *MNRAS*, 416, 1324
- Zhang, S. N., Cui, W., Harmon, B. A., et al. 1997, *ApJ*, 477, L95
- Ziółkowski, J. 2014, *MNRAS*, 440, L61

List of author's publications

Publications in refereed journals

Čechura, J. & Hadrava, P. 2014, *Stellar wind in state transitions of high-mass X-ray binaries*, A&A submitted

Hadrava, P. & Čechura, J. 2012, *Really focused stellar winds in X-ray binaries*, A&A, 542, A42

Other publications

Shore, S. N., Čechura, J., Korčáková, D., et al. 2013, *Continuing spectroscopic observations (3600–8800 Å) of V339 Del = Nova Del 2013 in the early nebular stage with the Nordic Optical Telescope*, The Astronomer's Telegram, 5546, 1

Vrtilek, S. D., Peris, C. S. & Čechura, J. 2013, *Imaging Black Hole and Neutron Star Binaries*, NOAO Proposal ID 2013A-0184

Hadrava, P. & Čechura, J. 2013, *Accretion of stellar winds in high-mass X-ray binaries*, in IAU Symposium, Vol. 290, IAU Symposium, ed. C. M. Zhang, T. Belloni, M. Méndez, & S. N. Zhang, 219-220

Čechura, J. 2012, *Probing the Environment of X-ray Binaries*, in Proceedings of Conference "X-ray Binaries. Celebrating 50 Years Since the Discovery of Sco X-1", online at <http://cxc.harvard.edu/cdo/xrb12>, id.11

Čechura, J. 2011, *Hydrodynamics in X-ray binaries*, in WDS'11 Proceedings of Contributed Papers: Part III - Physics (eds. J. Šafránková and J. Pavlů), Prague, Matfyzpress, pp. 43–48